8-11-2017

Multicomponent Ligand Interactions with Colloidal Gold and Silver Nanoparticles in Water

Wumudu Dilhani Siriwardana

Multicomponent ligand interactions with colloidal gold and silver nanoparticles in water

By

W-K-Kumudu Dilhani Siriwardana

A Dissertation
Submitted to the Faculty of
Mississippi State University
in Partial Fulfillment of the Requirements
for the Degree of Doctor of Philosophy
in Chemistry
in the Department of Chemistry

Mississippi State, Mississippi

August 2017

Multicomponent ligand interactions with colloidal gold and silver nanoparticles in water

By

W-K-Kumudu Dilhani Siriwardana

Approved:

_____

Dongmao Zhang
(Major Professor)

_____

David O. Wipf
(Committee Member)

_____

Todd E. Mlsna
(Committee Member)

_____

Stephen C. Foster
(Committee Member)

_____

Joseph P. Emerson
(Graduate Coordinator / Committee Member)

_____

Rick Travis
Interim Dean
College of Arts & Sciences

Name: W-K-Kumudu Dilhani Siriwardana

Date of Degree: August 11, 2017

Institution: Mississippi State University

Major Field: Chemistry

Major Professor: Dongmao Zhang

Title of Study: Multicomponent ligand interactions with colloidal gold and silver nanoparticles in water

Pages in Study 126

Candidate for Degree of Doctor of Philosophy

Multicomponent ligand interactions are involved in essentially all nanoparticle (NP) applications. However, the ligand conformation and ligand binding mechanisms on NPs are highly controversial. The research reported here is focused on deepening the fundamental understanding of multicomponent ligand interactions with gold and silver nanoparticles (AuNPs and AgNPs) in water.

We demonstrated that AuNPs passivated by saturated layer of poly(ethylene glycol) (PEG-SH) have large fractions of AuNP surface area available for ligand adsorption and exchange. The fraction of AuNP surface area passivated by PEG-SH with molecular weights of 2000, 5000, and 30000 g/mol was calculated to be ~ 25%, ~20%, and ~9% using 2-mercaptobenzimidazole and adenine as model ligands.

The effect of both reduced and oxidized protein cysteine residues on protein interactions with AgNPs was investigated. The model proteins included wild-type and mutated GB3 variants with 0, 1, or 2 reduced cysteine residues. Bovine serum albumin containing 34 oxidized (disulfide-linked) and 1 reduced cysteine residues was also included. Protein cysteine content that were found to have no detectable effect on kinetics

of protein/AgNP binding. However, only proteins that contain reduced cysteine induced significant AgNP dissolution.

We further demonstrated that organothiols can induce both AgNP disintegration and formation under ambient conditions by simply mixing organothiols with AgNPs or $AgNO_3$, respectively. Surface plasmon- and fluorescence-active AgNPs formed by changing the concentration ratio between Ag^+ and organothiol. Organothiols also induced AuNP formation by mixing $HAuCl_4$ with organothiols, but no AuNP disintegration occured.

Finally, we proposed that multicomponent ligand binding to AuNPs can be highly dependent on the sequence of ligand mixing with AuNPs. Quantitative studies revealed that competitive adenine and glutathione adsorption onto both as-synthesized and PEG-SH functionalized AuNPs is predominantly a kinetically controlled process. Besides providing new insights on multicomponent ligand interactions with colloidal AuNPs and AgNPs, this study opens a new avenue for fabrication of novel nanomaterials in biological/biomedical applications.

DEDICATION

I would like to dedicate this doctoral dissertation to my parents Priyankara Widuramal Siriwardana and Srimathie Kariyawasam, and my brother, Chamath Ushantha Siriwardana, for their love and enormous support.

ACKNOWLEDGEMENTS

I take this opportunity to express my deepest gratitude to many wonderful people without whose assistance and guidance this journey would have never been successful. In particular, I would like to acknowledge several people.

First and foremost, I would like to express my sincere gratitude to my advisor Dr. Dongmao Zhang, for the continuous support and guidance throughout my Ph.D. study and related research, for his patience, motivation, and immense knowledge. His guidance helped me all the time of research and I consider it truly a privilege to have worked in such an encouraging and academically engaging environment.

I am grateful to all my committee members Dr. Stephen C. Foster, Dr. David O. Wipf, Dr. Todd E. Mlsna, and Dr. Joseph P. Emerson for their helpful suggestions and discussions. I sincerely thank former and current graduate coordinators, Dr. Stephen C. Foster and Dr. Joseph P. Emerson, for their guidance throughout my graduate career.

I want to thank all our collaborators: Dr. Nicholas Fitzkee (Mississippi State University), Dr. Shengli Zou (University of Central Florida), Dr. Felio Perez (University of Memphis), Dr. Willard E. Collier (Tuskegee University). I thank them all for their insightful input.

I have been blessed with a helpful and friendly research group. I would like to thank all my fellow labmates in Dr.Zhang's lab for their stimulating discussion and support during my research.

Last but not least, I would like to thank my family: my parents and my brother for supporting me spiritually throughout my graduate career and life.

TABLE OF CONTENTS

LIST OF TABLES

LIST OF FIGURES

LIST OF ABBREVIATIONS

NPs	Nanoparticles
AuNPs	Gold nanoparticles
AgNPs	Silver nanoparticles
PEG	Poly(ethylene glycol)
SAMs	Self-assembled monolayers
PEG-SH	Thiolated poly(ethylene glycol)
SPR	Surface plasmon resonance
UV-vis	Ultraviolet visible
FRET	Fluorescence resonance energy transfer
FTIR	Fourier transform infrared
XPS	X-ray photoelectron spectroscopy
TEM	Transmission electron microscopy
SEM	Scanning electron microscopy
LSPR	Localized surface plasmon resonance
2-MBI	2-Mercaptobenzimidazole
pAuNP	Pegylated AuNPs
BSA	Bovine serum albumin
ME	2-Mercaptoethanol
DLS	Dynamic light scattering

GB3	IgG-binding domain of protein G
Cys	Cysteine
Hcy	Homocysteine
Prt	Propanethiol
Cyt	Cystine
SERS	Surface enhanced Raman spectroscopy
GSH	Glutathione
AgNC	Silver nanoclusters
HED	2-Hydroxyethyl disulfide
MBT	methylbenzenethiol

CHAPTER I

INTRODUCTION

Metallic nanoparticles (NPs) possess unique optical, electronic, chemical, and magnetic properties, which can completely different from their bulk and atomic counterparts. This unique behavior of NPs is mainly due to the NP's high surface-to-volume ratio,[1,2] and the quantum size effect[3] of materials in the nanometer size regime. The fabrication of nanomaterials and exploration of their unique properties has attracted tremendous interest in almost all branches of scientific research, including physics, chemistry, biology, and engineering. NPs have been widely applied in biosensing, catalysis, targeted drug delivery, solar energy harvesting, photo thermal therapy, and cellular imaging.[4-10] In many of these applications, NP stability, biocompatibility, and target specificity have been enhanced by surface functionalization using a variety of ligands. The main objective of this chapter is to discuss the properties of colloidal spherical gold and silver nanoparticles in water and the importance of understanding the NP interfacial interactions for essentially all NP applications.

Gold nanoparticles (AuNPs) and silver nanoparticles (AgNPs) are the most extensively studied metallic NPs. The most widely used spherical AuNP synthesis method is the citrate reduction method.[11] Turkevich et al. developed this method in 1951 by reducing gold(III) chloride ($AuCl_4^-$) to Au(0) using sodium citrate.[11] Sodium citrate acts as both a reducing and capping agent. In 1973, Frens et al. synthesized AuNPs with

different sizes (12-150 nm) by changing the ratio of $AuCl_4^-$ to citrate.[12] Citrate capping agents impart a negative charge on the AuNP surface resulting in electrostatic repulsion between individual AuNPs, which enhances the dispersion stability of AuNPs in water. The Brust-Schiffrin phase transfer method is another AuNP synthesis method.[13] $AuCl_4^-$ is transferred from aqueous solution to toluene using teraoctylammonium bromide as the phase-transfer reagent and then reduced with sodium borohydride in the presence of dodecanethiol.[13] This method leads to direct synthesis of surface functionalized NPs with thiols. While the Turkevich method allows the synthesis of AuNPs with a broad size range, the Brust-Schiffrin method can be used to synthesize small NPs (1-3 nm).

The antimicrobial properties of AgNPs have led to widespread use of AgNPs in industrial and medicinal applications. Lee and Misel developed the most common citrate reduction method to synthesize AgNPs in 1982.[14] In this method, $AgNO_3$ was used as the Ag precursor and sodium citrate was used as the reducing and capping agent. Sodium borohydrate has also been used as the reducing agent in AgNP synthesis. Another less common method of AgNP synthesis is γ-irradiation of a silver salt ($AgClO_4$) in the presence of a citrate stabilizer and an alcohol radical scavenger.[15]

NP surface functionalization is essential in almost all NP applications. For example, if NPs without surface functionalization are administered into the body for biomedical applications, proteins, enzymes, and electrolytes present in the biofluid/biological matrix will react with the incoming NPs, resulting in NP aggregation.[16] This will prevent NPs from reaching the targeted organ inside the body. Therefore, surface functionalization is generally necessary for NP stability, target specificity, and biocompatibility in biomedical applications.

1.1 Surface functionalization of AuNPs and AgNPs

Surface functionalization or ligand adsorption can tune NP surface properties to enhance NP stability, target specificity, and biocompatibility.[17,18] The stability of NPs in a complex biological mixture is critically depend on the structure, binding affinity, and packing density of the ligand bound to the NP surface.

Three common strategies are available for NP surface functionalization.[19] Firstly, nanoparticles can be synthesized in the presence of the ligands used for surface functionalization. For example, alkanethiols are added to the reaction mixture during NP synthesis using the Brust-Schiffrin method.[13] The second method is the ligand exchange method.[20-22] Displacement of the initially bound ligands by a desired incoming ligand with stronger affinity to NPs will allow NP surface functionalization with the second ligand. The third approach is surface modification using covalent bond formation.[23] After a chemical reaction, the terminal functional group of the surface bound ligand can be attached to another ligand with important properties. This allows incorporation of many different functionalities to the NP surface.

Good surface ligands typically contain functional groups which are able to bind strongly to the NP surface, charged and/or polymer segments that provide electrostatic or steric stabilization, and self-interacting segments that discourage ligand dissociation.[24] Surface ligands stabilize NPs against aggregation in a variety of ways.[24] Surface ligands act as a barrier to undesirable incoming ligands preventing physical and chemical access to the NP surface. Moreover, surface ligands help to increase the compatibility of NPs with a solvent, inhibit NP-NP interactions sterically and/or electrostatically, slow down

the loss of surface atoms to the solution, and provide functional groups for conjugating biological or other molecules to the particle without interfering with the NP surface.[25,26]

A protecting ligands should contain a functional group that has strong affinity to the metal to ensure strong ligand adhesion to the NP surface. Several functional groups including polymers, macromolecules, and biomolecules have been reported in literature to protect NP surface against NP aggregation.[27] Specifically, citrate, amines, nucleic acids, peptides, antibodies, and lipids are a few molecules that have been used as functionalizing ligands.[26] Additionally, polymers including polysaccharides, polyacrylamide, poly(vinyl alcohol), poly(*N*-vinyl-2-pyrrolidone), poly(ethylene glycol) (PEG), and PEG containing copolymers have also been used in NP surface functionalization.[27-29]

AuNPs have high stablity in aqueous media. AuNPs form strong bonds with soft ligands,[30] so, thiols and phosphines are often used as AuNP stabilizing agents.[19,31,32] However, aqueous AgNPs are not stable and they dissolve into silver ions if they are not sufficiently stabilized.[33] Therefore, it is important to understand the destabilizing mechanism and dissolution process of AgNPs. Currently the understanding of the AgNP dissolution and destabilization mechanisms are incomplete. It is necessary to fill the knowledge gap on the effect of AgNP surface coating against dissolution in order to understand the dissolution process.

1.1.1 Organothiol interactions with NPs

Organothiols are organic molecules with thiol functional groups. Thiol-Au chemistry has been widely used in many different fields including chemistry, physics, molecular biology, pharmaceutical engineering, and material science due to the formation

of a strong covalent Au-S bond.[19,34,35] Self-assembled monolayers (SAMs) of thiols on planar gold surfaces, gold nanoclusters, and AuNPs have been studied for decades.[19,35]

Organothiols have also been used to functionalize the AgNP surface.[36-39] However, organothiols can continuously react with AgNPs, converting the silver oxide on the AgNP surface and silver atoms into a water-insoluble Ag^+-thiolate salt.[40] Organothiol structure and conformation determine the rate of such conversions. For instance, aromatic organothiols produce large Ag^+-thiolate precipitates that can accumulate on the AgNP surface or settle elsewhere,[40] while long chain alkanethiols are mostly adsorbed as monolayers.[37,41]

1.1.2 Protein interactions with NPs

Better understanding of protein and AuNP interfacial interactions opens the door for numerous AuNP applications including biodiagnosis, photothermal therapy, targeted drug delivery, and catalysis.[42] Protein adsorption onto the AuNP surface occurs via nonspecific intermolecular forces such as electrostatic, hydrophobic, and van der Waals interactions, as well as, specific Au-S covalent bond formation.[43-46] Proteins present in biofluids adsorb onto the nanoparticle surface forming a "protein corona" at the bio-nano interface.[42,47,48] The protein inner layer forms a hard corona with slower exchangeable proteins and outer layer referred as soft corona which consists of weakly bound proteins with faster exchange rate.[49] Plasma protein adsorption onto the nanoparticle surface depends on the NP size and surface charge or the hydrophobicity, size, and surface functionality of the proteins.[44,50]

According to literature reports, protein exchange on the AuNP surface can either occur through dissociative exchange or associative (displacement) exchange.[51] The

dissociative exchange pathway depends on the amount of protein adsorbed onto the AuNP surface and ligand desorption activation energy, while the rate of associative exchange depends on the concentration of the incoming ligand and its penetration capability. However, the exact protein exchange pathway is currently unclear. Therefore, it is worthwhile to fill the existing knowledge gap regarding the protein exchange mechanism on AuNP surfaces. Understanding whether protein adsorption and exchange onto the AuNP surface is kinetically or thermodynamically controlled is important since it opens the door for many biomedicinal and nano-science applications.

Apart from protein interactions with NPs, several studies have been reported about protein interactions with organothiol fuctionalized NPs.[43,52-54] In our previous study, we reported that protein conformation on the AuNP surface can be modified even after 3 days of AuNP incubation with protein.[53] Also, the number of thiol containing groups (cysteine) present in a protein has no significant effect on the initial protein adsorption onto AuNPs.[43] However, the amount of cysteine on protein functionalized AuNPs has a significant effect on organothiol induced AuNP aggregation.[43]

1.1.3 Thiolated poly(ethylene glycol) (PEG-SH) interactions with NPs

PEG-SH has been widely used as a biocompatible surface functionalizing ligand.[29,55,56] Due to the amphiphilic nature of PEG-SH, pegylated NPs are stable in both hydrophilic and lipophilic solvents.[4] Pegylation prevents protein adsorption onto AuNPs and stabilizes AuNPs against electrolyte induced aggregation.[29,56-59] The size, geometry, and attachment site of PEG-SH play critical roles in designing pharmaceutically important nanomaterials.[60] Both "mushroom" and "brush" confirmations of PEG-SH have been reported when it is grafted onto a lipid membrane.[55,60]

It has been reported that PEG-SH has been used as a linker to incorporate peptides, antibody, or labelling molecules onto the NP surface.[61,62] Larson-Smith et al. studied the competitive alkanethiol adsorption onto pegylated AuNPs by replacing PEG-SH.[63,64] It has been demonstrated that the conformation and surface concentration of PEG-SH on AuNP surfaces is affected by the length and packing density of the alkanethiol. They proposed a significant thiol replacement on pegylated AuNPs when small thiols were used.[56,63] There are also several other PEG-SH displacement studies.[21,65]

There is abundant literature on the benefits of pegylation and its ability to reduce protein adsorption and diminish non specific interactions with cells, and there are also many ligand displacement studies of PEG-SH on AuNPs.[27,29,63,66] However, the possibility of ligand adsorption and exchange without significant PEG-SH displacement has not been systematically evaluated.

This work will focus on the interactions of the aforementioned proteins, PEG-SH, and organothiols with AuNPs and AgNPs in water.

1.2 Analytical strategies for studying ligand interactions with NPs

Various analytical techniques are available to characterize the changes associated with AuNPs and AgNPs due to their interfacial interactions with ligands. The optimal technique is determined from the desired information needed and the type of the NP-ligand system is being studied.

AuNPs and AgNPs show characteristic surface plasmon resonance (SPR) peaks in their UV-vis spectra. NP size, aggregation state, and the local dielectric environment determine the SPR peak position and broadness.[67] The UV-vis spectroscopic method is

faster, cheaper, simpler, and requires less sample preparation compared to other methods.[42] The UV-vis spectroscopic method must be combined with other analytical methods to get a better understanding about ligand interfacial interactions.

Fluorescence spectroscopy also has been used to study NP-ligand interactions by taking advantage of the intrinsic fluorophores in ligands or by using fluorescence labelled ligands.[68,69] This is a more sensitive technique even though analysis is affected by the stability issues of fluorophores. However, the inner filter effect correction is necessary before experimental result interpretation. Steady-state and time-resolved fluorescence spectroscopy, fluorescence resonance energy transfer (FRET), and fluorescence correlation spectroscopy are some available measurement techniques.

Surface information about ligand functionalized NPs can be obtained using Fourier transform infrared (FTIR) and Raman spectroscopic techniques.[70-72] X-ray photoelectron spectroscopy (XPS) is another widely used surface analysis technique. Elemental identification and the chemical state of surface elements can be determined using XPS.[70]

Transmission electron microscopy (TEM) and scanning electron microscopy (SEM) are two other commonly used surface imaging techniques.[73,74] Dynamic light scattering (DLS) and zeta-potential measurements can be used to determine hydrodynamic diameter and surface charge, respectively.[75]

The following section includes background on the localized surface plasmon resonance (LSPR) principal which has been largely employed in this study.

1.3 Localized surface plasmon resonance (LSPR)

Metallic NPs have unique and extraordinary optical properties that have been extensively studied for decades. Noble metal NPs exhibit a strong absorption band in the visible region which is absent in individual atoms and bulk gold.[76,77] Localized surface plasmon resonance (LSPR) is an optical phenomena generated by a light wave trapped within conductive NPs smaller than the incident wavelength of light.[76-80] This is a result of the interactions between the incident light and surface electrons in a conduction band. Incident photon frequency is resonant with the collective oscillation of conduction band electrons resulting in an extinction band. Figure 1.1 shows the schematic representation of the plasmon oscillation for a spherical particle. Upon light irradiation of a small spherical metallic NP, the oscillating electric field causes the conduction electrons to oscillate coherently. When the electron cloud is displaced relative to the nuclei, a restoring force arises from Coulombic interaction between electrons and nuclei which results in oscillation of the electron cloud relative to the nuclear frame work.[76]

LSPR is strongly depends on the composition, size, geometry, dielectric environment, and particle-particle separation distance of NPs.[77] As a result of extremely intense and localized electromagnetic field generated by LSPR, NPs are highly sensitive to small changes in the local refractive index.[80] Extinction spectral peak shift can be observed due to these changes. For example, binding of a molecule with high refractive index (relative to the solvent or air) to the NP surface results in a red shift of the extinction peak maxima.

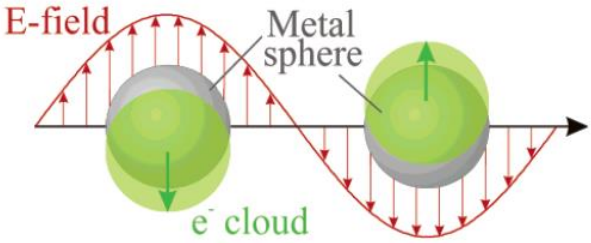

Figure 1.1 Schematic representation of plasmon oscillation for a sphere. Reproduced with permission from ref.[76] Copyright 2003 Americal Chemical Society.

In the limit of $2R << \lambda$ (where R is the radius of the NP and λ is the wavelength of the light in the media), only the electric dipole term contributes significantly to the extinction cross section (C_{ext}).[80] In that case Mie's solution of Maxwell's equation can be used to obtain the spectrum for well separated NPs.[77,81]

$$C_{ext} = \frac{24\pi^2 R^3 \varepsilon_m^{3/2} N}{\lambda \ln(10)} \frac{\varepsilon_i}{(\varepsilon_r + \chi\varepsilon_m)^2 + \varepsilon_i^2} \quad (1.1)$$

Where;

ε_m - dielectric constant of the surrounding medium

$\varepsilon = \varepsilon_r + i\varepsilon_i$ - complex dielectric constant of the bulk metal

R - radius of the NP

N - electron density

χ - 2 for spherical particle

1.4 Dissertation objective

Multicomponent ligand interfacial interactions with colloidal AuNPs and AgNPs are critical and complicated phenomena. Our research group is interested in studying protein, electrolyte, and organothiol interactions with metal NPs and their applications.

As a part of an extension to the current fundamental understanding of NP interfacial interactions, the main goal of this dissertation is to discuss multicomponent ligand interactions with AuNPs and AgNPs in water using proteins, PEG-SH, and organothiols as probe molecules.

This dissertation is composed of five chapters. An overview of the dissertation including current state-of-knowledge to the subject related to the dissertation is included in Chapter 1. Chapter 2 describes the ligand adsorption and exchange processes on pegylated AuNPs in water using adenine and 2-mercaptobenzimidazole (2-MBI) as model ligands. The surface area passivated by PEG-SH with different chain lengths will be discussed. Chapter 3 compares the effect of number of cysteine residues in proteins for AgNP dissolution. Also, the effect of reduced and oxidized protein cysteine residues on protein interactions with AgNPs will be discussed. Chapter 4 compares and contrasts AgNP disintegration and formation under ambient conditions using organothiols. The organothiol's ability to function as a stabilizing, chelating, and reducing agent will also be discussed. The key focus in Chapter 5 is to study the effect of proteine and organothiol mixing sequence on the stability of AuNPs in water. In addition to providing new insight on multicomponent ligand interactions with AuNPs and AgNPs, the work reported in this dissertation is important for nanomaterial fabrication and application.

CHAPTER II

LIGAND ADSORPTION AND EXCHANGE ON PEGYLATED GOLD NANOPARTICLES

(Published in *J. Phys. Chem. C* **2014,** *118*, 11111-11119)

2.1 Abstract

Previous researchers proposed that thiolated polyethylene glycol (PEG-SH) adopts a "mushroom-like" conformation on gold nanoparticles (AuNPs) in water. However, information regarding the size and permeability of the PEG-SH mushroom caps and surface area passivated by the PEG-SH mushroom stems are unavailable. Reported herein is our finding that AuNPs that are saturated by PEG-SHs all have large fractions of AuNP surface area available for ligand adsorption and exchange. The model ligands adenine and 2-mercaptobenzimidazole (2-MBI) can rapidly penetrate the PEG-SH overlayer and adsorb onto the AuNP surface. Most of the ligand adsorption and exchange occurs within the first few minutes of the ligand addition. The fraction of AuNP surface area passivated by saturation packed model PEG-SHs are ~25%, ~20%, and ~9% for PEG-SHs with molecular weights of 2000, 5000, and 30000 g/mol, respectively. Localized surface plasmonic resonance and dynamic light scattering show that the PEG-SH overlayer is drastically more loosely packed than the protein bovine serum albumin on AuNPs. Studies investigating the effect of aging the AuNP/PEG-SH

mixtures on subsequent adenine adsorption onto the pegylated AuNPs revealed that PEG-SHs reach approximately a steady-state binding on AuNPs within 3 h of sample incubation. This work sheds new insights into the kinetics, structures, and conformations of PEG-SHs on AuNPs and demonstrates that pegylated AuNPs can be used as an important platform for studying ligand interaction with AuNPs. In addition, it also opens a new avenue for fabrication of multicomponent functionalized nanoparticles.

2.2 Introduction

Gold nanoparticle (AuNP) pegylation, self-assembly of a layer of thiolated poly(ethylene glycol) (PEG-SH) onto AuNPs, has been used extensively in a wide range of AuNP applications.[4,27,56,82] Pegylation can stabilize AuNPs against electrolyte-induced aggregation.[29,58,59] It can also inhibit protein adsorption onto AuNPs.[16,56,57,63,83] While there have been numerous reports on ligand displacement studies of PEG-SHs on AuNPs,[21,63] the possibility of ligand adsorption (without significant PEG-SH displacement) onto pegylated AuNPs, to our knowledge, has not been systematically evaluated. Such a study is critical for understanding the structures and morphologies of PEG-SHs on AuNPs. For example, it has been proposed that PEG-SHs adopt a mushroom-like structure on AuNPs.[29,60] However, definitive confirmation of this structure is challenging because it is currently impossible to directly visualize the PEG-SH structure on AuNPs in water. A direct consequence of a mushroom-like PEG-SH architecture on AuNPs is that there should be a large fraction of the AuNP surface that is covered by the PEG-SH mushroom cap, but not passivated by the PEG-SH mushroom stem. Therefore, exploration of the fraction of the AuNP surface actually passivated by

PEG-SH has critical significance for understanding its conformation and properties of PEG-SHs on AuNPs.

Reported herein is our finding that the PEG-SH overlayer on AuNPs is exceedingly permeable for ligand adsorptions, and that PEG-SH only passivates a small fraction of the AuNP surface. Consequently, pegylated AuNPs can serve as an important platform for studying ligand adsorption and exchange on AuNPs. However, these studies can be challenging when using as-synthesized AuNPs because many ligands can induce AuNP aggregation and settlement. The model ligands used in this work are adenine and 2-mercaptobenzimidazole (2-MBI) (Figure 2.1) that were chosen for the following considerations. First, 2-MBI has recently been used as a probe to study protein binding with AuNPs.[53] Using 2-MBI in this work allows us to compare and contrast ligand binding to PEG-SH- and protein-coated AuNPs. This is important for developing an understanding of the similarities and differences in the structures and properties between polymer and biopolymer functionalized AuNPs. Second, 2-MBI and adenine have different binding affinities to AuNPs. Therefore, they constitute an ideal pair of probe molecules for studying ligand exchange on pegylated AuNPs. 2-MBI is a stable organosulfur compound that binds to AuNPs through the formation of a covalent S-Au bond,[84-86] while adenine can only bind nonspecifically to AuNPs, thus it has a drastically lower affinity than 2-MBI for AuNPs. This point was experimentally confirmed in this work by the observation that adenine is readily displaced by 2-MBI. Thirdly, 2-MBI and adenine are both UV-vis active. This enables UV-vis quantification of ligand adsorption and exchange on the pegylated AuNPs. It also allows us to study the effect of AuNP binding on the adenine UV-vis absorption. Previous research by us and others

demonstrated that AuNP binding quenches the UV-vis absorption of 2-MBI and other aromatic organothiols.[53,87,88] This effect was attributed to charge transfer between the covalently bonded organithiols and AuNPs.[89] However, charge transfer between AuNPs and adenine or other nonspecific ligands has, to our knowledge, not been experimentally demonstrated, even though charge transfer has been commonly invoked in surface enhanced Raman spectroscopy to explain possible chemical enhancement.[90,91]

Three PEG-SHs with nominal molecular weights of 2000, 5000, and 30000 g/mol were used in this work, and they are referred hereafter as PEG_{2K}-SH, PEG_{5K}-SH, and PEG_{30K}-SH, respectively. The AuNP and PEG-SH binding was monitored using the AuNP localized surface plasmonic resonance (LSPR). The kinetics of the adenine and 2-MBI adsorption onto the pegylated AuNPs (pAuNP) was studied as a function of the aging time of AuNP/PEG-SH mixtures before ligand addition. This aging study allowed us to estimate the kinetics of the AuNP pegylation process that is the time required for PEG-SHs to reach a steady-state adsorption and conformation on the AuNPs. Similar aging studies have been conducted in earlier research to probe the kinetics of bovine serum albumin (BSA) binding to AuNPs.[53] Our hypothesis is that once the PEG-SHs reach equilibrium adsorption and conformation on the AuNPs, further aging of the AuNP/PEG-SH mixtures will not have a significant effect on the kinetics and the amount of subsequent 2-MBI or adenine adsorbed onto the pAuNPs. In this work, we used the notation of (A/B)*t*/C to represent a three-component mixture in which the two components inside the parenthesis were mixed for a period of time *t* before the addition of the third component.

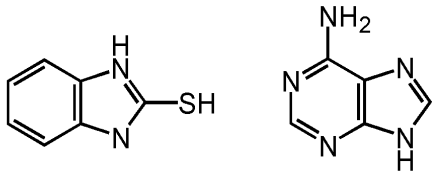

2-Mercaptobenzimidazole (2-MBI) Adenine

Figure 2.1 Molecular structure of model ligands used in this study.

2.3 Experimental section

2.3.1 Materials and instruments

All chemicals except PEG_{30K}-SH were purchased from Sigma-Aldrich. PEG_{30K}-SH was purchased from Laysan Bio, Inc. Thiolated poly(ethylene glycol) monomethyl ether with molecular weights of 30000 (PEG_{30K}-SH), 5000 (PEG_{5K}-SH), and 2000 (PEG_{2K}-SH) g/mol were dialyzed and used. The purities of both PEG_{5K}-SH and PEG_{2K}-SH were 98%. Nanopure water (18.2 MΩ cm) was used in sample preparation. An Evolution 300 spectrophotometer was used for steady-state UV-vis measurements and an Olis HP 8452 A diode array spectrophotometer was used for the time-resolved UV-vis measurements. Centrifugations were performed using a Marathon 21000R Fisher Scientific instrument. All solution mixtures were prepared and incubated under ambient conditions.

2.3.2 AuNP synthesis

AuNPs were synthesized by using the citrate reduction method reported in the literature.[92] Gold(III) trihydrate (0.0415 g) was dissolved in 100 mL of Nanopure water

(18.2 MΩ cm). The solution was refluxed while stirring. Sodium citrate (0.1141 g) was dissolved in 10 mL of Nanopure water (18.2 MΩ cm) and added to the boiling solution of gold(III) trihydrate. The mixture was refluxed for another ~ 20 min then cooled to room temperature while stirring in order to prevent aggregation. The concentration of synthesized AuNPs was determined using the UV-vis spectrophotometer.

2.3.3 Displacement of adsorbed adenine from as-synthesized AuNPs by 2-MBI

The two times concentrated as-synthesized AuNP solution (1.5 mL) was mixed with an equal volume of adenine (147.6 μM) solution. The resulting solution was briefly vortexed and allowed to sit at room temperature for ~ 12 h at which the adenine adsorbed AuNPs were completely aggregated and allowed to settle. Replicate samples were prepared for each analysis time. After sample incubation, 1.5 mL of the supernatant was removed and the free adenine in the supernatant was quantified using a UV-vis spectrophotometer. The amount of adenine adsorbed was calculated as the difference between the amount of adenine added and the amount of free adenine in the supernatant. To make the total number of moles of adenine and 2-MBI approximately the same in the ligand exchange solution, 1.93 mL of 2-MBI (64.9 μM) was added to the remaining 1.5 mL AuNP/adenine solution. The AuNP/adenine/2-MBI mixtures were vortexed briefly for ~ 5 s and allowed to incubate for predefined periods before quantification of the 2-MBI and adenine remaining free in the supernatant. During each analysis time, the UV-vis spectrum of the supernatant was taken and later deconvoluted to determine the amount of free adenine and 2-MBI in the supernatant. A control sample was prepared by adding 1.93 mL 2-MBI (64.9 μM) to 1.5 mL of the adenine supernatant (without AuNPs).

2.3.4 Adenine and 2-MBI adsorption onto pAuNPs

Colloidal AuNPs (1 mL) and different concentrations of PEG-SHs (1 mL) were mixed and incubated for 5 h. Subsequently, 1 mL of either 2-MBI or adenine solution was added into each of the AuNP/PEG-SH mixtures, and the three-component mixtures were incubated overnight before centrifugation quantification of the 2-MBI or adenine adsorbed. Centrifugation was conducted at 9000 rpm for 1h. The amount of 2-MBI or adenine that remained free in the supernatant was quantified with UV-vis spectroscopy.

2.3.5 Adenine/ 2-mercaptoethanol (ME) exchange on the pAuNPs

AuNP (1 mL) and PEG_{30K}-SH (1 mL) solutions were mixed and incubated for 5 h before the addition of 1 mL of adenine or ME. The resulting three-component mixtures were incubated overnight before the addition of incoming ME or adenine ligand. The amount of adenine displaced was quantified by centrifugation removal of pAuNPs together with their surface adsorbates. Centrifugation was conducted at 9000 rpm for 1h. The amount of adenine that remained free in the supernatant was quantified with UV-vis spectroscopy.

2.3.6 Dynamic light scattering (DLS)

Colloidal AuNPs (1 mL, 14.2 nM) were mixed with 1 mL of 30 μM PEG-SH or BSA solution. The AuNP/PEG-SH or AuNP/BSA mixtures were incubated overnight before collecting DLS measurements with a ZetaPALS analyzer. The hydrodynamic radii were calculated with five independent measurements.

2.4 Results and discussion

2.4.1 Pegylation of AuNPs

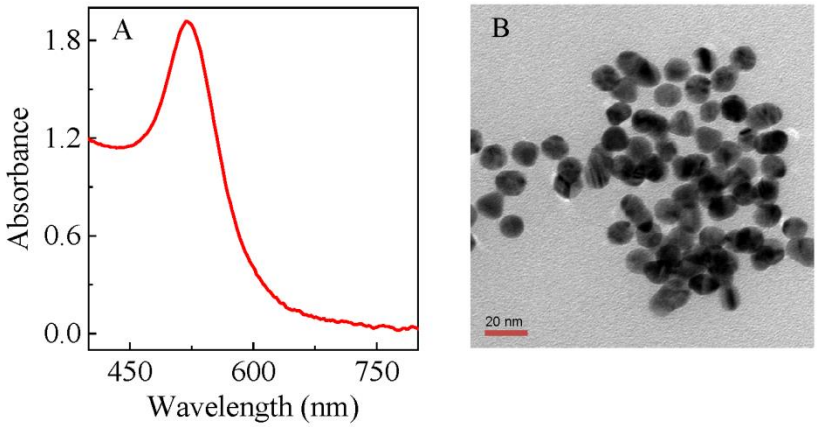

Figure 2.2 (A) UV-vis spectrum and (B) TEM image of as-synthesized AuNPs.

Note: UV-vis spectrum was obtained using a two times diluted as-synthesized AuNP solution. The particle size of the AuNPs is ~13 nm in diameter. The concentration of the as-synthesized AuNP is 7.1 nM, which is estimated on the basis of the AuNP UV-vis peak absorbance at 520 nm and the published AuNP UV-vis extinction coefficient.[93]

AuNPs used in this work were prepared by using a published procedure[92] and the particle size was ~13 nm in diameter. This was calculated on the basis of a AuNP TEM image (Figure 2.2) and the dynamic light scattering results (Table 2.1). AuNP pegylation was monitored using time-resolved UV-vis that measures the AuNP LSPR absorption as a function of time after the PEG-SH addition into the colloidal AuNPs (Figure 2.3). The PEG-SH binding was also compared to BSA binding to AuNPs (Figure 2.3).[53] An immediate red-shift in the AuNP LSPR peak wavelength and an instantaneous increment in the AuNP LSPR peak absorbance were observed upon PEG_{2K}-SH, PEG_{5K}-SH, and PEG_{30K}-SH addition to AuNPs (Figure 2.3), indicating that PEG-SH binding to AuNPs is an exceedingly rapid process. The net increases in the AuNP LSPR absorbance induced

by PEG_{2K}-SH, PEG_{5K}-SH, and PEG_{30K}-SH are 0.18, 0.08 and 0.06 (Table 2.1), respectively. The degree of AuNP LSPR red-shift also decreases with increasing PEG-SH chain lengths (Figure 2.3 and Table 2.1). It is noted that in these samples the amount of each PEG-SH added to the AuNPs was higher than the AuNP saturation packing capacities predicted for all model PEG-SHs by the saturation packing densities provided in earlier works.[21,60] This result indicates that the AuNP LSPR change induced by fully packed PEG-SHs decreases with increasing PEG-SH molecular weight.

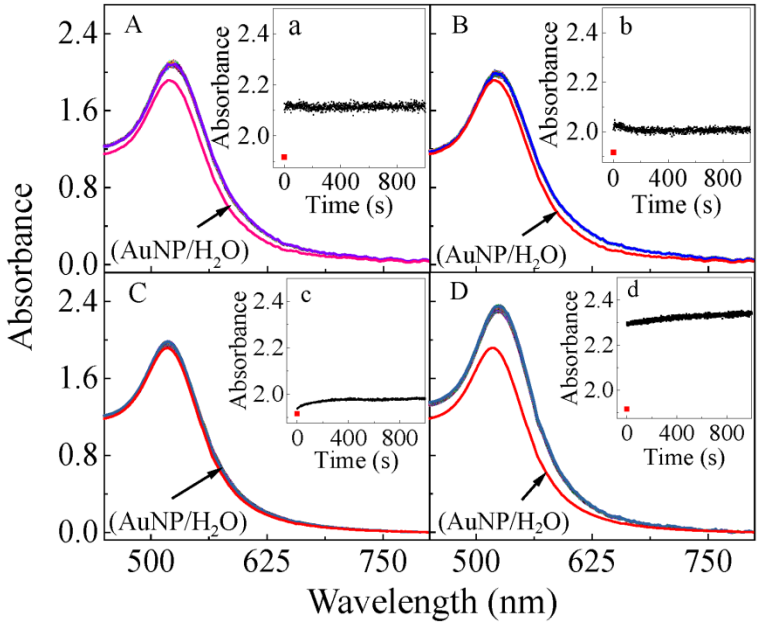

Figure 2.3 Time-resolved UV-vis spectra of AuNPs mixed with (A) PEG_{2K}-SH, (B) PEG_{5K}-SH, (C) PEG_{30K}-SH, and (D) BSA.

Note: The spectra in red are the AuNP control. The concentrations of AuNPs and PEG-SH (or BSA) are 7.1 nM and 10 μM, respectively. Insets are the time courses of AuNP UV-vis peak absorbances.

Table 2.1 AuNP LSPR and particle size change induced by PEG-SH and protein bovine serum albumin binding.

AuNP complex	Molecular weight of the polymer (g/mol)	DLS particle diameter (nm)	Increment in AuNP LSPR peak absorbance	Red-shift in AuNP LSPR peak wavelength (nm)
AuNP	NA	12.2 ± 1.3	0	0
AuNP/PEG_{2K}-SH	2000	18.1 ± 3.4	0.18	4
AuNP/PEG_{5K}-SH	5000	24.1 ± 5.9	0.08	2
AuNP/PEG_{30K}-SH	30 000	81.7 ± 10.7	0.06	0
AuNP/BSA	67 000	25.4 ± 2.8	0.43	6

Previous research established that the degree of AuNP and AgNP LSPR red-shift monotonically increase with the chain-lengths of saturation packed alkanethiols with numbers of carbons from 1 to 17.[94,95] Theoretical modeling shows that gold and silver LSPR red-shift and peak absorbance increases monotonically with increasing dielectric coating thickness until the thickness reaches a decay length of the LSPR evanescence field characteristic to the metal nanostructure,[94,96] This LSPR change is due to the increase in the dielectric constant of the dielectric shells immediately surrounding the metal surfaces.[94,96] The fact that PEG-SH also causes a red-shift in the AuNP LSPR peak wavelength and increment in the AuNP peak absorbance is consistent with the fact that PEG has a higher refractive index (n = 1.46) than water (n = 1.33) and a higher dielectric constant (n^2 = 2.1316) than water (n^2 = 1.7689). However, the PEG chain-length dependence of the pAuNP LSPR responses shown in Figure 2.3 and Table 2.1 is opposite to what has been observed for chain-length dependence of alkanethiols on gold and silver surfaces.[94-96] These results highlighted the challenge in using gold and silver LSPR to predict the ligand chain-length on the AuNP and AgNP surface. Besides the chain-lengths of the surface coating molecules, the packing density and the molecular

conformation of ligands on the metal surfaces also affects the noble metal LSPR response. In fact, the PEG chain-length dependence of the pAuNP LSPR features correlates very well with the PEG-SH chain-length dependence of the PEG-SH saturation packing density on AuNPs. Levine et al. showed that PEG_{2K}-SH and PEG_{5K}-SH packing densities on silica-core, gold-shell nanoparticles with a diameter of 110 nm were 46.7 ± 20.8 and 15.3 ± 7.9 pmol/cm^2, respectively.[60] Tsai et al. reported the saturation packing densities of PEG_{1K}-SH, PEG_{5K}-SH, and PEG_{20K}-SH on AuNPs 60 nm in diameter were 230, 26, and 8 pmol/cm^2, respectively.[21]

The fact that larger PEG-SHs induce smaller AuNP LSPR changes provides some validation for the proposal that PEG-SHs adopt a mushroom-like structure on AuNPs.[29,97] If the ethylene glycol units in these PEG-SHs spread on and are in direct contact with the AuNP surface, they should induce similar change in the dielectric constant of the medium immediately surrounding the AuNPs. Consequently, the degree of AuNP LSPR change induced by PEG_{2K}-SH, PEG_{5K}-SH, and PEG_{30K}-SH should have been much more similar. Using the PEG-SH packing densities reported by Levine et al,[60] the PEG-SH mass density on the AuNPs is very similar for PEG_{2K}-SH and PEG_{5K}-SH (93.4 ng/cm^2 for PEG_{2K}-SH vs. 76.5 ng/cm^2 for PEG_{5K}-SH).

Comparing the LSPR and DLS data obtained from pAuNPs (Figure 2.3 and Table 2.1) with data obtained from protein stabilized AuNPs, reveals significant differences in both the structures and conformations of proteins and PEG-SHs on AuNPs. Our recent research showed that different proteins, including BSA and both wild-type and mutated GB3 proteins that contain 0, 1, and 2 cysteine residues, respectively, all induce similar and significant changes to the AuNP LSPR peaks.[43,53] Since the GB3 variants and BSA

differ significantly in their molecular weights (~6208 g/mol for GB3 variants and 67,000 g/mol for BSA),[16,43,98] and their number of thiols (0,1, or 2 for the GB3 variants, 35 for BSA), these results suggest that proteins induce similar AuNP LSPR shifts regardless of their size and number of thiols.[43,53] This is in sharp contrast to the PEG-SH size dependence of the LSPR features of pAuNPs. The discrepancy is most likely due to the morphology differences between PEG-SHs and proteins on gold surfaces. Unlike PEG-SHs that bind monovalently to AuNPs as a mushroom-like structure, a protein can bind multivalently to AuNPs both specifically through its cysteine residues[16,45,99] and nonspecifically through electrostatic interactions, van der Waals forces, and so forth. Besides cysteine, many amino acid residues, including lysine, tyrosine, tryptophan, methionine, and histidine have high affinity to AuNPs. Consequently, a single protein molecule can form multiple anchoring points on the AuNP surface. For example, our recent research revealed that a BSA molecule has more than 20 stable anchoring points that can resist 2-MBI displacement from the AuNPs.[53] This large number of anchoring points should effectively confine all the amino acid residues within an extremely close vicinity of the AuNP surface. Therefore, the average distance between the protein amino acid residues and the AuNP surface is most likely significantly shorter than that between the ethylene glycol residues and the AuNP surface in pegylated AuNPs. This conclusion is supported by the DLS results (Table 2.1) that showed the thickness of the BSA overlayer is ~13 nm, which is ~5 times smaller than the thickness of the PEG_{30K}-SH overlayer on AuNPs. The DLS results are even more telling considering that the molecular weight of BSA is more than 2 times larger than that of PEG_{30K}-SH.

2.4.2 Adenine and 2-MBI adsorption onto AuNPs

The surface area and accessibility of the AuNP surface at the bottom of the PEG-SH mushroom caps and between the stems were probed through 2-MBI and adenine adsorption experiments (Figure 2.4). The addition of adenine or 2-MBI into as-synthesized colloidal AuNPs induced immediate AuNP aggregation and complete AuNP settlement after prolonged sample incubation times (Figures 2.4 A,B). AuNP settlement was observed by the complete disappearance of the AuNP LSPR feature in the UV-vis spectra obtained from the overnight aged AuNP/adenine and AuNP/2-MBI mixtures. The amount of adenine and 2-MBI adsorbed onto the as-synthesized AuNPs was 13.6 and 17.7 nmol, respectively, corresponding to packing densities of 410 and 535 pmol/cm^2 for adenine and 2-MBI, respectively. These quantifications are based on the difference between the amount of the ligand added into the colloidal AuNP solutions and that remaining free in the supernatant. The size and concentration of the AuNPs were estimated on the basis of the AuNP TEM image and UV-vis spectra (Figure 2.2).

The 2-MBI packing density deduced from the data in Figure 2.4 is very similar to the reported saturation 2-MBI packing density on AuNPs.[84] Adenine's lower saturation packing density than that of 2-MBI is also consistent with the difference in their molecular orientation on AuNPs. Both 2-MBI and adenine are planar molecules with similar molecular dimensions. However, 2-MBI is reported to adopt an upright conformation on AuNPs,[84] while adenine has been proposed to lie flat on the gold surface.[100] Consequently, 2-MBI has a smaller footprint than adenine on AuNPs. This conclusion was also supported by the adenine displacement studies on as-synthesized AuNPs (Figure 2.5), and the quantitative comparison of the 2-MBI and adenine

adsorption onto pAuNPs that will be discussed later in this work. The ligand displacement experiments showed that it takes 1.3 2-MBI molecules to displace one adenine molecule from AuNPs (Figure 2.5).

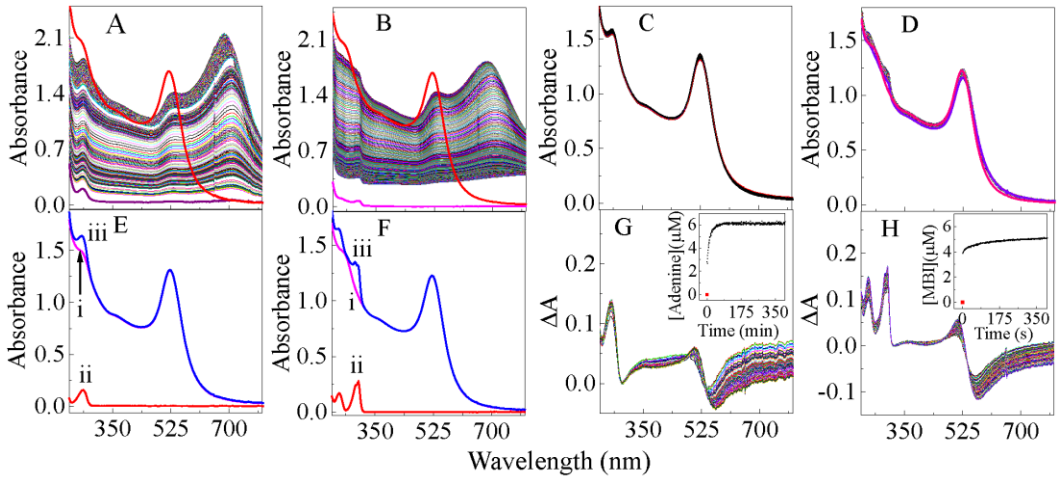

Figure 2.4 Time-resolved UV-vis spectra of (A) adenine/AuNPs, (B) 2-MBI/AuNP, (C) (AuNP/PEG$_{5K}$-SH)*24h*/adenine, and (D) (AuNP/PEG$_{5K}$-SH)*24h*/2-MBI mixtures. (E) Experimental spectra of (i) AuNP/PEG$_{5K}$-SH control, (ii) adenine control, and (iii) the mathematic additive spectrum of AuNP/PEG$_{5K}$-SH and adenine control. (F) Experimental spectra of (i) AuNP/PEG$_{5K}$-SH control, (ii) 2-MBI control, and (iii) the mathematic additive spectrum of AuNP/PEG$_{5K}$-SH and 2-MBI control. Difference spectra of (G) (AuNP/PEG$_{5K}$-SH)*24h*/adenine and (H) (AuNP/PEG$_{5K}$-SH)*24h*/2-MBI.

Note: Spectra in (A)-(D) were taken immediately after the addition of adenine or 2-MBI to AuNP or pAuNP mixtures. (G) Difference spectra obtained by subtracting the time-resolved UV-vis spectra of (AuNP/PEG$_{5K}$-SH)*24h*/adenine from the additive spectrum of AuNP/PEG$_{5K}$-SH control and adenine control (Figure 2E spectrum (iii)). (H) Difference spectra obtained by subtracting the time-resolved UV-vis spectra of (AuNP/PEG$_{5K}$-SH)*24h*/2-MBI from the additive spectrum of AuNP/PEG$_{5K}$-SH and 2-MBI control (Figure 2F spectrum (iii)). Insets in (G) and (H) are the amount of adenine and 2-MBI adsorbed onto the pAuNPs calculated by assuming that the UV-vis transition of 2-MBI and adenine on AuNPs were completely quenched. The nominal AuNP and ligand concentrations were 6.3 nM and 15 μM in both sample (A) and (B). The AuNP, PEG-SH, and adenine/2-MBI concentration in both samples (C) and (D) are 4.7 nM, 10 μM, and 10 μM, respectively.

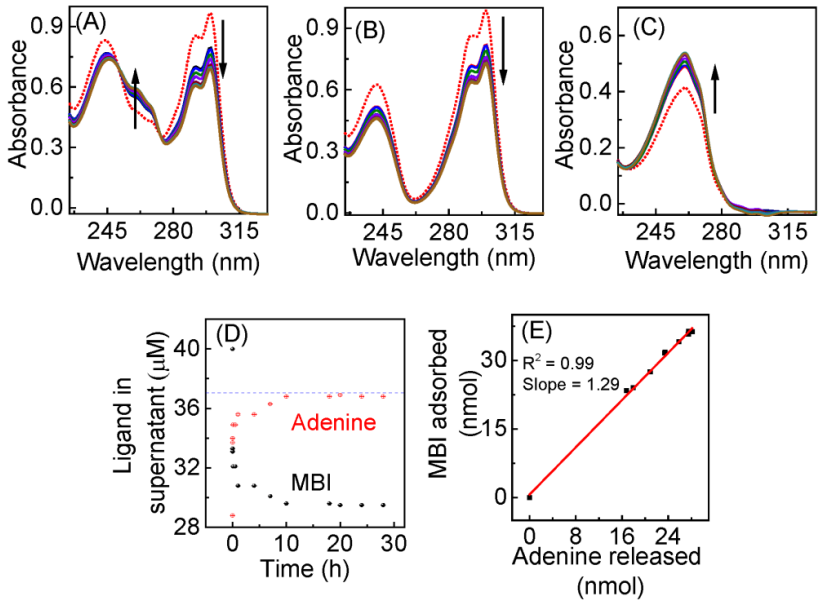

Figure 2.5 Time-dependent UV-vis study of adenine displacement from the as-synthesized AuNPs by 2-MBI.

Note: (A) Time-dependent UV-vis spectra obtained with the supernatant of the (AuNP/adenine)*12h*/2-MBI mixture. Red dotted spectrum was obtained with an adenine/2-MBI mixture control that represents the (AuNP/adenine)/2-MBI mixture before the onset of ligand exchange (t = 0). Time-dependent UV-vis spectra of (B) 2-MBI and (C) adenine obtained by decomposition of the 2-MBI and adenine mixture spectrum in (A) into 2-MBI and adenine component spectra. (D) Concentration of adenine (red spheres) and 2-MBI (black spheres) in the ligand exchange samples over the ligand exchange period. The dash line in (D) shows the total concentration of adenine in the ligand exchange samples. (E) Correlation between the amount of adenine released and 2-MBI adsorbed. The slope indicates that it takes 1.3 2-MBI molecules to replace one adenine on AuNPs. Detailed sample preparation and measurement procedure is discussed in experimental section.

No AuNP aggregation was observed when adenine or 2-MBI was added to fully pegylated AuNPs (Figure 2.4 C, D, and Figure 2.6). The peyglation was conducted using PEG-SH with a concentration of 10 μM. This PEG-SH concentration is in large excess relative to the AuNP monolayer packing capacity for PEG-SH. Indeed, if all the PEG-SH was adsorbed onto the AuNPs, the PEG-SH saturation packing density would be 723 pmol/cm^2, which is ~15 and ~47 times higher than the saturation packing density

reported for PEG_{2K}-SH and PEG_{5K}-SH on AuNPs by Levine *et al.*[60], and ~90 times higher than that reported for PEG_{20K}-SH.[21] The AuNP/PEG-SH mixture was incubated overnight to ensure that the PEG-SH reached saturation adsorption. As it will be shown later in this work, PEG-SH reaches an approximately steady-state adsorption within 3 h of sample incubation.

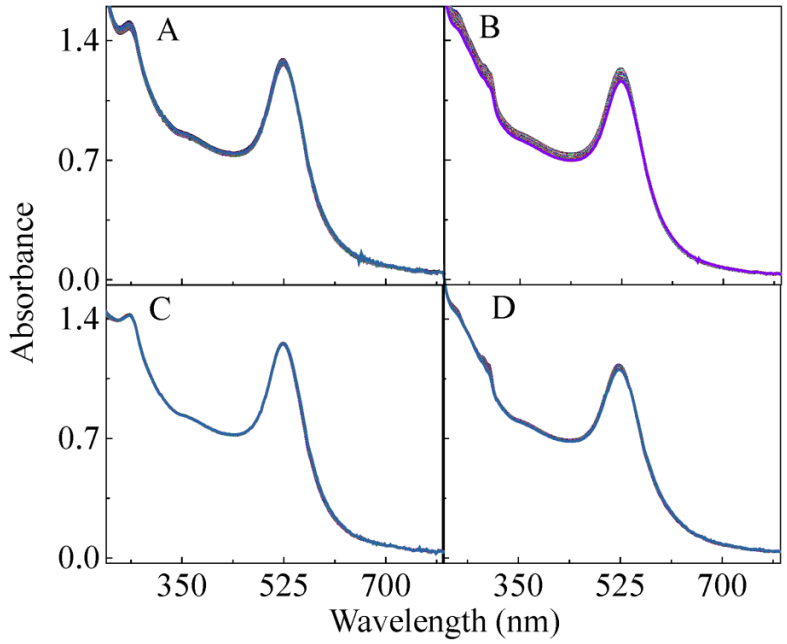

Figure 2.6 Time-resolved UV-vis spectra of (A) (AuNP/PEG_{2K}-SH)/adenine, (B) (AuNP/PEG_{2K}-SH)/2-MBI, (C) (AuNP/PEG_{30K}-SH)/adenine, and (D) (AuNP/PEG_{30K}-SH)/2-MBI mixtures.

Note: Spectra were taken right after the addition of adenine or 2-MBI to the pAuNP mixture. The AuNP, PEG-SH, and adenine or 2-MBI concentrations are 4.7 nM, 10, and 10 μM respectively. The spectra were acquired with 1 s interval for a total of 30 mins.

The amounts of 2-MBI and adenine adsorbed onto the overnight aged (AuNP/PEG_{5K}-SH)*24h*/2-MBI and (AuNP/PEG_{5K}-SH)*24h*/adenine were 13.5 ± 0.1 and 10.8 ± 0.2 nmol, respectively. These were determined on the basis of the concentration difference between the ligand added to the AuNP/PEG_{5K}-SH mixtures and that remaining

free in the supernatant after centrifugation removal of the AuNPs together with their surface adsorbates. These results indicate that the fraction of the AuNP surface area passivated by fully saturation packed PEG_{5K}-SH against both adenine and 2-MBI adsorption is ~20 (± 5)%. This conclusion was drawn by comparing the ligand adsorption onto the as-synthesized AuNPs and the pAuNPs. The detailed procedure for centrifugation quantification of ligand adsorption was described in the experimental section. The fact that there is a larger amount of 2-MBI adsorbed onto the pAuNPs than that for adenine is consistent with their adsorption onto the as-synthesized AuNPs, which provides further evidence supporting the hypothesis that adenine has a larger footprint than 2-MBI on AuNPs.

AuNP binding quenches both 2-MBI and adenine UV-vis adsorption. Such an effect is evident from the UV-vis difference spectra obtained by subtracting the time-resolved UV-vis spectra of the (AuNP/PEG_{5K}-SH)24h/ligand mixtures from the mathematically additive spectra of (AuNP/PEG_{5K}-SH) control and ligand controls (Figure 2.4 G, H). The adenine and 2-MBI UV-vis absorbance both monotonically increased in the difference spectra until each reached approximately a plateau when the 2-MBI and adenine reached equilibrium adsorption. The only sensible explanation for the decrease in the 2-MBI and adenine UV-vis absorbance is that AuNPs quench the ligand UV-vis transition due to a charge transfer between the ligand and AuNPs. Such a charge transfer has been demonstrated for aromatic organothiols including 2-MBI on as-synthesized or BSA stabilized AuNPs.[54,87] However, experimental demonstration of charge-transfer between adenine and plasmonic AuNPs has, to our knowledge, not been reported. The possibility that PEG-SHs quench 2-MBI or adenine UV-vis absorption was

excluded on the basis of the control experiments that show the mathematical additive spectra of the PEG-SH and ligand controls is identical to the experimental spectra of the corresponding PEG-SH/ligand mixtures (Figure 2.7).

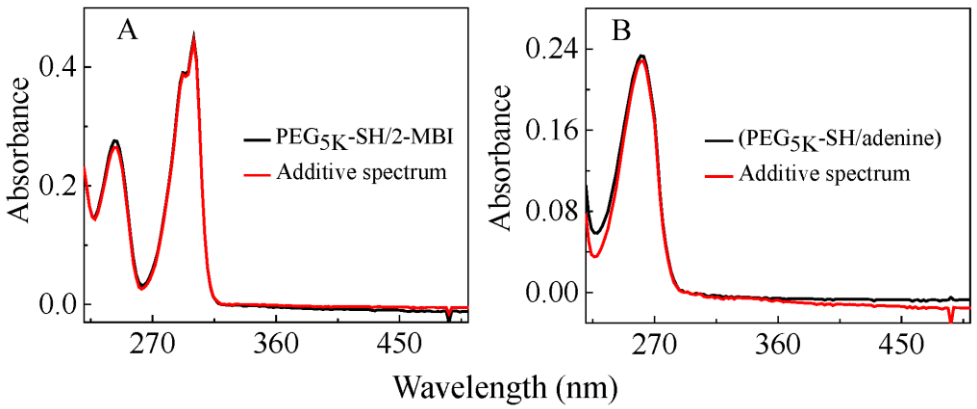

Figure 2.7 UV-vis spectra of (A) (PEG_{5K}-SH/2-MBI) and mathematical additive spectrum of (2-MBI/H_2O) + (PEG_{5K}-SH/H_2O) and (B) (PEG_{5K}-SH/adenine) and mathematical additive spectrum of (adenine/H_2O) + (PEG_{5K}-SH/H_2O).

Theoretically, 2-MBI and adenine can be adsorbed onto pAuNPs through one or more of the following three pathways: 1) by occupying the AuNP surfaces that are under the PEG-SH "mushroom cap" but not passivated by the "mushroom stem", 2) by displacing PEG-SH molecules previously attached to AuNPs, and 3) by binding to the PEG-SH overlayer on the AuNPs through possible intermolecular interactions between PEG-SHs and the ligand molecules. These interactions can be hydrogen bonding, van der Waals force, and electrostatic interactions and even physical entanglement. The last pathway was ruled out for both 2-MBI and adenine based on the PEG-SH concentration dependence of 2-MBI and adenine adsorption onto the (AuNP/PEG-SH)/ligand mixtures (Figure 2.8 and 2.9). This showed that the amount of 2-MBI and adenine adsorption

decreases with increasing PEG-SH concentration at the beginning and then reaches a plateau in (AuNP/PEG-SH)/ligand mixtures. If 2-MBI or adenine is adsorbed by binding to the PEG-SH overlayer, increasing the PEG-SH concentration should increase the amount of the ligand adsorbed.

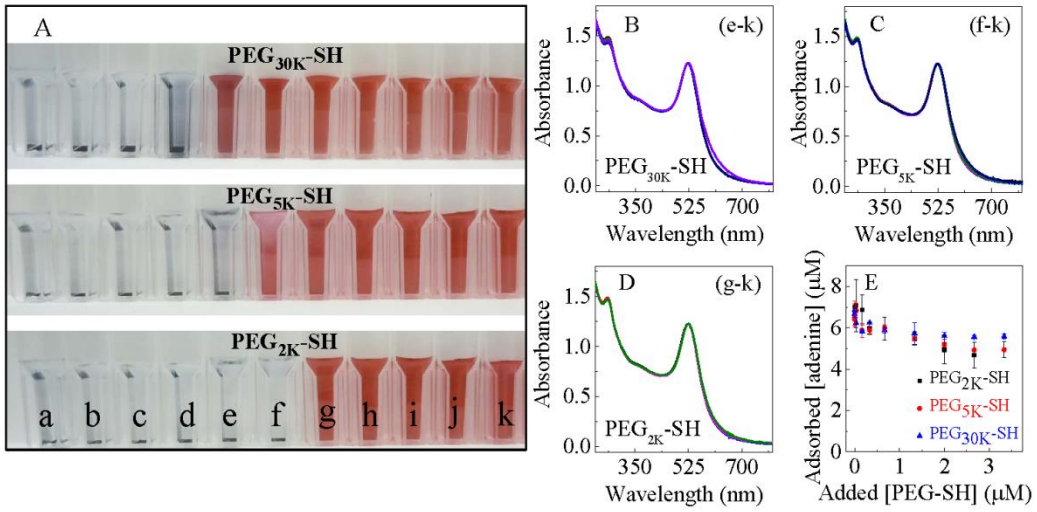

Figure 2.8 Photograph of (A) (AuNP/PEG-SH)*overnight*/adenine mixtures. (B), (C), and (D) normalized UV-vis spectra obtained with a subset of (AuNP/PEG_{30K}-SH)/adenine, (AuNP/PEG_{5K}-SH)/adenine, and (AuNP/PEG_{2K}-SH)/adenine mixtures that have no significant AuNP aggregation. (E) The amount of adenine adsorbed onto the pAuNPs as a function of PEG-SH concentration.

Note: The PEG-SH concentrations in vials ***a*** to ***k*** in (A) are 0, 0.0003, 0.003, 0.03, 0.17, 0.3, 0.7, 1.3, 2, 2.7, and 3.3 μM, respectively. Concentrations of AuNPs and adenine in all the samples are 4.7 nM and 10 μM, respectively. The normalization in (B)-(D) is performed by scaling the peak UV-vis absorbance for the different samples to be the same.

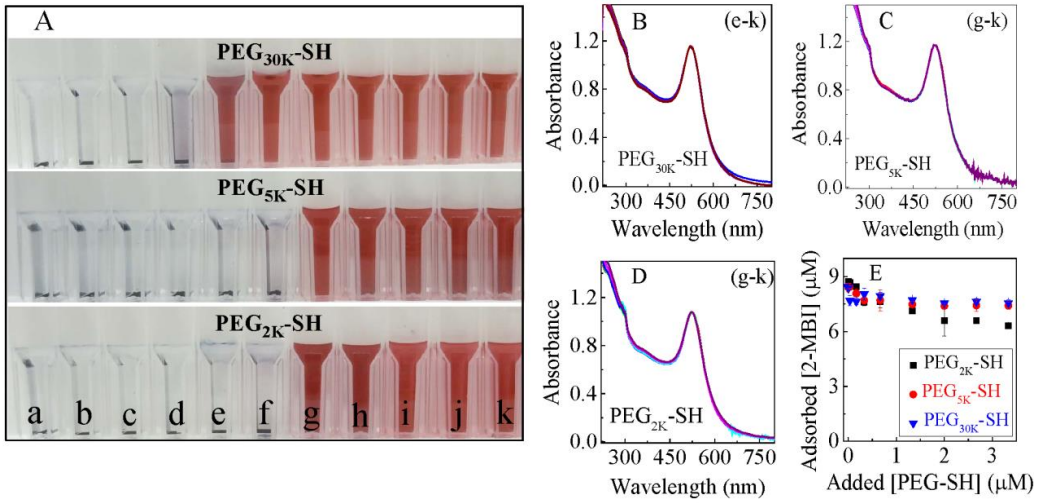

Figure 2.9 Photograph of (A) AuNPs mixed with PEG_{30K}-SH, PEG_{5K}-SH and PEG_{2K}-SH, respectively, with the subsequent addition of 2-MBI. (B), (C), and (D) normalized UV-vis spectra obtained with a subset of ((AuNP/PEG_{30K}-SH)/2-MBI), ((AuNP/PEG_{5K}-SH)/2-MBI), and ((AuNP/PEG_{2K}-SH)/2-MBI) mixtures that have no significant AuNP aggregation. (E) The amount of 2-MBI adsorbed onto the pAuNPs as a function of PEG-SH concentration.

Note: The PEG-SH concentrations in vials a to k are 0, 0.0003, 0.003, 0.03, 0.17, 0.3, 0.7, 1.3, 2, 2.7, and 3.3 μM, respectively. Concentrations of AuNPs and 2-MBI are 4.3 nM and 10 μM, respectively.

The second pathway is completely excluded for adenine adsorption onto the pAuNPs because adenine has a much lower binding affinity to AuNPs than organothiols. Control experiments showed that adenine on as-synthesized AuNPs can be completely displaced by 1-propanethiol, but not vice versa (Figure 2.10). This result strongly indicates that adenine can only bind to pAuNPs through the first pathway, that is, by occupying the AuNP surfaces beneath the PEG-SH mushroom caps.

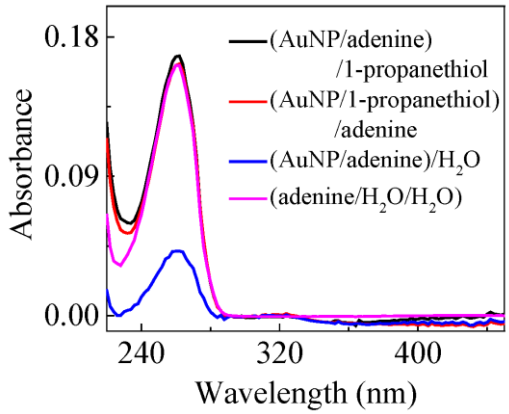

Figure 2.10 UV-vis spectra of (black) ((AuNP/adenine)/1-propanethiol), (red) ((AuNP/1-propanethiol)/adenine), (blue) ((AuNP/adenine)/H_2O), and (magenta) (adenine/H_2O/H_2O).

Note: The nominal AuNP, adenine, and 1-propanethiol concentrations were 4.7 nM, 10 μM, and 10 μM respectively.The fact that the amount of free adenine among (AuNP/adenine)/1-propanethiol, (AuNP/1-propanethiol)/adenine, and (adenine/H_2O)/H_2O is the same indicates that 1) 1-propanethiol completely displaced adenine adsorbed onto AuNPs and 2) adenine can not displace 1-propanethiol from the AuNPs.

The 2-MBI adsorption onto the pAuNPs is also primarily through the first pathway. This conclusion is drawn from the PEG-SH and 2-MBI concentration dependence of the amount of 2-MBI adsorbed onto the (AuNP/PEG_{5K}-SH)*overnight*/2-MBI (Figure 2.9 and 2.11). Following the initial decrease in the amount of 2-MBI adsorption with increasing PEG-SH concentration, further increasing the PEG-SH concentration has no significant effect on the amount of 2-MBI adsorption (Figure 2.9). In addition, once 2-MBI reaches saturation adsorption onto pAuNPs, further increasing the 2-MBI concentration has no significant effect on the amount of the 2-MBI adsorbed (Figure 2.11). If 2-MBI displacing PEG-SH is significant in 2-MBI adsorption onto pAuNPs, one would expect that the amount of 2-MBI adsorbed onto pAuNPs should

monotonically increase with increasing 2-MBI concentration, or decrease with increasing PEG-SH concentration in (AuNP/PEG_{5K}-SH)*overnight*/2-MBI.

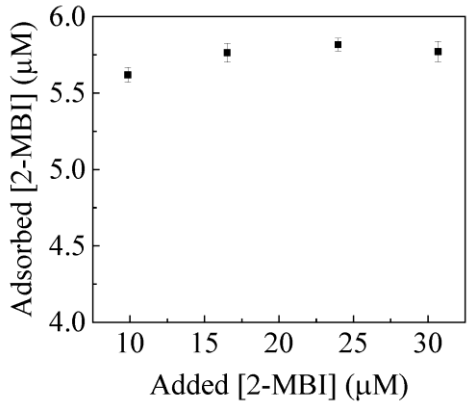

Figure 2.11 The amount of adsorbed 2-MBI to pAuNPs from different concentrations of added 2-MBI.

Note: AuNP and PEG_{5K}-SH concentrations were 4.7 nM and 10 μM, respectively. (AuNP/PEG_{5K}-SH) mixtures were incubated overnight and different concentrations of 2-MBI (10, 16.7, 23.3, and 30 μM) were added to the mixture and incubated for 7 h. The UV-vis spectra were obtained after the centrifugation.

The threshold PEG-SH concentration to stabilize AuNPs from either 2-MBI- or adenine-induced AuNP aggregation is significantly smaller for PEG_{30K}-SH than that for PEG_{5K}-SH and PEG_{2K}-SH (Figures 2.8 and 2.9). The threshold PEG-SH concentrations preventing AuNPs from adenine-adsorption-induced aggregation are ~0.7, ~0.3, and ~0.17 μM for PEG_{2K}-SH, PEG_{5K}-SH, and PEG_{30K}-SH, respectively, and those for preventing 2-MBI adsorption-induced aggregation are ~0.7, ~0.7, and ~0.17 μM for PEG_{2K}-SH, PEG_{5K}-SH, and PEG_{30K}-SH, respectively. This result indicates that the larger the PEG-SH molecule, the more effective it is in preventing ligand co-adsorption induced aggregation of AuNPs.

The ligand adsorption data in Figure 2.8 are consistent with the PEG-SH packing densities reported by Levin et al.[60] and Tsai et al.,[21] but argues against the exceedingly large PEG_{2K}-SH and PEG_{5K}-SH saturation packing densities on AuNPs recently reported by Rahme et al.[66] The latter reported the saturation packing density of PEG-SHs on AuNPs are 652 and 398 pmol/cm^2 for PEG-SHs with molecular weight of ~2000 and ~5000 g/mol, respectively.[66] The data in Figure 2.8 strongly suggest that the PEG-SHs reached saturation adsorption on AuNPs at PEG-SH concentrations of ~2 μM and ~1.3 μM for PEG_{2K}-SH and PEG_{5K}-SH, respectively. This conclusion is drawn from the observation that further increasing the PEG-SH concentration in the respective (AuNP/PEG-SH)/adenine mixtures does not reduce adenine adsorption (Figure 2.8). The PEG-SH packing densities at the saturation concentration are 145 and 94 pmol/cm^2 for PEG_{2K}-SH and PEG_{5K}-SH, respectively. These values are significantly smaller than those reported by Rahme et al.[66] It is important to note that the PEG-SH saturation packing densities estimated on the basis of our adenine adsorption should be the upper limit of the saturation PEG-SH packing density. This is because we assumed that all the PEG-SH molecules at these saturation concentrations are completely adsorbed onto the AuNPs.

The adenine and 2-MBI adsorption data in Figures 2.8 and 2.9 also provide direct evidence that there is a large fraction of free AuNP surface (not passivated) at the bottom of the PEG-SH overlayer and this surface is accessible for ligand adsorption. Evidently, no adenine or 2-MBI adsorption would be possible if the PEG-SH completely covered and passivated the AuNP surfaces. On the basis of the difference between adenine adsorbed onto the as-synthesized AuNPs and the fully peylgated AuNPs, we further estimated that the maximum fractions of AuNP surface that are passivated by PEG-SHs

against further ligand adsorption are ~25%, ~20%, and ~9% for PEG_{2K}-SH, PEG_{5K}-SH, and PEG_{30K}-SH, respectively. This result indicates that while the nominal footprint of a PEG-SH increases with increasing PEG-SH chain-length, the fraction of the AuNP surface passivated by a PEG-SH decreases as its molecular weight increases. It is gratifying that passivated AuNP fractions estimated by ligand adsorption method are qualitatively consistent with that estimated on the basis of the AuNP red-shift introduced by the model PEG-SHs. Using Mie theory,[101] we calculate the AuNP LSPR red-shift of the AuNPs when the environmental dielectric constant is changed. The environmental dielectric constant is calculated by averaging the dielectric constants of water (n^2 = 1.7689) and PEG-SH (n^2 = 2.1316) weighted by their volume around the AuNPs. The AuNP LSPR red-shift versus the passivated fractions is shown in Figure 2.12. The calculations show that the resonance wavelength red shifts by 1, 2, and 2.5 nm when the passivated fraction is at 10, 20, and 25% which is reasonably close to the measured shift of 0, 2.5 and 4 nm in the experiments. The calculations solidify the experimental measurement and also support the proposed mushroom configuration for PEG-SH on AuNPs.

Unlike the large amount of adenine and 2-MBI that can be adsorbed onto pAuNPs (Figures 2.8 and 2.9), no protein adsorption was observed when BSA labeled with fluorescein isothiocynate was added to pAuNPs. Since proteins are known to have high binding affinities to AuNP surfaces, this result implies that ligand molecules have a size threshold in order to occupy the AuNP surface under the PEG-SH mushroom caps. In other words, we believe that PEG-SHs can prevent protein adsorption onto AuNPs

primarily due to steric hindrance, not because PEG-SHs completely passivate the AuNP surfaces.

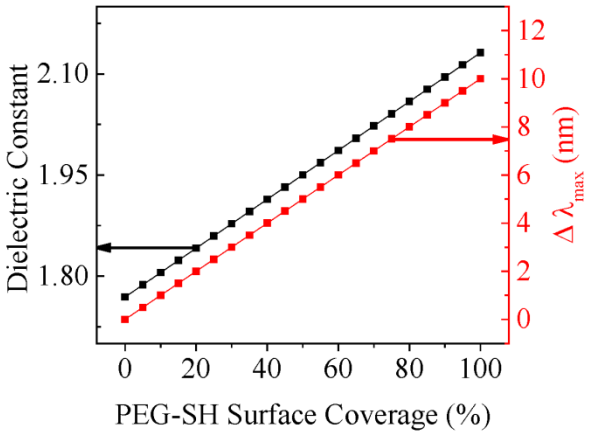

Figure 2.12 Theoretical prediction of the AuNP LSPR peak shift (red axis) induced by PEG-SH with different surface coverage, calculated with Mie theory.

Note: The environmental dielectric constant (left axis) is calculated by averaging the dielectric constants of water ($n^2 = 1.7689$) and PEG-SHs ($n^2 = 2.1316$) weighted by their volume around the AuNPs. This PEG-SH dielectric constant was assumed to be independent of the PEG-SH chain-lengths and sulfuhydryl group, and it is assumed to be the same as that for PEG-SH with an average molecular weight of 400 g/mol ($n^2 = 2.1316$) (http://www.sigmaaldrich.com). The AuNPs were assumed to be perfectly spherical with diameter of 13 nm in diameter

2.4.3 Effect of aging (AuNP/PEG-SH) on subsequent ligand adsorption

Our recent research established that ligand adsorption is an effective tool to probe protein structure and conformation on AuNPs.[53] Studying the effect of aging the AuNP/PEG-SH mixtures on their subsequent 2-MBI or adenine adsorption should also provide critical information regarding the PEG-SH binding kinetics on the AuNPs. Conceivably, once PEG-SHs reach a steady-state adsorption and conformation onto the AuNPs, further aging of the AuNP/PEG-SH mixtures should not have any significant

effect on the kinetics and amount of ligand adsorption. Figure 2.13 shows the experimental results of an aging study conducted using PEG_{5K}-SH as the model PEG-SH. After the initial three hours, further aging of the AuNP/PEG_{5K}-SH mixture has no significant effect on the kinetics and adsorption capacity for either 2-MBI or adenine adsorption (Figure 2.13). This result indicates that the PEG_{5K}-SH reaches a steady-state adsorption onto the AuNP surface after three hours of sample incubation. The similarity in the effect of aging (AuNP/PEG_{5K}-SH) mixtures on both 2-MBI and adenine adsorption is consistent with our conclusion that both 2-MBI and adenine adsorption follow primarily the same pathway for adsorption onto the pAuNPs.

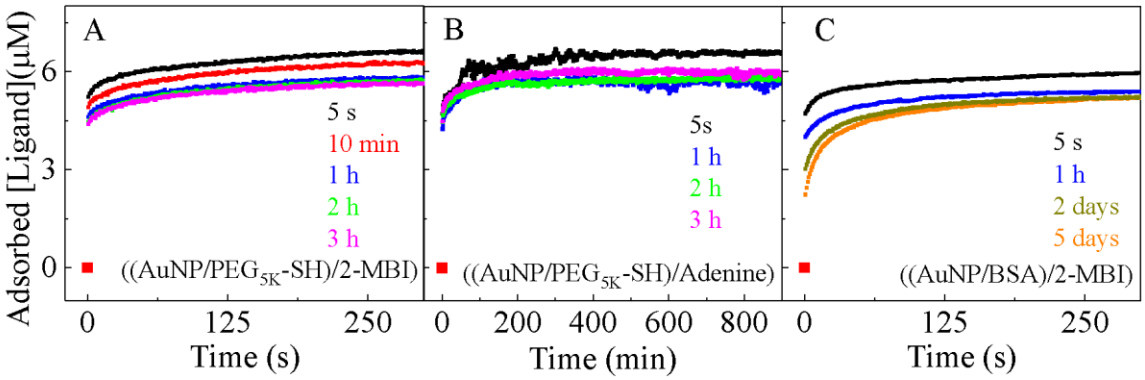

Figure 2.13 Effect of aging (AuNP/PEG_{5K}-SH) mixtures on subsequent (A) 2-MBI and (B) adenine adsorption. (C) Effect of aging (AuNP/BSA) mixtures on subsequent 2-MBI adsorption.

Note:The AuNP, PEG_{5K}-SH or BSA, and 2-MBI or adenine concentrations are 4.7 nM, 10 μM, and 10 μM, respectively.

A similar aging effect has been observed for (AuNP/PEG_{2K}-SH) and (AuNP/PEG_{30K}-SH) for their subsequent 2-MBI adsorption (Figure 2.14), suggesting that the kinetics of PEG-SH binding onto AuNPs does not depend significantly on the molecular weights of the model PEG-SH molecules used in this work. However, the

effect of aging (AuNP/PEG-SH) on 2-MBI adsorption is remarkably different from that of aging (AuNP/BSA) on subsequent 2-MBI adsorption (Figure 2.13). It is important to note that the same batch of AuNPs was used in the (AuNP/PEG-SH) and (AuNP/BSA) aging studies, facilitating a head-to-head comparison of the aging effect between pAuNPs and BSA coated AuNPs. An attempt to study the effect of aging (AuNP/BSA) on adenine adsorption was unsuccessful because UV-vis quantification of adenine was complicated by the fact that adenine and BSA UV-vis absorptions overlap at 260 nm.

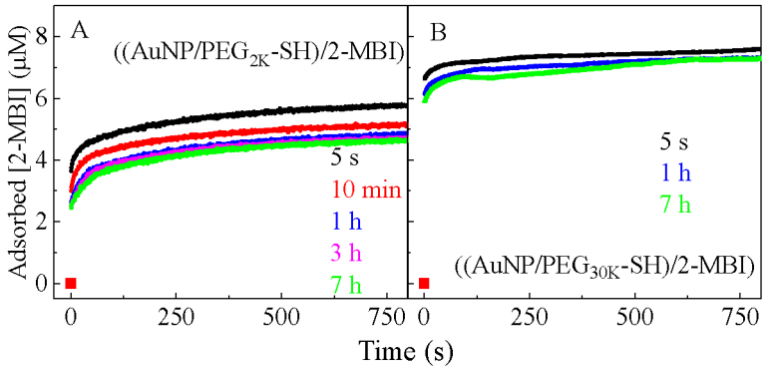

Figure 2.14 Effect of aging (A) (AuNP/PEG_{2K}-SH) and (B) (AuNP/PEG_{30K}-SH) on subsequent 2-MBI adsorption.

Note: (AuNP/PEG_{2K}-SH) mixtures were aged for 5s (black), 10 min (red), 1h (blue), 3h (magenta), and 7h (dark green). (AuNP/PEG_{30K}-SH) mixtures were aged for 5s (black), 1h (blue), and 7h (green). The final concentration of AuNPs was 4.7 nM. The concentrations of both PEG-SH and 2-MBI were 10 μM.

Unlike PEG-SH that reaches a steady-state adsorption onto AuNPs within a few hours of sample incubation, BSA does not reach equilibrium adsorption onto AuNPs even after 2 days of sample incubation. The latter finding is consistent with our recent work.[53] This difference can be explained based on a comparison of PEG-SH and BSA structural characteristics. PEG-SH is a simple synthetic polymer that can bind to AuNPs

presumably only through its terminal –SH group. However, BSA has 35 cysteine groups that can bind covalently to AuNPs, and many other amino acids such as lysine that are known to have a high binding affinity to gold surfaces. As a result, BSA can be initially adsorbed onto the AuNPs through one or more amino acids followed by conformational change that likely leads to formation of one or more covalent S-Au bonds. The data in Figure 2.13 C showed that these conformation changes last at least a few days for proteins on AuNPs.

The amount of 2-MBI adsorbed onto pAuNPs is significantly higher than that adsorbed onto the BSA coated AuNPs. This result indicates that the fraction of AuNP surface passivated by PEG_{5K}-SH is significantly smaller than that passivated by BSA even though the literature packing density of PEG_{5K}-SH is ~10 times higher than that for BSA (46 to 230 pmol/cm^2 for PEG_{5K}-SH[21,60,83] vs. 6.6 to 10 pmol/cm^2 for BSA[46,53,98]). This difference is consistent with our hypothesis that BSA binds multivalently to AuNPs, while PEG-SH is tethered monovalently to AuNPs through its terminal –SH group. Regardless, the result in Figure 2.13 indicates that BSA is far more effective than PEG-SHs in passivating the AuNP surface against ligand adsorption.

2.4.4 Adenine binding affinity on AuNPs

Since PEG-SHs can stabilize AuNPs from ligand-adsorption-induced aggregation without significantly reducing the AuNP ligand binding capacity, pAuNPs can serve as a valuable platform for studying ligand binding and exchange on AuNPs. For example, using pAuNPs, we demonstrated in Figure 2.4 that adenine binding to AuNPs led to the quenching of adenine UV-vis absorption. Such an observation could not be made with the as-synthesized AuNPs because adenine adsorption induces AuNP aggregation.

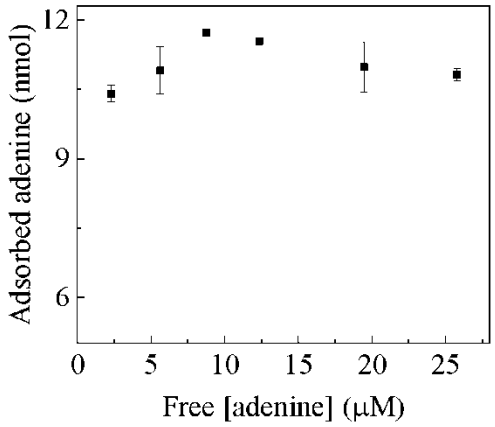

Figure 2.15 Adsorption isotherm of adenine on AuNPs pegylated with PEG_{30K}-SH

Note: The concentrations of the PEG_{30K}-SH and AuNPs are10 μM and 4.7 nM, respectively. The AuNP/PEG_{30K}-SH mixtures were incubated for 12 h before the adenine addition. The error bars represent one standard deviation with three independent measurements.

Figures 2.15 and 2.16 demonstrate another example of pAuNP application for ligand interaction with AuNPs, the estimation of the adenine binding affinity to AuNPs. It can be deduced from the adenine adsorption isotherm in Figure 2.15 that the adenine binding affinity to AuNPs should be significantly higher than 10^5 M^{-1}. This conclusion is drawn by assuming that adenine binding to the pAuNPs follows the Langmuir adsorption isotherms. If the AuNP/adenine binding constant is smaller than or equal to 10^5 M^{-1}, the amount of adenine adsorbed onto the pAuNPs should be significantly different when the adenine concentrations are 5 and 25 μM. Pinpointing the exact adenine binding affinity to AuNPs is currently impossible with the ligand adsorption data in Figure 2.15. However, the upper limit of the adenine binding affinity to AuNPs should be significantly smaller than 4.5×10^6 M^{-1}, the binding constant reported for 2-MBI adsorption onto AuNPs at neutral pH.[84,102] This conclusion is drawn on the basis of an adenine/2-MBI displacement

experiment conducted on the as-synthesized AuNPs (Figure 2.5), and the adenine/2-mercaptoethanol (ME) displacement experiment that used pAuNPs (Figure 2.16). Adenine on the pAuNPs was rapidly displaced by ME, but not vice versa (Figure 2.16). Most adenine displacement in the pAuNPs was observed within the first 10 mins after the addition of ME. This rapid ligand displacement (Figure 2.16), in combination with the rapid ligand adsorptions (Figure 2.4) on the pAuNPs, confirmed that the PEG-SH overlayer is highly porous and permeable for small ligands such as 2-MBI, adenine, and ME.

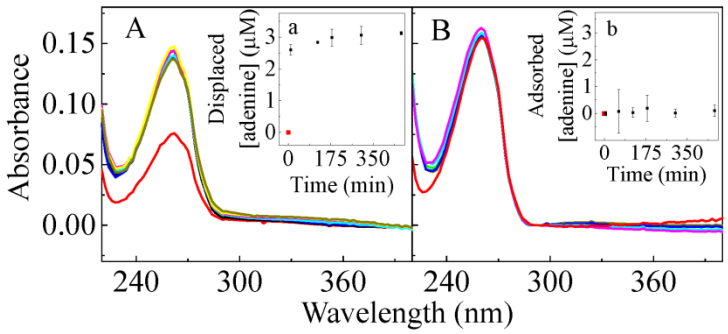

Figure 2.16 UV-vis study of adenine/ME exchange on pAuNPs. Time-dependent UV-vis spectra obtained with (A) ((AuNP/PEG$_{30K}$-SH)*5h*/adenine)*12h*/ME and (B) ((AuNP/PEG$_{30K}$-SH)*5h*/ME)*12h*/adenine.

Note: The spectra in red were taken using the supernatant of the controls where the fourth component in the respective samples was replaced with water. The insets show the changes of adenine concentration in the supernatant of the ligand binding solution as a function of time after the addition of the fourth component in the respective sample mixture. The nominal AuNP, PEG$_{30K}$-SH, adenine, and ME concentrations are 3.55 nM, 7.5 μM, 7.5 μM, and 7.5 μM respectively. Detailed sample preparation and measurement procedures are in the experimental section.

2.5 Conclusions

In summary, using adenine and 2-MBI as model ligands, we provided an experimental confirmation that PEG-SH molecules with a molecular weight equal or larger than 2000 g/mol adopt a mushroom-like configuration on AuNP surfaces in water. A large fraction of the AuNP surface under the PEG-SH mushroom caps is available for ligand adsorption and exchange. UV-vis measurements revealed that AuNP binding quenches the UV-vis absorption of both adenine and 2-MBI. This information could not be obtained with as-synthesized AuNPs because both adenine and 2-MBI adsorption induce spontaneous AuNP aggregation. In addition to providing new insight into the assembly kinetics and conformations of PEG-SHs on AuNPs, this work also demonstrated that pAuNPs are an effective platform for studying ligand adsorption and exchange. Furthermore, this work could also lead to new applications that utilize the AuNP surface under PEG-SH overlayer for biomedical imaging, drug delivery, and catalysis.

Notes: This work has been previously published: Siriwardana, K.; Gadogbe, M.; Ansar, S. M.; Vasquez, E. S.; Collier, W. E.; Zou, S.; Walters, K. B.; Zhang, D., Ligand Adsorption and Exchange on Pegylated Gold Nanoparticles. *J. Phys. Chem. C* **2014**, *118*, 11111-11119.

CHAPTER III

STUDYING THE EFFECT OF CYSTEINE RESIDUES ON PROTEIN INTERACTIONS WITH SILVER NANOPARTICLES

(Published in *J. Phys. Chem. C* **2015,** *119*, 2910-2916)

3.1 Abstract

Studies of protein and organothiol interactions with silver nanoparticles (AgNPs) are important for understanding AgNP nanotoxicity, antimicrobial activity, and material fabrications. Reported herein is a systematic investigation of the effects of both reduced and oxidized protein cysteine residues on protein interactions with AgNPs. The model proteins included wild-type and mutated protein GB3 variants that contain 0, 1, or 2 reduced cysteine residues, respectively. Bovine serum albumin (BSA) that contains a total of 34 oxidized (disulfide-linked) cysteine residues and one reduced cysteine residue was also included. Protein cysteine content has no detectable effect on the kinetics of protein/AgNP binding. However, only proteins that contain reduced cysteine residues induce significant AgNP dissolution. Proteins can slow down, but do not prevent the AgNP dissolution induced by subsequently added organothiols. The insights provided in this work are important to the mechanistic understanding the AgNP stability in biofluids that are rich in proteins and amino acid thiols.

3.2 Introduction

Silver nanoparticles (AgNPs) have been widely used in biosensing, chemical catalysis, and solar energy harvesting.[103-105] One key complication in understanding the AgNP structure and properties is the AgNP's susceptibility to oxidation and dissolution. It is generally accepted that the surface silver atoms in as-synthesized AgNPs are oxidized and are likely silver oxide.[106-108] Without silver chelating agents, the as-synthesized AgNPs covered in insoluble silver oxide can be stable in aqueous solution for up to several months under ambient conditions. However, organothiols can continuously react with AgNPs, converting the silver oxide and silver atoms into water-insoluble silver thiolate salts.[40] The rate of such conversion depends strongly on the organothiol structure and conformation. For example, aromatic organothiols produce large silver-thiolate precipitates that can accumulate on the AgNP surface or settle elsewhere,[40] while long-chain 1-alkanethiols on the AgNP are mostly adsorbed as a monolayer.[37,41] The latter is due to the surface silver-alkanethiolate salts that are highly ordered on the AgNP surfaces, which impose a strong steric hindrance preventing further alkanethiol reaction with AgNPs. In contrast, alkanethiols on AuNPs are highly disordered regardless of their carbon-chain length.[109]

We recently investigated the effect of cysteine on protein binding to AuNPs.[43] One key observation was that cysteine has no significant effect on the kinetics of the protein/AuNP binding, but it plays a critical role in stabilizing the AuNPs against organothiol displacement and organothiol-induced AuNP aggregation. This finding implies that protein and AuNP binding is initiated by forces including long range

electrostatic and van der Waals forces, but not the covalent cysteine/AuNP bonding that forms only after the protein is adsorbed and deformed onto the AuNPs.

Reported herein is a systematic investigation of the effect of protein cysteine residues on protein interactions with AgNPs in water. The model proteins include bovine serum albumin (BSA), and wild-type and mutated third IgG-binding domain of protein G (GB3) (Figure 3.1). These proteins were also used in our study of protein binding with AuNPs,[43,53,54] which enables us to compare and contrast the protein binding with AuNPs and AgNPs. The wild-type GB3 protein contains 56 amino acid residues with no cysteine ($GB3_0$).[110,111] However, the mutated GB3 variants contain one ($GB3_1$) and two cysteine residues ($GB3_2$), respectively. The lysine residue in $GB3_0$ at the 19th position was replaced by a cysteine residue in $GB3_1$, while both the threonine and lysine at the 11th and 19th positions in $GB3_0$ were replaced by cysteines in $GB3_2$ (Figure 3.1). BSA has 17 interchain disulfide bonds formed by 34 oxidized cysteines and 1 free sulfhydryl group in one reduced cysteine.[112]

Organothiols have been used as probe molecules to study the protein structure and conformational modification when adsorbed onto AuNPs.[53,54] The protein overlayer on AuNPs is highly permeable to small organothiol molecules that can trigger protein desorption or be adsorbed with protein onto the AuNP surface. [43,54] In this work, a series of organothiols were employed to investigate the organothiols' interaction with AgNPs that are pretreated with proteins. This study is critical for evaluating the effectiveness of protein in stabilization of AgNPs to organothiol-induced AgNP aggregation and dissolution. Such information is particularly relevant for AgNP biological applications because proteins and amino acid thiols are abundant in biofluids. For the sake of

simplicity, we will use the notation of A/B to represent a two-component solution, and (A/B)/C a three-component solution in which the two components inside the parenthesis are mixed first before the addition of the third component.

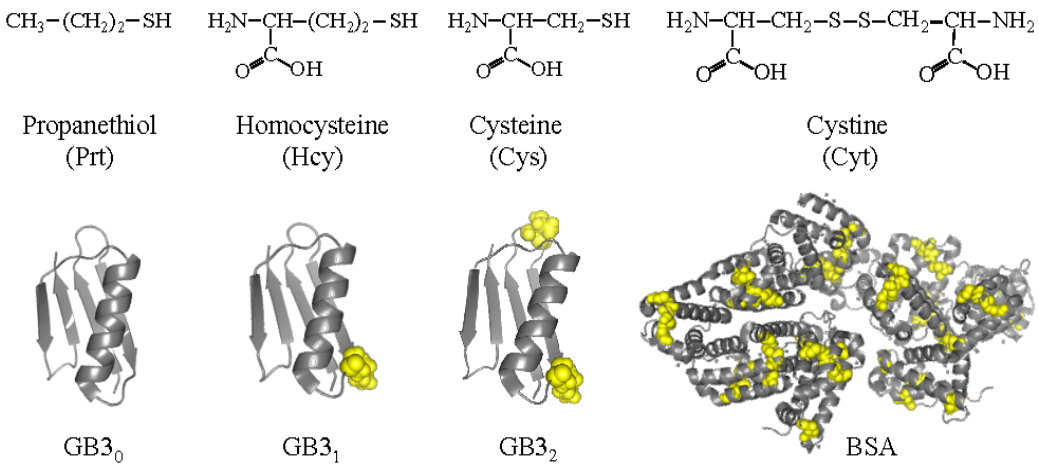

GB3$_0$: MQYKLVINGK TLKGETTTKA VDAETAEKAF KQYANDNGVD GVWTYDDATK TFTVTE
GB3$_1$: MQYKLVINGK TLKGETTTCA VDAETAEKAF KQYANDNGVD GVWTYDDATK TFTVTE
GB3$_2$: MQYKLVINGK CLKGETTTCA VDAETAEKAF KQYANDNGVD GVWTYDDATK TFTVTE

Figure 3.1 (Top) Model organothiols used. (Bottom) Cartoon representation of GB3 (from PDB 2-OED) and BSA (from PDB 4OR0) proteins and amino acid sequence of GB3 variants.

Note: Cysteine residues are highlighted in yellow CPK spheres. Image created using PyMOL software.

The model organothiols used in this study include the amino acid thiols cysteine (Cys) and homocysteine (Hcy), and the highly hydrophobic oragnothiol propanethiol (Prt). We also included the disulfide-linked organothiol cystine (Cyt) that is composed of two disulfide-linked (oxidized) Cys molecules. Investigation of both the Cys and Cyt interactions with AgNPs allows us to compare the reactivity of reduced (R-SH) and oxidized (R-S-S-R) organothiols with AgNPs.

It is important to note that there are extensive literature reports on single component protein or organothiol interactions with nanoparticles.[31,33,113-121] However, cross-comparisons of the chemical reactivity of reduced and oxidized organothiols with AgNPs are to our knowledge very limited, so is the comparison of the effects of reduced and oxidized protein cysteine residues on the protein interactions with AgNPs. Filling this knowledge gap is critical for deepening our understanding of molecular-level interfacial interactions of AgNPs. As an example, the time-dependent surface enhanced Raman spectroscopic (SERS) measurement in this work revealed that Cyt initially binds to AgNP through its carboxylate group. Its disulfide bond is cleaved only after relatively long sample incubation of the Cyt/AgNP mixture. This result may explain the literature controversy on the structure of Cyt on AgNP surfaces.[117,122]

3.3 Experimental section

3.3.1 Materials and instruments

All chemicals including BSA were purchased from Sigma-Aldrich. The citrate-reduced AgNPs with nominal diameter of 10 nm (Figure 3.2) were purchased from Nanocomposix Inc. AgNPs synthesized in house with the Lee and Meisel method have also been used in this work.[14] Similar experimental observations were seen with both the in-house and commercial AgNPs. However, the data presented in this chapter are all obtained with the commercial citrated reduced AgNPs because of their smaller particle size and more uniform particle size distribution. Indeed, because of their smaller size (10 nm versus ~65 nm for the in-house AgNPs), the protein- and organothiol-induced AgNP structural modifications are much more readily detectable with the commercial AgNPs. Nanopure water (Thermo Scientific, 18.2 MΩ cm) was used in sample preparation. An

Olis HP 8452 A diode array spectrophotometer was used for the time-resolved UV-vis measurements. All solutions were stored in a refrigerator at ~ 4 °C. Normal Raman and SERS spectra were acquired using the Lab Ram HR800 confocal Raman microscope system with a 633 nm Raman excitation laser.

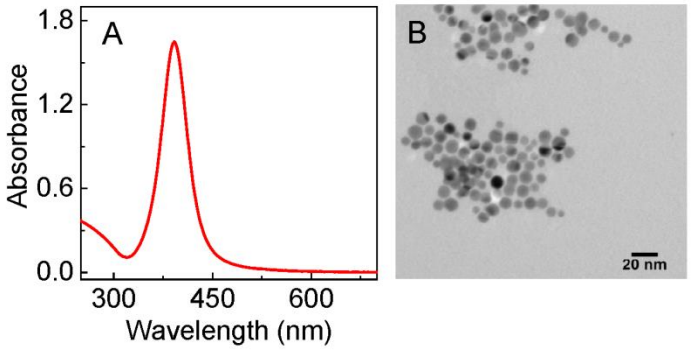

Figure 3.2 (A) UV-vis spectrum and (B) TEM image of commercial AgNPs.

Note: UV-vis spectrum was obtained by using a two times diluted sample of as-received commercial AgNPs. The particle size is 10 nm in diameter. The nominal concentration of AgNPs is 3.9 nM.

3.3.2 Synthesis of GB3 and GB3 variants

A pET-11b plasmid encoding for GB3 was provided as a generous gift from Ad Bax (National Institutes of Health). After heat-shock transformation, *E. coli* BI21*DE3 cells (Invitrogen) were incubated in 1L of LB media at 37 °C. When the culture reached an OD600 of 0.5-0.7, expression was induced with 1mM IPTG. After growing at 37 °C for 4 h the cells were harvested and then resuspended in lysis buffer (50 mM NaCl, 20 mM NaH_2PO_4, pH 7.5, 5 mM EDTA). For K19C and T11C K19C GB3 50 mM DTT was added to ensure all thiols were reduced. The resuspended cells were sonicated (Branson Sonifier 250) on ice at power level 6. Processed lysate was incubated at 85 °C for 15 min

and was swirled every 3-4 min. After the mixture was cooled on ice, DNA was precipitated by adding 0.5 % streptomycin sulfate and swirling an additional 10 min. The lysate was centrifuged (Beckman Coulter) at 18000 g for 45 min, with GB3 remaining in the soluble fraction. Further DNA removal was performed using anion exchange column (GE Healthcare 5 mL HiTrap Q FF). The collected fractions were loaded onto HiLoad26/600 Superdex 75 pg column (Amerisham biosciences/GE healthcare) and eluted with 50 mM NaCl, 20 mM NaH_2PO_4, pH 7.5 (5 mM DTT for K19C and T11C K19C GB3). Pooled protein fractions were exchanged buffer to nanopure water by performing HiPrep26/10 desalting column (GE healthcare) and frozen at -80 °C. The protein was then lyophilized, and purity was estimated at >98% by SDS-PAGE (Biorad) analysis.

3.3.3 Protein interactions with AgNPs

As-received colloidal AgNPs (7.8 nM, 0.5 mL) were mixed with $GB3_0$ protein (30 μM, 0.5 mL) and time-resolved UV-vis spectra were acquired immediately after the mixing. The same procedure was followed for $GB3_1$, $GB3_2$ and BSA proteins. Concentration dependence of protein interaction with AgNPs was studied by using 1, 10, 30, and 90 μM protein solutions. The time-resolved UV-vis spectra were taken immediately after the protein and AgNP mixing. The time-dependent UV-vis spectra were taken periodically during the entire time-course (up to 3 weeks) of the experiment period.

3.3.4 Effect of Ag^+ on protein interactions with AgNPs

A 0.5 mL aliquot of 600 μM $AgNO_3$ was mixed with an equal volume of each protein (60 μM), and then the solutions were refrigerated overnight to allow protein binding with Ag^+. The $AgNO_3$-treated proteins were then mixed with an equal volume of as-received AgNPs. Time-resolved UV-vis spectra were acquired immediately after AgNP addition.

3.3.5 Sequential protein and organothiol interactions with AgNPs

A 400 μL sample of as-received colloidal AgNPs was mixed with an equal volume of a 30 μM solution of each protein, respectively. The solutions were incubated overnight before the addition of 400 μL of 900 μM organothiol. Time-dependent UV-vis spectra were acquired immediately after the organothiol addition.

3.3.6 Transmission electron microscopy (TEM) measurement

TEM measurement was acquired using a JEOL 2100 instrument. The washed AgNP samples were deposited onto Cu grids covered with a Formvar carbon film. The measurements were conducted at an accelerating voltage of 200 kV.

3.3.7 Raman and SERS measurements

All Raman and SERS spectra were acquired with an Olympus 10 x objective, a spectrograph grating of 300 grooves/mm, and a laser intensity before entering the sample of 1.3 mW. The spectral integration time varied from 10 to 200 s. The Raman shift was calibrated with a neon lamp, and the Raman shift accuracy was ~ 0.5 cm^{-1}. When it was needed, 100 μL of 5% KCl was used as the aggregation reagent to induce AgNP aggregation before the SERS acquisition.

3.4 Results and discussion

3.4.1 Protein interactions with AgNPs

The effects of cysteine on the protein interactions with AgNPs were studied with time-resolved UV-vis spectroscopic method, which monitored the protein-adsorption-induced change in the AgNP localized surface plasmonic resonance (LSPR) (Figure 3.3). Upon protein addition, the AgNP LSPR peak absorbance increases immediately (within the first two seconds, the instrument dead time for time-resolved UV-vis). After reaching a maximum absorbance within the first few seconds, however, the AgNP LSPR peak absorbance monotonically decreases upon prolonged sample incubation for AgNPs treated with $GB3_1$, $GB3_2$, and BSA, while the LSPR peak of the $GB3_0$ treated AgNP is totally stable after the initial LSPR intensity change.

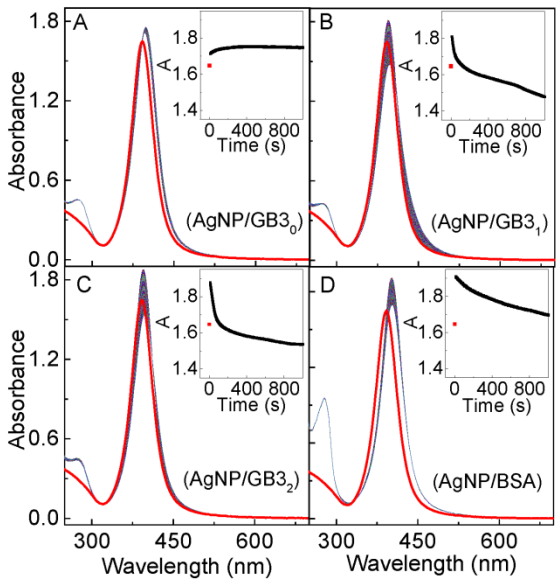

Figure 3.3 Time-resolved UV-vis spectra of (A) AgNP/$GB3_0$, (B) AgNP/$GB3_1$, (C) AgNP/$GB3_2$, and (D) AgNP/BSA.

Note: The spectrum in red is the AgNP control. Insets are the time course of the peak AgNP UV-vis absorbance as a function of sample incubation time. The nominal concentrations of AgNPs and proteins are 3.9 nM and 15 μM, respectively.

It is instructive to compare the AgNP versus AuNP LSPR changes induced by protein adsorption. Immediate nanoparticle LSPR increase was also observed when the same sets of model proteins were added into AuNPs.[43,53] This result indicates that protein adsorption onto AuNPs and AgNPs are both extremely rapid processes, and the protein cysteine content has no appreciable effect on either protein/AuNP or protein/AgNP binding kinetics. However, unlike the AuNPs for which their LSPR time-courses induced by GB3 protein binding are approximately identical for all three GB3 protein variants[43], the LSPR time-courses of the GB3 treated AgNPs are much more complicated (Figure 3.3). The increments in the AgNP LSPR peak absorbance induced by GB3 proteins increase from 0.11 for $GB3_0$, to 0.17 and 0.23 for $GB3_1$ and $GB3_2$, respectively. However, the LSPR peak absorbance of the AgNPs treated with $GB3_0$ remains constant after its initial increase, but the AgNP LSPR peak absorbance decreases significantly in the AgNP/$GB3_1$ and AgNP/$GB3_2$ from their respective maximum peak absorbance.

The increase of the AgNP LSPR peak absorbance is due to the protein binding to the AgNP surfaces, which increases the dielectric constant of the medium immediately surrounding the AgNP surfaces. However, the subsequent decrease of the AgNP LSPR peak absorbance is due to the protein-induced AgNP dissolution. The fact that $GB3_0$ induces no significant AgNP dissolution indicates that except for cysteine, the other 15 different amino acid residues in the GB3 proteins have no significant effect on AgNP dissolution. The fact that BSA induces significantly less AgNP LSPR attenuation than that for both $GB3_1$ and $GB3_2$ strongly indicates disulfide-linked cysteine is not effective in inducing AgNP dissolution. The latter was experimentally confirmed later in this chapter.

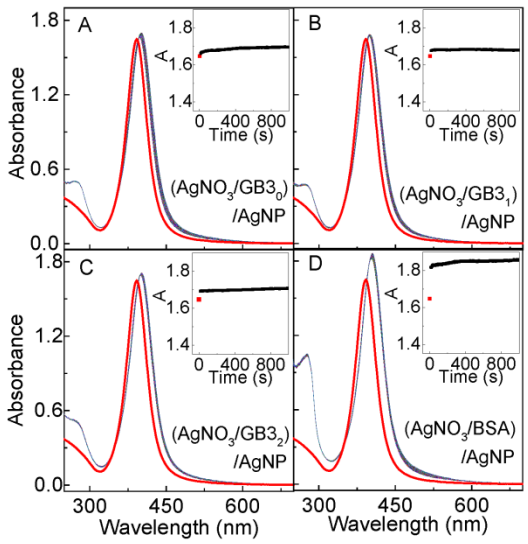

Figure 3.4 AgNP interactions with $AgNO_3$-treated proteins. Time-resolved UV-vis spectra of AgNPs mixed with $AgNO_3$ treated (A) $GB3_0$, (B) $GB3_1$, (C) $GB3_2$, and (D) BSA, respectively.

Note: Insets are the time course of the AgNP peak UV-vis absorbance. The concentration of $GB3_0$, $GB3_1$, $GB3_2$ and BSA proteins are 60 μM. Ag^+/protein ratio was 10/1. $AgNO_3$ and protein were mixed and incubated overnight. Time-resolved UV-vis spectra were obtained immediately after the addition of AgNPs to the $AgNO_3$-treated proteins.

Experimental confirmation that protein-induced AgNP dissolution is caused by protein chelating Ag^+ comes from the study of AgNP binding with proteins pretreated with excess $AgNO_3$ (Figure 3.4). In this case, the AgNP LSPR peak absorbance increased immediately after the addition of the $AgNO_3$-treated protein. This is similar to what has been observed with AgNP mixed with intact proteins. However, subsequent aging of (protein/$AgNO_3$)/AgNP solutions has no significant effect on the the AgNP LSPR absorbance. It is important to note that the ratio of the Ag^+/protein in these (protein/$AgNO_3$)/AgNP samples are 10/1. The amount of Ag^+ is in large excess to saturate all the reduced protein cysteine residues for all GB3 proteins and in BSA, but is

not adequate for the 34 oxidized (disulfide-linked) protein cysteine residues in BSA. This design allows us to differentiate the effectiveness of oxidized and reduced protein cysteine residues in inducing AgNP dissolution. The data in Figure 3.4 have two notable implications. First, Ag^+ chelated proteins can also rapidly adsorb onto the AgNP surface, which provides further evidence that the protein/AgNP binding is initiated by nonspecific forces. Second, oxidized (disulfide-linked) protein cysteine residues have no significant effect in inducing AgNP dissolution. Otherwise, there should be a significant AgNP LSPR decrease in the (BSA/$AgNO_3$)/AgNP sample. The fact that no significant AgNP LSPR decrease is observed in the (protein/$AgNO_3$)/AgNP samples also indicate that besides cysteine, other protein amino acid residues cannot induce significant AgNP dissolution. Otherwise, one should also observe significant AgNP dissolution at least in (BSA/$AgNO_3$)/AgNP, considering that each BSA molecules contains 583 amino acids.

Figure 3.5 illustrates the protein concentration dependence of the protein/AgNP interactions. When protein concentration is low, the AgNP LSPR peak increases instantaneously following addition of protein. Further aging the protein/AgNP mixtures has no effect on the AgNP LSPR feature. This is true regardless of the proteins used. However, once the protein concentrations surpass the saturation packing density of the proteins, AgNP/$GB3_1$ and AgNP/$GB3_2$ mixtures exhibit significant protein concentration dependence in the degree of the protein-induced AgNP dissolution. (Saturation packing concentration for each protein was estimated on the basis of the AgNP size, concentrations of AgNPs, and the size of the proteins. AgNP diameter was assumed to be exactly 10 nm. The concentration of AgNPs was 7.8 nM. Literature reported footprints of GB3 and BSA proteins were 4 and 25 nm^2, respectively.[53,123] The calculated saturation

packing concentrations of proteins were ~0.6 and ~0.1 μM for GB3 and BSA proteins, respectively). In contrast, the degree of the BSA induced AgNP dissolution within the probed time period is independent of the BSA concentration. The fact that no $GB3_0$ induced AgNP dissolution occurs regardless of the protein concentration further confirms that only cysteine residues in the GB3 proteins can induce significant AgNP dissolution.

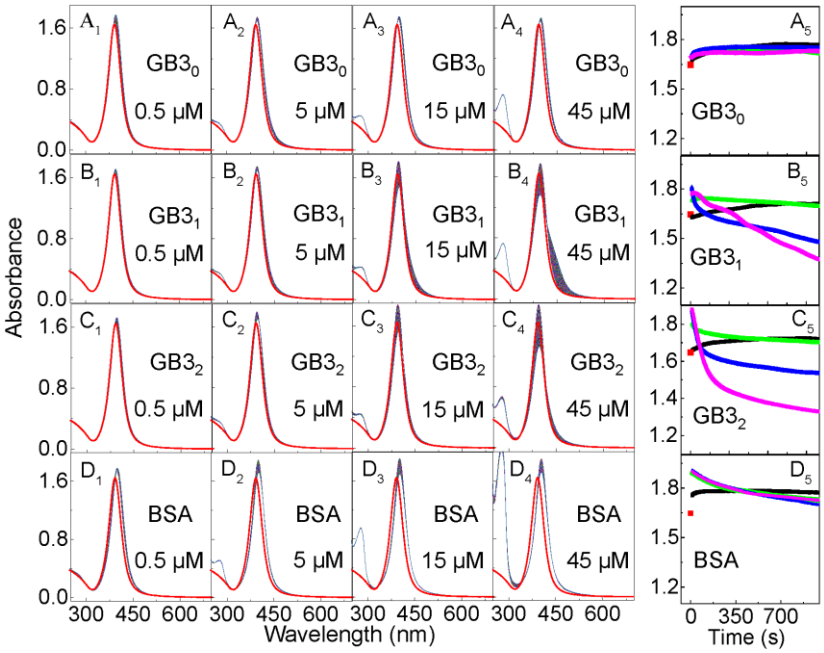

Figure 3.5 Concentration dependence of protein interaction with AgNPs. Time–resolved UV-vis spectra of (A_{1-4}) (AgNP/$GB3_0$), (B_{1-4}) (AgNP/$GB3_1$), (C_{1-4}) (AgNP/$GB3_2$), and (D_{1-4}) (AgNP/BSA) as a function of protein concentration. The time course of the peak AgNP UV-vis absorbance of (A_5) (AgNP/$GB3_0$), (B_5) (AgNP/$GB3_1$), (C_5) (AgNP/$GB3_2$), and (D_5) (AgNP/BSA) mixtures as a function of sample incubation time.

Note:The spectrum in red is the AgNP control. The nominal protein concentrations in 1-4 are 0.5, 5, 15, and 45 μM, respectively. In A_5-D_5 0.5, 5, 15, and 45 μM protein solutions are represented in black, green, blue, and magenta, respectively.

Three possible pathways can be proposed to explain the protein concentration dependence of protein-induced AgNP dissolution (Figure 3.6). The first is protein

dissociative exchange on the AgNPs in which the protein initially is adsorbed onto the AgNPs, chelates with the surface silver ion, and then is dissociatively exchanged with free protein in solution. AgNP dissolution proceeds until all the reduced cysteine residues in the proteins are saturated with Ag^+. The second pathway involves protein displacement exchange in which the incoming protein displaces the Ag^+-loaded protein on the AgNP surfaces. The third pathway involves Ag^+ leakage where the oxidized Ag^+ or silver oxide diffuses through the protein overlayer into the surrounding medium, and reacts with protein free in solution. All three pathways could be concurrently in play in all protein/AgNP mixture solutions. However, the likely main reaction pathway for $GB3_1$ and $GB3_2$ induced AgNP dissolution is through the protein displacement exchange (pathway B in Figure 3.6) in which the rate of the AgNP dissolution depends critically on the protein concentration. In contrast, the BSA-induced AgNP dissolution likely follows the dissociative protein exchange and/or silver leakage pathway where the rate of protein-induced AgNP dissolution is mostly independent of protein concentration (pathways A and C in Figure 3.6). It is known that the rate of displacement exchange critically depends on the concentration of the incoming ligands,[124,125] but the kinetics of the dissociative exchange depends on the amount of the protein adsorbed onto the AgNP surfaces. The silver leakage pathway is a two-step process. The surface silver atom is first oxidized and detached from the AgNP surface, and then diffuses through the protein overlayer. Subsequently, the diffuse silver ion chelates with a protein cysteine residue, leading to further AgNP oxidation and dissolution. The rate limiting step in this silver leakage pathway should be the AgNP oxidation and silver ion diffusion, but not by the Ag^+ ion chelating with the protein cysteine residue.

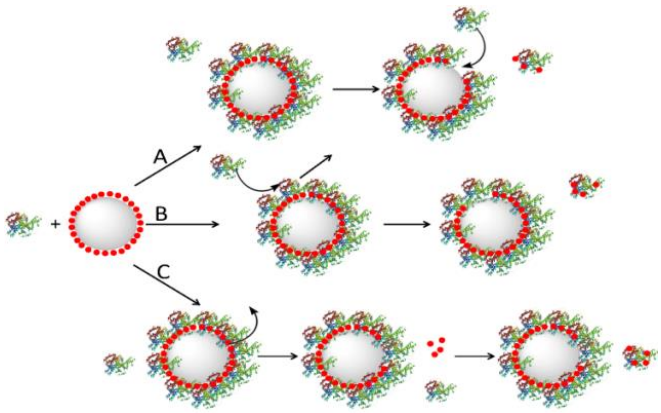

Figure 3.6 Schematics of possible pathways for protein-induced AgNP dissolution. (A) Dissociative exchange, (B) displacement exchange, and (C) silver ion leakage.

Note: (A) Dissociative protein exchange in which the dissociated protein carries the dissolved silver atoms, (B) displacement protein exchange in which the displaced protein carries the dissolved silver atoms, and (C) silver ion leakage in which surface silver is oxidized and diffused out of the protein overlayer. Large gray spheres and small red spheres represent AgNPs and Ag^{+} ions, respectively.

The protein concentration dependence of the AgNP LSPR feature is in sharp contrast to the AuNP LSPR feature induced by protein binding (Figure 3.7). The AuNP LSPR peak absorbance reaches a constant once the protein concentration is beyond a threshold value in the AuNP/protein mixtures. Further addition of protein has no effect on the AuNP LSPR features. This result indicates that protein can only adopt a monolayer adsorption onto AuNPs. It also highlights the difference between AgNPs and AuNPs in their molecular-level interfacial interactions.

The reason that the AgNP dissolution rate induced by BSA is lower than same amount of $GB3_1$ and $GB3_2$ (Figure 3.5) is likely due to the former's much larger size. The molecular weight of BSA is about 10 times higher than that of GB3 proteins. Accordingly, the rates of protein/protein exchange on AgNP surface, protein dissociation

from the AgNP, and the silver leakage from the AgNP surface in AgNP/BSA mixtures should be drastically slower than their respective counterpart process in the AgNP/GB3 protein mixtures.

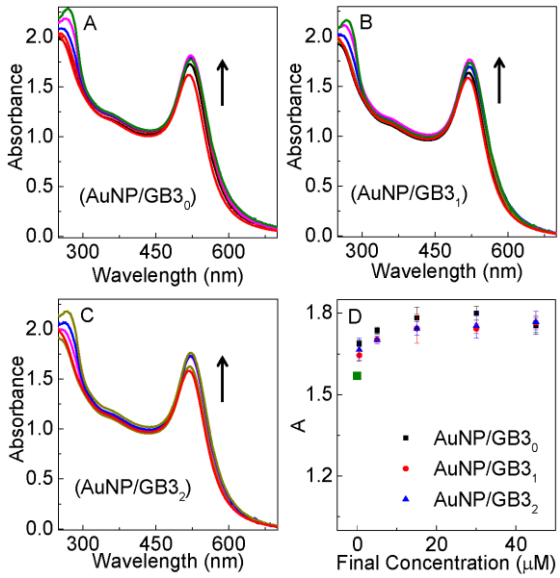

Figure 3.7 Concentration dependence of protein interactions with AuNPs. UV-vis spectra of (A) (AuNP/GB3$_0$), (B) (AuNP/GB3$_1$), (C) (AuNP/GB3$_2$), and (D) correlation between the peak UV-vis absorbance of (AuNP/GB3$_0$), (AuNP/GB3$_1$), and (AuNP/GB3$_2$) mixtures with protein concentration.

Note: The nominal concentration of AuNPs is 11.7 nM. Protein concentrations are 0.5, 15, 30, and 45 μM, respectively. The concentration dependence of AuNPs with BSA protein has been reported in our previous publication.[53]

3.4.2 Sequential protein and organothiol interactions with AgNPs

The sequential protein and organothiol interactions with AgNPs are enormously complicated (Figure 3.8). AgNPs mixed with the GB3 proteins and BSA maintains excellent dispersion stability (no aggregation) in water (Figure 3.3). However, organothiols can induce both significant AgNP dissolution and AgNP aggregation (Figures 3.8, parts A$_1$ -A$_3$). It is critical to note that AgNP dissolution and aggregation is

not mutually exclusive even though AgNP aggregation should invariably reduce the rate of AgNP dissolution. The AgNP dissolution rate in the AgNP/organothiol mixture should also increase with increasing water solubility of the silver-thiolate salts. After prolonged (~3 weeks) sample incubation, no AgNPs can be observed in the AgNPs mixed with excess Cys (Figure 3.8). The AgNPs were converted into amorphous white precipitates that can be seen under microscopy examinations (Figure 3.9). In contrast, the AgNP dissolution rate in AgNP/Hcy and AgNP/Prt are much slower. The precipitate in the AgNP/Prt mixture is mostly the aggregated AgNPs, the amorphous silver-propylthiolate salt can only be observed in the TEM image of the prolonged incubated AgNP/Prt mixture (Figure 3.10), but not in the optical image shown in Figure 3.9.

All the model proteins including $GB3_0$ show organothiol-induced AgNP aggregation in the (AgNP/protein)/organothiol samples, and BSA is the most effective protein in preventing AgNP aggregation triggered by the subsequently added organothiols. However, none of the proteins can prevent AgNP dissolution induced by the subsequently added organothiols, which is evident from the complete absence of AgNPs in the (AgNP/protein)/Cys sample and from the large AgNP LSPR intensity drop in the (AgNP/protein)/Hcy samples. Importantly, the effect of the protein binding to AgNP on AgNP dissolution induced by the subsequently added organothiol is likely highly complicated. On one hand, the protein enhances the AgNP dispersion stability in solution, which should enhance organothiol-induced AgNP dissolution. On the other hand, the protein overlayer on the AgNP should reduce the mass transfer rate of the organothiol in and out of the protein overlayer, which can reduce the rate of AgNP dissolution. Consequently, the dissolution rate of AgNPs sequentially treated with

protein/organothiol mixture can be slower or faster than AgNPs mixed with organothiol alone depending on the structure and conformation of protein and organothiol on the AgNPs, and the solubility of the silver-thiolate salt.

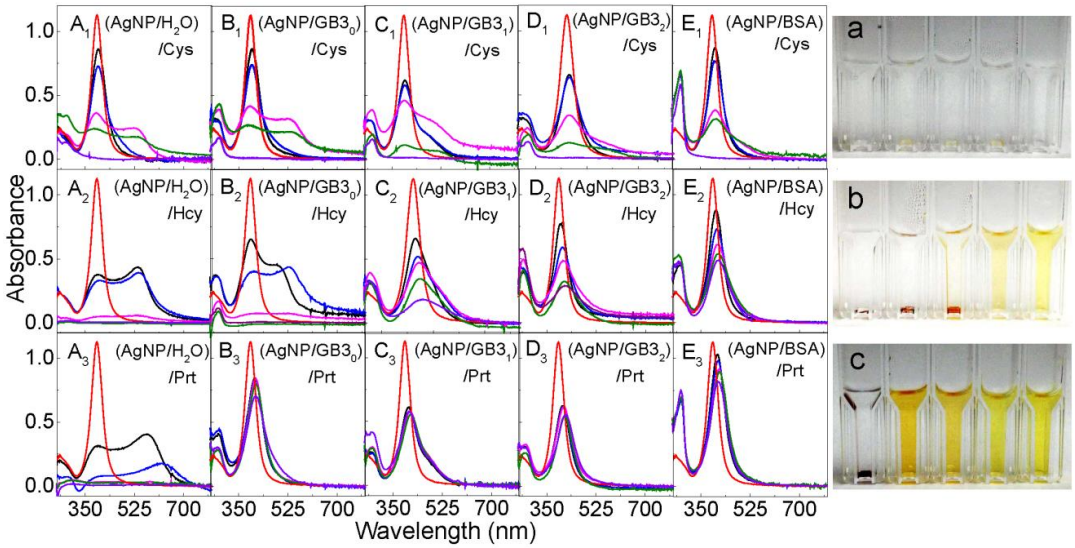

Figure 3.8 Sequential protein and organothiol interaction with AgNPs. (Left) Time-dependent UV-vis spectra of (A_1-A_3) (AgNP/H_2O)/organothiol, (B_1-B_3) (AgNP/$GB3_0$)/organothiol, (C_1-C_3) (AgNP/$GB3_1$)/organothiol, (D_1-D_3) (AgNP/$GB3_2$)/organothiol, and (E_1-E_3) (AgNP/BSA)/organothiol. (Right) Photographs of the AgNPs treated with Cys, Hcy, and Prt, respectively.

Note: Spectra were obtained (red) 0 min, and (black) 2 min, (blue) 1 h, (magenta) 1day, (green) 3 days, and (purple) 3 weeks after the sample preparation. The concentrations of AgNP, protein, and organothiols were 2.6 nM, 10 µM, and 300 µM, respectively. Cuvettes in photograph form left to right corresponding to samples A to E in the same row. Photographs were taken after the samples were left in refrigerator for three weeks.

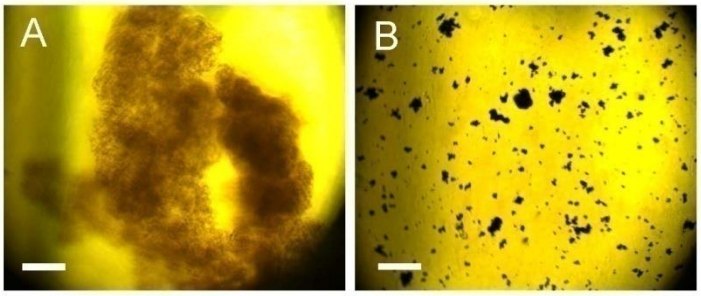

Figure 3.9 Optical images of the precipitate formed in 3 weeks aged (A) AgNP/Cys and (B) AgNP/Prt. Scale bar = 100 μm.

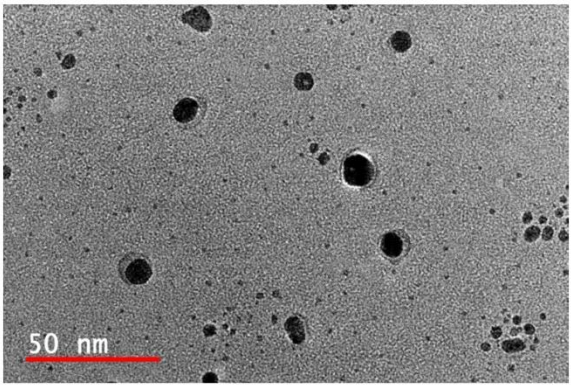

Figure 3.10 TEM image of (AgNP/Prt) mixture after prolonged incubation.

Note: The scale bar is 50 nm. The sample preparation and TEM measurement procedure are described in the experimental section.

All three pathways proposed in Figure 3.6 for the protein concentration dependence of protein-induced AgNP dissolution could be in play for the sequential protein and organothiol interactions with AgNPs. Besides possible silver ion leakage, the dissociative and displacement exchanges between protein/protein, organothiol/organothiol, and protein/organothiol can also contribute to the AgNP dissolution. Presumably, the organothiol/organothiol exchange is likely the predominant pathway for the AgNP dissolution in the (AgNP/protein)/organothiol mixtures. This

hypothesis is consistent with the fact that Cys introduces significantly faster AgNP dissolution than Hcy and Prt in their corresponding (AgNP/protein)/organothiol mixture solutions (Figure 3.8).

3.4.3 Cyt binding with AgNPs

Oxidized (disulfide-linked) cysteines play critical roles in protein structure and properties. Most cysteine residues in wild-type proteins are disulfide-linked to maintain the globular structure of the proteins. Possible AgNP interaction with oxidized protein cysteine residues has been studied with Cyt as the model molecule. However, Cyt differs significantly from the oxidized protein cysteine residues because the latter do not usually contain free carboxylate groups. In contrast, each Cyt has two free carboxylate groups for possible AgNP binding. Indeed, Lee et al. believed that Cyt binds to the AgNPs as a thiolate in which the S-S bond is cleaved by the formation of S-Ag bonds,[122] while Lopez-Tobar et al. proposed that Cyt is adsorbed onto AgNPs as carboxylate.[117] Resolving this controversy is critical for understanding AgNP interactions with oxidized protein cysteine residues. It would be impossible for disulfide-linked cysteine residues in protein to induce any significant AgNP dissolution if Cyt indeed can only bind to AgNP as carboxylate. This is because the carboxyl group in cysteine is mostly utilized in peptide bonds. Furthermore, the absence of significant AgNP dissolution in the $GB3_0$ containing samples regardless of the $GB3_0$ concentrations strongly suggests that the protein carboxyl groups are inadequate for inducing significant AgNPs dissolution under the investigated experimental conditions.

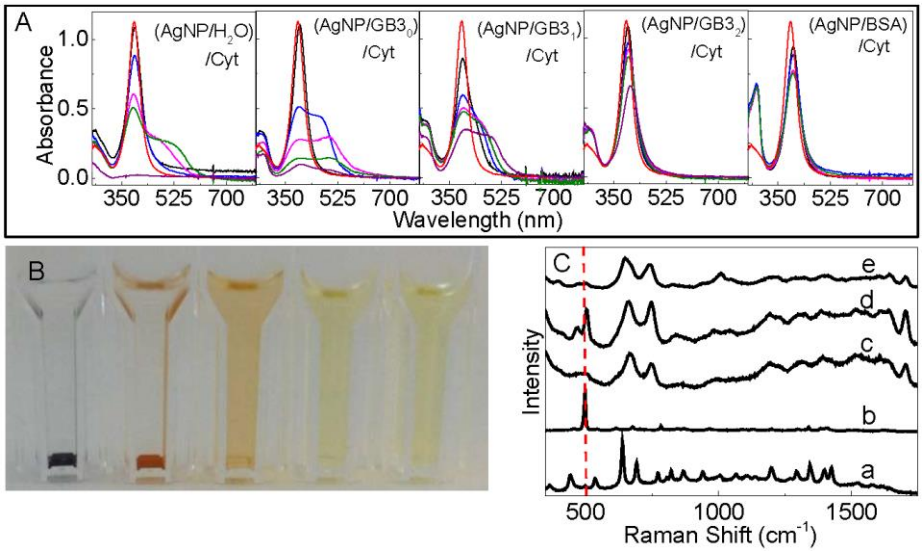

Figure 3.11 Characterization of Cyt interactions with AgNPs. (A) Time-dependent UV-vis spectra of AgNP/Cyt and (AgNP/protein)/Cyt samples and (B) photograph of the AgNP/Cyt and (AgNP/protein)/Cyt samples used for the UV-vis measurement in (A). (C) Time-dependent SERS spectra of Cyt adsorbed onto AgNPs.

Note: The photograph was taken after the samples were kept inside the refrigerator for three weeks. Spectra (a) and (b) in time-dependent SERS spectra in (C) are the normal Raman spectra of Cys and Cyt, respectively, (c) SERS spectra of Cys on AgNPs, and spectra (d) and (e) were acquired with Cyt adsorbed onto AgNPs. The sample incubation time before the SERS spectral acquisition is ~2 h and ~12 h for spectrum (d) and (e), respectively. The dash line indicates the S-S stretch feature at 520 cm^{-1} region.

Figure 3.11 showed the photographs and UV-vis spectra of AgNP/Cyt and (AgNP/protein)/Cyt mixtures, and the SERS spectra of the Cys and Cyt on AgNPs. Cyt induces gradual AgNP aggregation and settlement in the AgNP/Cyt and $(AgNP/GB3_0)$/Cyt and $(AgNP/GB3_1)$/Cyt mixtures, but no significant AgNP aggregation was observed in $(AgNP/GB3_2)$/Cyt and (AgNP/BSA)/Cyt mixtures. In stark contrast to Cys binding to AgNPs that leads to complete AgNP dissolution in all Cys-containing samples, there are still undissolved AgNPs in all the Cyt-containing AgNP samples even

after 2 months of sample incubations. It is important to note that the amount of Cys and Cyt added into the AgNP/protein mixtures are all the same in their sulfur content. The fact that Cyt can induce AgNP aggregation or dissolution confirms that Cyt can bind to AgNPs as previously reported. However, the sharp difference in AgNP dissolution rates between the Cys- and Cyt-containing samples indicates that Cyt is much less effective than Cys for inducing AgNP dissolution.

Time-dependent SERS studies revealed that the Cyt disulfide bond remains mostly intact in Cyt initially adsorbed onto AgNPs, but is cleaved after prolonged sample incubation (Figure 3.11). This is evident from the presence of the S-S stretch feature in the SERS spectra of the freshly prepared Cyt/AgNP sample and absence of the S-S peak in the aged sample. This aging effect on the Cyt structure on AgNPs may be due to both kinetic and thermodynamic reasons. It is possible that the thiolate formation with AgNPs is thermodynamically more favorable, but kinetically slower than the reaction of the carboxylate group with AgNPs. Therefore, the Cyt initially binds as a Ag-carboxylate salt, but is subsequently converted to the more stable Ag-thiolate salt. It is also possible that the disulfide binding to AgNP is both kinetically and thermodynamically more unfavorable than that for carboxylate. In the latter case, the S-S cleavage only occurs when the carboxyl groups in Cyt are fully reacted with silver ions derived from AgNPs.

The fact that Cyt can induce AgNP dissolution in (AgNP/$GB3_2$)/Cyt and (AgNP/BSA)/Cyt does not necessarily imply that oxidized cysteine residues in protein can induce AgNP dissolution. This is because oxidized protein cysteine residues are commonly located in the interior core of globular proteins.[126] Unlike the Cyt in (AgNP/$GB3_2$)/Cyt and (AgNP/BSA)/Cyt that can diffuse to the AgNP surfaces to initiate

the Cyt/AgNP interactions, it is unlikely for the oxidized protein cysteine residues to directly bind to AgNPs. This steric hindrance combined with the low disulfide reactivity with AgNPs explains why BSA is drastically less effective than the thiol-containing GB3 variant in inducing AgNP dissolution. Indeed, the experimental data obtained from AgNP binding with protein pretreated with $AgNO_3$ (Figure 3.4) strongly indicates that oxidized protein cysteine has no effect on protein induced AgNP dissolution.

3.5 Conclusions

The effects of both reduced and oxidized protein cysteine residues on protein binding to AgNPs were investigated with a series of model protein and organosulfur molecules. The protein cysteine content has no effect on the kinetics of protein/AgNP binding. Only reduced protein cysteine induces significant AgNP dissolution when the protein concentration is high. Other protein amino-acid residues including oxidized protein cysteine residues have no significant effect on AgNP dissolution. Pretreatment of AgNPs with protein can inhibit AgNP aggregation induced by subsequently added organothiols, but can not prevent the organothiol-induced AgNP dissolution. The insights provided in this work are important for enhancing the understanding of AgNP interfacial interactions with proteins and organothiols.

Notes: This work has been previously published: Siriwardana, K.; Wang, A.; Gadogbe, M.; Collier, W. E.; Fitzkee, N. C.; Zhang, D., Studying the Effects of Cysteine Residues on Protein Interactions with Silver Nanoparticles. *J. Phys. Chem. C* **2015**, *119*, 2910-2916.

CHAPTER IV

CONTRADICTORY DUAL EFFECTS: ORGANOTHIOLS CAN INDUCE BOTH SILVER NANOPARTICLE DISINTEGRATION AND FORMATION UNDER AMBIENT CONDITIONS

(Published in *J. Phys. Chem. C* **2015,** *119*, 20975-20984)

4.1 Abstract

Using propanethiol (Prt), 2-mercaptoethanol (ME), glutathione (GSH), and cysteine (Cys) as model thiols, we demonstrated herein that organothiols can induce both silver nanoparticle (AgNP) disintegration and formation under ambient conditions by simply mixing organothiols with AgNPs and $AgNO_3$, respectively. Mechanistically, organothiols induce AgNP disintegration by chelating silver ions produced by ambient oxygen oxidizing the AgNPs, while AgNP formation in $AgNO_3$/organothiol mixtures is the result of organothiols serving as the reducing agent. Furthermore, surface plasmon- and fluorescent-active AgNPs can be interconverted by adding excess Ag^+ or ME into the AgNP-containing solutions. Organothiols can also reduce gold ion in $HAuCl_4$/organothiol solutions into fluorescence- and surface plasmon-active gold nanoparticles (AuNPs), but no AuNP disintegration occurs in the AuNP/organothiol solutions. This work highlights the extraordinary complexity of organothiol interactions with gold and silver nanoparticles. The insights from this work will be important for AgNP and AuNP synthesis and applications.

4.2 Introduction

Silver-based nanomaterials are the most commonly used noble metal nanoparticles because of their relatively low cost and many unique physicochemical and antimicrobial properties. There are many types of man-made and naturally occurring silver-based nanomaterials including fluorescent-active silver nanoclusters (AgNC) and surface plasmonic resonance (SPR) active silver nanoparticles (AgNPs)[127-130] that have been used for biosensing,[5,6] chemical catalysis,[7] and solar energy harvesting.[8] Organothiols and thiol-containing biomolecules have been utilized in a wide range of AgNP synthesis and applications.[36,40,131,132] They are the most popular capping agents in AgNC synthesis,[36,130,133-135] and the commonly used model molecules in studying AgNP SERS activities.[71,109,117,136] However, current understanding of organothiol interactions with AgNPs and silver ions remains incomplete. As strong chelating agents of silver ion, organothiols and thiol-containing biomolecules can greatly reduce the redox potential of silver, making AgNPs susceptible to oxidative disintegration under ambient conditions.[36] Using the formation constant of 7.9×10^{11} M^{-1} reported for the complex formed by cysteine and Ag^{+},[137] it was estimated that the redox potential of Ag in 10 mM cysteine is 0.21 V, which is significantly lower than the standard redox potential of oxygen (0.440 V).[138] As a result, aqueous AgNPs are highly susceptible to oxidative disintegration in organothiol-containing solutions under ambient conditions. However, the extent of AgNP disintegration depends critically on the structure and conformation of the organothiols on the AgNP surfaces. For example, aromatic organothiols induce rapid AgNP disintegration, but AgNPs mixed with long-chain alkylthiols are relatively stable in

water.[40,109] The latter is because long alkylthiols are highly ordered on the AgNPs,[109] imposing significant steric hindrance for the silver oxidation reaction.

In theory, organothiols can also stabilize AgNPs. Organothiols are relatively strong reductants in that the S-H can be converted into S-S or higher charge-state sulfur ion. For example, the standard redox potential of glutathione /disulfide-linked glutathione is -0.24V,[139,140] significantly lower than that for Ag^+/Ag. Therefore, organothiols can thermodynamically convert silver ion into AgNPs, inhibiting the AgNP oxidative disintegration under ambient conditions. Indeed, silver ion reduction by thiol has been proposed to explain the observation of reduced silver ion concentration when cysteine was added into $AgClO_4$ solution.[38] An alternative explanation to this observation is that cysteine chelates with Ag^+, forming insoluble cysteine-Ag complex.[141] These two hypotheses differ fundamentally in their reaction pathways. Understanding both the dual functionality and the interplay of organothiols as silver ion reductants and chelating agents are critical for understanding the structures and properties of AgNPs in a sample matrix involving either organothiols or thiol-containing biomolecules.

The goal of this work is to enhance our fundamental understanding of organothiol interactions with AgNPs by studying organothiol interactions with AgNPs and Ag^+ in water. It is noted that organothiol-induced AgNP disintegration has been observed in a series of recent studies.[40,109,141] The disintegration products were generically referred to as silver-thiolate salts. However, the structure and properties of these disintegration products remain essentially unknown. Presented herein is direct experimental evidence of the dual functionality of organothiols as the Ag^+ reductant and chelating agent. Indeed, both

organothiol-induced AgNP disintegration and formation under ambient conditions were observed by simply mixing thiols with AgNPs and $AgNO_3$, respectively.

Glutathione (GSH), cysteine (Cys), 2-mercaptoethanol (ME), and propanethiol (Prt) were used as the model thiols. These molecules differ significantly in their water solubility and structural complexity, therefore allowing us to explore the generality of the experimental phenomena. Cys and GSH were chosen for their biological relevancy and popularity in AgNP-based studies.[5,6,142] The inclusion of Prt and ME is important for pinpointing the effect of the thiol (RS-H) functional group on AgNP and Ag^+ ions because thiol is the only moiety in Prt and ME that can react with silver. The cross-comparison of the structure and properties of reaction products of both AgNP and Ag^+ with this series of thiols provides insights that would be difficult to obtain with individual organothiols. For the sake of simplicity, we use A/B to denote solutions of components A and B.

4.3 Experimental section

4.3.1 Materials and instruments

All chemicals were purchased from Sigma-Aldrich and used as received. Both commercial and in-house synthesized citrate-reduced AgNPs were used. The relatively monodispersed AgNPs with a nominal diameter of 10 nm were purchased from Nanocomposix Inc. The in-house AgNPs were prepared using the Lee-Meisel method.[14] Gold nanoparticles were synthesized using the citrate reduction method.[92] Nanopure water (18.2 MΩ cm) was used in sample preparation. An Olis HP 8452 A diode array spectrophotometer was used for the UV-vis measurements. Fluorescence measurements were acquired using a Horiba Jobin Yvon fluoromax-4 spectrofluorometer. A Spectroline TE-3123 UV-transilluminator (Spectronics Corporation) was used to take fluorescent

images. TEM measurements were acquired using a JEOL 2100 instrument. IR spectra were acquired using Thermo Scientific NICOLET iS5 iD5 ATR-FTIR instrument.

4.3.2 AgNP disintegration in AgNP/organothiol mixture

A 1.4 mL aliquot of as-received commercial AgNPs of 10 nm in diameter were mixed with 0.6 mL of 4.7 mM organothiols in either water or ethanol/water (v:v 50/50) and incubated under ambient conditions. Time-dependent UV-vis and fluorescence spectra were acquired with the AgNP/organothiol mixtures after brief vortexing. The precipitates in these samples were washed extensively with water before further analysis using TEM and XPS.

4.3.3 AgNP formation in $AgNO_3$/organothiol mixture

A 1.4 mL aliquot of 1mM $AgNO_3$ and 0.6 mL of 21 or 0.26 mM organothiols in water or ethanol/water (v:v 50/50) were mixed and incubated under ambient conditions. Washed precipitates in the solutions were analyzed using TEM, XPS, UV-vis, and fluorescence spectrophotometer.

4.3.4 AuNP formation in $HAuCl_4$/organothiol mixture

A 1.4 mL aliquot of 1mM $HAuCl_4$ and 0.6 mL of 21 or 0.26 mM organothiols were mixed and incubated under ambient conditions. Washed precipitates were analyzed using TEM, XPS, UV-vis, and fluorescence spectrophotometer.

4.3.5 X-ray photoelectron spectroscopic (XPS) measurement

XPS measurements were acquired for the precipitates in the AgNP/organothiol and $AgNO_3$/organothiol mixtures that were deposited on the silicon wafers. All samples were washed thoroughly with 18.2 MΩ cm Nanopure water before depositing on the

silicon wafers. The silicon wafers were soaked in an ultrasonic bath in reagent degree isopropanol for 5 min and dried with UNP N_2 gas before the XPS measurements.

XPS analysis was performed using a Thermo Scientific K-Alpha XPS system equipped with a monochromatic X-ray source at 1486.6 eV corresponding to the Al Kα line. The spot size was 400 μm^2 and the takeoff angle of the collected photoelectrons was 90˚ relative to the sample surface. The pass energy for the acquisition of the survey spectra was 200 eV and the pass energy for the high resolution core level spectra was 50 eV. An average of 20 scans was performed for each sample, with a step size of 0.1 eV. All measurements were performed in the Constant Analyzer Energy mode. "Avantage v5.932" software was used in XPS data analysis. C 1s, N 1s, O 1s, S 2p, and Ag 3d signal intensities were determined by fitting their respective peaks with a mixture of Lorentzian and Gaussian curves.

4.3.6 Transmission electron microscopy (TEM) measurement

TEM measurements were acquired using a JEOL 2100 instrument. The washed precipitates from the AgNP/organothiol, $AgNO_3$/organothiol, and $HAuCl_4$/organothiol mixtures were deposited on Cu grids covered with a Formvar carbon film. The measurements were conducted at an accelerating voltage of 200 kV.

4.4 Results and discussion

4.4.1 Thiol-induced AgNP disintegration

ME, Cys, and GSH induced significant AgNP disintegration, but no significant AgNP disintegration was seen in the AgNP/Prt mixture. These conclusions were drawn from the UV-vis and TEM measurements shown in Figure 4.1. Sponge-like precipitates

were observed in the AgNP/GSH, AgNP/Cys, and AgNP/ME mixtures and the color of these precipitates ranged from light yellow in the AgNP/GSH mixture to mostly whitish in AgNP/Cys. However, only black AgNP aggregates were observed in the AgNP/Prt mixture (Figure 4.1). TEM measurements conducted with the washed precipitates revealed that the AgNPs were disintegrated into much smaller particles in the AgNP/GSH, AgNP/Cys and AgNP/ME solutions, but there was no significant size change for AgNPs in the AgNP/Prt solution. UV-vis measurements conducted with the vortex-agitated AgNP/organothiol solutions showed that the AgNP localized surface plasmon resonance peak (LSPR) at 392 nm region disappeared in the AgNP/GSH, AgNP/Cys, and AgNP/ME solutions. This indicates that AgNPs were completely disintegrated in these samples.

There are two reasons for the drastic difference between Prt and the other three model organothiols in inducing AgNP disintegration. First, the solubility of Prt in water is significantly lower than that for the other organothiols, which affects the dispersion stability of the reaction products between AgNPs and organothiols. Indeed, AgNPs aggregated and precipitated much faster in the AgNP/Prt mixture than the reaction products of AgNPs and the other model organothiols. Consequently, the mass transfer for environmental oxygen to trigger the silver oxidation is likely slower in the AgNP/Prt solution than that in AgNPs mixed with other thiols. Second, as an alkanethiol, Prt are highly ordered on the AgNP surface,[109] which further reduced the mass transfer of the AgNP disintegration reactions.

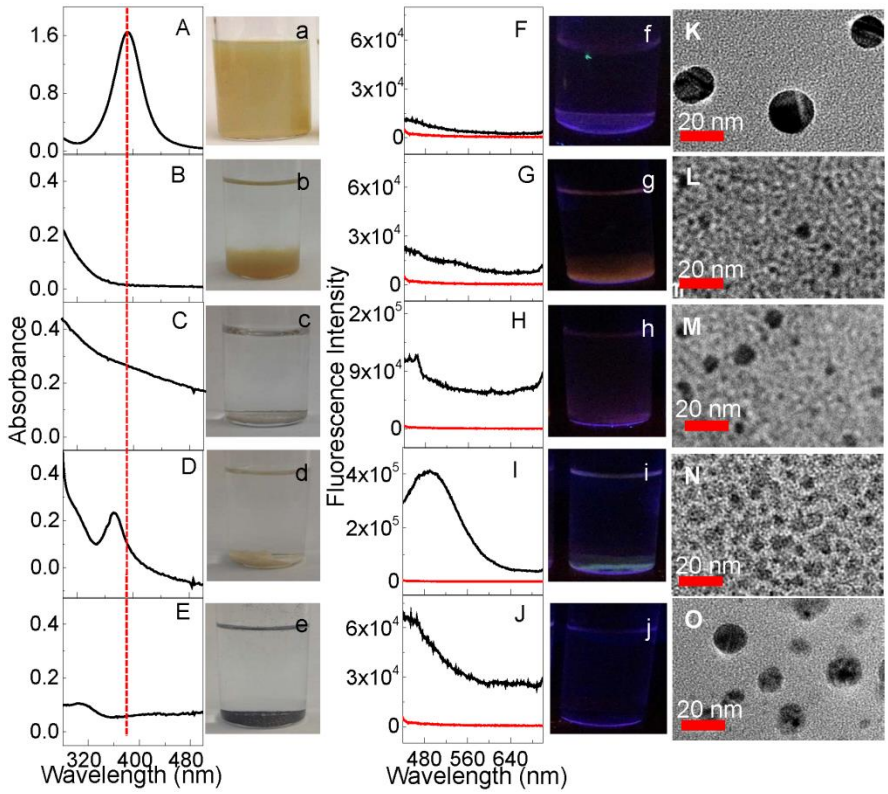

Figure 4.1 Thiol-induced AgNP disintegration conducted with the commercial AgNPs. UV-vis spectra of (A) AgNP control, (B) (AgNP/GSH), (C) (AgNP/Cys), (D) (AgNP/ME), and (AgNP/Prt). Fluorescence spectra of (F) AgNP control, (G) (AgNP/GSH), (H) (AgNP/Cys), (I) (AgNP/ME), and (J) (AgNP/Prt). (K-O) TEM images of AgNPs and washed precipitates in the (AgNP/organothiol) mixtures.

Note:Fluorescence excitation wavelength was 370 nm. UV-vis and fluorescence spectra were obtained 3 days after sample preparation and the solutions were vortex mixed before measurements. Photographs of respective samples were taken under (a-e) room light and (f-j) UV light. The nominal concentrations of AgNPs and organothiols are 3.9 nM and 1.4 mM, respectively. Lower magnification TEM images of these samples were shown in Figure 4.2.

The comparison of the degree of AgNP aggregation induced by Prt with that induced by aromatic monothiols such as methylbenzenethiol (MBT) is revealing. MBT is even more water-insoluble than Prt. However, the degree of MBT induced AgNP disintegration observed in our recent study,[40] is significantly higher than that of Prt. This

result strongly suggests that the key reason for the greater stability of AgNPs in the AgNP/Prt mixture is the Prt ordering on AgNPs, not its poor water solubility. Indeed, the rather general observation that organothiols induce AgNP disintegration contradicts the proposal that organothiols passivate AgNPs from oxidative disintegration.[38] This is because organothiols significantly reduce the silver redox potential, making AgNPs more thermodynamically susceptible to oxidative disintegration by environmental oxygen.

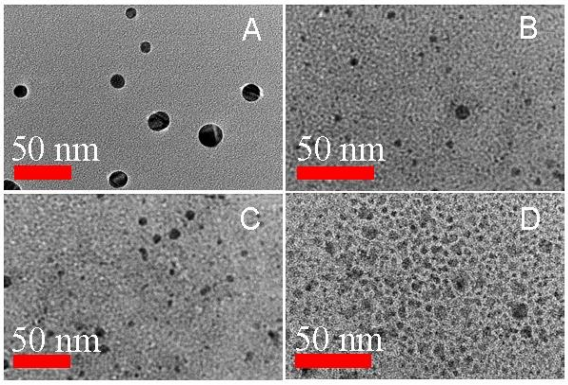

Figure 4.2 TEM images of (A) AgNPs, (B) (AgNP/GSH), (C) (AgNP/Cys), and (D) (AgNP/ME).

Note: The nominal concentrations of 10 nm commercial AgNPs and organothiols are 3.9 nM and 1.4 mM, respectively. The scale bars are 50 nm. Details of sample preparation and TEM data acquisition are shown in the Experimental section.

The UV-vis and fluorescence activities of the disintegrated AgNPs differ significantly among the AgNP/organothiol solutions. Only the AgNP/ME mixture exhibits a well-defined UV-vis peak centered at 370 nm, and relatively high fluorescent activity with a peak emission at ~500 nm. No well-defined UV-vis or fluorescence peaks were observed for other AgNP/organothiol mixtures. Only a low-intensity continuum emission was observed when those samples were excited at 370 nm.

The LSPR-active AgNPs disintegrated in the AgNP/organothiol solutions were eventually converted into smaller AgNPs as the final products, not molecular silver-thiolate salts as previously assumed.[40] TEM measurements (Figure 4.1 and 4.2) obtained with the extensively washed precipitates from the AgNP/ME, AgNP/Cys, and AgNP/GSH solutions showed that there are large numbers of polydispersed NPs in these samples. The sizes of these NPs are significantly smaller than that of the initial AgNPs, but the number of these NPs exceeds that of the starting AgNPs. The latter is especially evident for the NPs in AgNP/ME mixtures.

Mechanistically, the small NPs in the AgNP/ME, AgNP/Cys, and AgNP/GSH solutions can be formed through two pathways. The first is the etching pathway in which the individual AgNPs are gradually etched into small NPs through eq. 4.1 where Ag_x and Ag_{x-n} refers to AgNPs that contains *x* and *x-n* core silver atoms. The second is the decomposition pathway in which the RS-Ag formed in eq. 4.1 is converted into small silver nanoparticles that contain zero-valence silver atoms together with the capping thiolate. One possible decomposition reaction is eq. 4.2 in which the molecular silver-thiolate salts were decomposed into disulfide and a silver nanoparticle capped with thiolate.

— (4.1)

(4.2)

$$2m\,RS{-}H + Ag_x + \frac{m}{2}O_2 \rightarrow n\,RS{-}Ag + mH_2O + (Ag)_{x-n}SR_{2m-n}$$

$$(Ag)_n SR_{n-2m} \rightarrow m\,RS{-}SR + (Ag)_n SR_{n-2m}$$

Both pathways could be in play for the small NPs seen in the AgNP/organothiol mixtures. However, the decomposition pathway (eq. 4.2) is likely the predominant one for the small AgNPs observed in the AgNP/ME mixture. Otherwise, the number of small NPs in this sample should be significantly smaller than that observed in the TEM images. This is because the number of small NPs produced through the etching pathway has to be equal to or smaller than the number of the starting AgNPs. Further experimental evidence supporting the decomposition pathway for NPs observed in the AgNP/ME mixtures is that the optical properties of the AgNP/ME mixture are almost identical to that observed with a $AgNO_3$/ME mixture that will be shown below. The only mechanism for AgNP formation observed in the $AgNO_3$/ME mixture is the decomposition pathway.

4.4.2 Thiol-induced AgNP formation

The data in the preceding section demonstrated organothiol disintegration of the LSPR-active AgNPs into small NPs under ambient conditions. The model thiols can also lead to AgNP formation by simply mixing $AgNO_3$ with the organothiols without exogenous reducing agents (Figures 4.3 and 4.4). The structure and properties of the NPs formed in the $AgNO_3$/organothiol mixtures depend critically on the silver and organothiol concentration ratio. Whitish precipitates are formed in the $AgNO_3$/organothiol mixtures that have concentration ratio of 1:9 (Figure 4.3). All samples exhibited a relatively narrow and well-defined UV-vis peak at 370 nm region. When excited at this wavelength, the dispersed precipitates in the $AgNO_3$/GSH, $AgNO_3$/Cys, and $AgNO_3$/ME mixtures are fluorescence-active with peak emission wavelengths at 536, 456, and 500 nm, respectively. The precipitate in the $AgNO_3$/Prt solution is also fluorescence-active even though it has a rather broad emission instead of a well-defined fluorescence peak.

TEM measurements revealed that the AgNPs in these samples are highly polydispersed, but most of the particles are smaller than 10 nm in diameter.

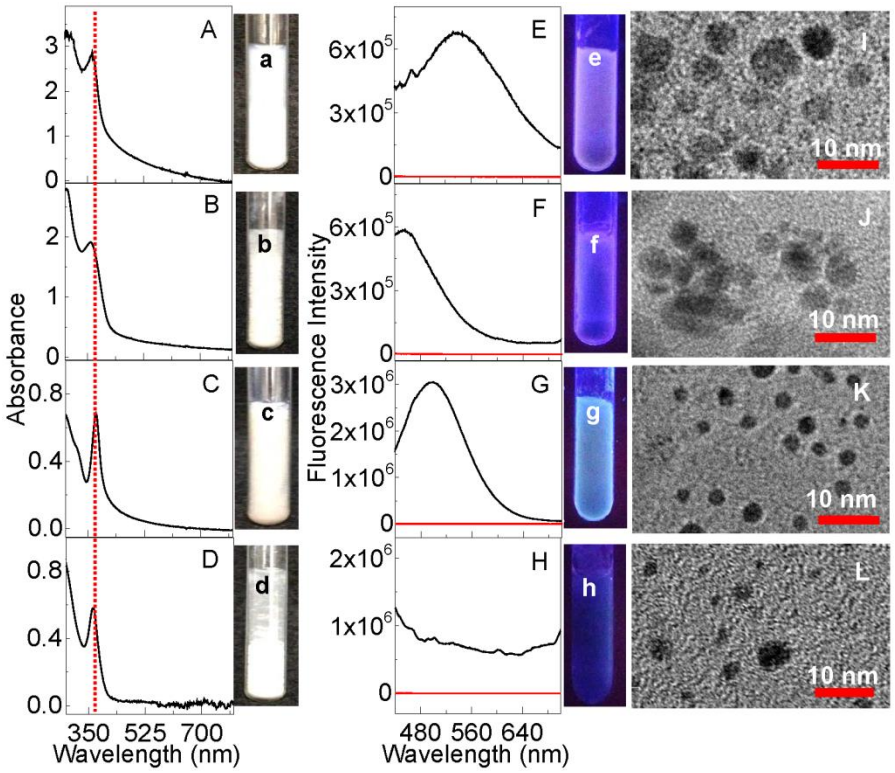

Figure 4.3 Thiol-induced formation of fluorescence-active AgNPs. UV-vis spectra of (A) $AgNO_3$/GSH, (B) $AgNO_3$/Cys, (C) $AgNO_3$/ME, and (D) $AgNO_3$/Prt, respectively. Fluorescence spectra of (E) ($AgNO_3$/GSH), (F) $AgNO_3$/Cys, (G) $AgNO_3$/ME, and (H) $AgNO_3$/Prt, respectively. TEM images of (I) $AgNO_3$/GSH, (J) $AgNO_3$/Cys, (K) $AgNO_3$/ME, and (L) $AgNO_3$/Prt, respectively.

Note: Fluorescence excitation wavelength was 370 nm. UV-vis and fluorescence spectra were obtained 3 days after sample preparation. Photographs of respective samples were taken under (a-d) visible and (e-h) UV light. Molar ratio of $AgNO_3$:organothiol was 1:9 in each mixture. The nominal concentrations of $AgNO_3$ and organothiols are 0.7 and 6.4 mM, respectively.

No fluorescent AgNPs were observed in $AgNO_3$/organothiol mixtures where Ag^+ was in excess. With the only exception of the $AgNO_3$/GSH solution that remained a clear solution during the entire 3 days sample incubation process (Figure 4.5), the other $AgNO_3$/organothiol mixtures turned a yellowish color that is characteristic of LSPR-active AgNPs. Indeed, both the $AgNO_3$/ME and $AgNO_3$/Cys mixtures exhibited a relatively intense and broad UV-vis peak at ~420 nm (Figure 4.4). A much broader peak was observed in the $AgNO_3$/Prt mixture spanning from 350 to 700 nm (Figure 4.4). The latter is due to the presence of aggregated AgNPs, which is consistent with the observation that Prt is much more effective than the other model organothiols for inducing AgNP aggregations. TEM confirms the formation of AgNPs in the $AgNO_3$/ME, $AgNO_3$/Cys, and $AgNO_3$/Prt solutions (Figure 4.4). No significant fluorescence was observed in any of the samples.

The average particle size in precipitates from the $AgNO_3$/ME, $AgNO_3$/Cys, and $AgNO_3$/Prt mixtures that contain excess Ag^+ (Figure 4.4) is significantly larger than that observed in the corresponding $AgNO_3$/organothiol solutions where organothiols are in excess (Figure 4.3). The combined TEM, UV-vis, and fluorescence measurements provided conclusive evidence that organothiols can reduce Ag^+ into both fluorescence- and LSPR-active AgNPs. Unfortunately, the AgNPs are rather polydispersed in both series of samples, and we were unable to separate the AgNPs on the basis of their particle sizes in either case. Attempts to determine the structure of the oxidized organothiol was unsuccessful. The XPS measurements, conducted with the washed precipitates in the AgNP/organothiol and $AgNO_3$/organothiol solutions revealed that sulfur has multiple oxidation states in both series of samples.

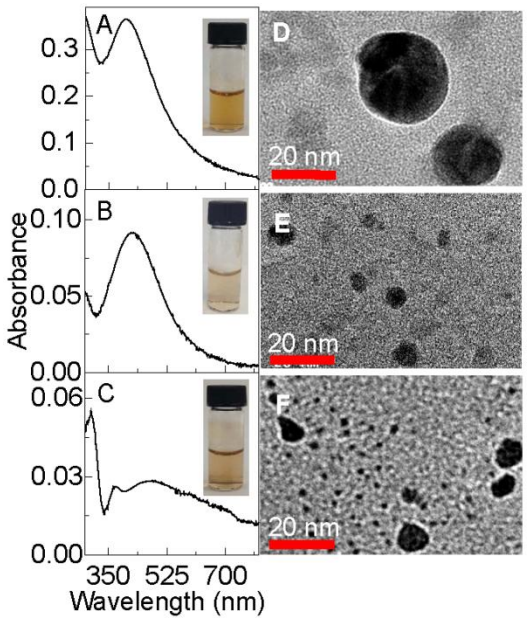

Figure 4.4 Thiol-induced formation of LSPR-active AgNPs. UV-vis spectra of (A) $AgNO_3$/Cys, (B) $AgNO_3$/ME, and (C) $AgNO_3$/Prt, respectively. TEM images of (D) $AgNO_3$/Cys, (E) $AgNO_3$/ME, and (F) $AgNO_3$/Prt, respectively.

Note : Insets: photographs of respective mixtures after NP formation. The molar ratio of $AgNO_3$:organothiol was 9:1 in all mixtures. The nominal concentrations of $AgNO_3$ and organothiols are 700 and 78 µM respectively.

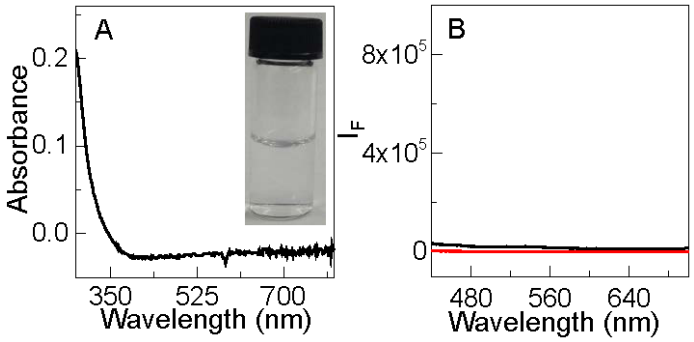

Figure 4.5 (A) UV-vis and (B) fluorescence spectra of (black) $AgNO_3$/GSH mixture and (red) water.

Note: Inset: photograph of mixture after 3 days. $AgNO_3$:GSH molar ratio is 9:1. The nominal concentrations of $AgNO_3$ and GSH are 700 and 78 µM, respectively.

4.4.3 Comparison of the bottom-up and top-down AgNPs

The AgNPs seen in Figure 4.1 in the AgNP/organothiol mixtures can be viewed as the top-down AgNPs, while the AgNPs formed in the $AgNO_3$/organothiol mixtures are the bottom-up AgNPs. It is noted that the concentration ratio of the silver precursor and organothiol used in the AgNP/organothiol mixtures shown in Figure 4.1 is the same as that in their corresponding $AgNO_3$/organothiol mixtures in Figure 4.3. Comparing the structure and properties of the AgNPs in these mixtures should be instructive for determining the reaction mechanisms involved in the bottom-up and top-down approaches.

(4.3)

Except for ME, the structure and properties of the AgNPs observed in the AgNP/organothiol mixtures are markedly different from that observed in their corresponding $AgNO_3$/organothiol solutions. The likely reason for this discrepancy is the difference in the AgNP formation reaction pathways between these two approaches. In the case of the $AgNO_3$/organothiol mixtures, all silver ions likely reacted with organothiols forming RS-Ag intermediates (eq. 4.3) before the AgNP formation reaction (eq. 4.2). The proposed RS-Ag formation reaction (eq. 4.3) is supported by the experimental observation that mixing $AgNO_3$ with organothiols leads to significantly acidified solutions (Table 4.1). Importantly, this pH change occurs immediately (within minutes) following the mixing of the organothiol with $AgNO_3$. Further sample incubation has no significant effect on the solution pH. In contrast, the fluorescent AgNPs only appear at least 30 min after addition of organothiol into the $AgNO_3$ solution. This result supports the hypothesis that the AgNP formation in the $AgNO_3$/ organothiol mixture

$$RS - H + Ag^+ \rightarrow RS - Ag + H^+$$

occurs sequentially with reactions depicted in eq. 4.3 and eq. 4.2, respectively. However, in the case of the AgNP/organothiol solution, the fluorescence-active AgNP formation rates are drastically slower than that in the $AgNO_3$/organothiol solution. One likely reason is that Ag-thiolate salt formation in AgNP/organothiol solution occurs more or less concurrently with the Ag-thiolate conversion to small AgNPs. The kinetics of the Ag-thiolate formation can have significant impact on the structure and properties of the small AgNPs formed in the AgNP/organothiol solutions.

Table 4.1 pH change in the organothiol solutions induced by the $AgNO_3$ and AgNPs.

pH	GSH	Cys	ME	Prt
Before adding $AgNO_3$ or AgNPs	3.1	5.6	5.8	5.6
After adding $AgNO_3$	2.9	2.8	2.6	2.6
After adding AgNPs	3.5	7.5	7.6	7.9

XPS data obtained with the washed precipitates from both $AgNO_3$/ME and AgNP/ME are very similar (Figure 4.6), which is consistent with the fact that the optical properties and morphological features of the AgNPs in these two samples are very similar. In contrast, the XPS data obtained with the precipitates in the AgNP/Cys and AgNP/GSH samples are very different from the precipitate in their respective $AgNO_3$/organothiol mixtures. For example, the fractions of the high-charge state sulfur in the former samples are significantly higher than that in the latter ones (Figure 4.6). While the reason for this discrepancy is unknown, the XPS data confirm that the structures of the small AgNPs in the AgNP/GSH and AgNP/Cys mixtures are indeed different from that in the $AgNO_3$/GSH and $AgNO_3$/Cys solutions, respectively.

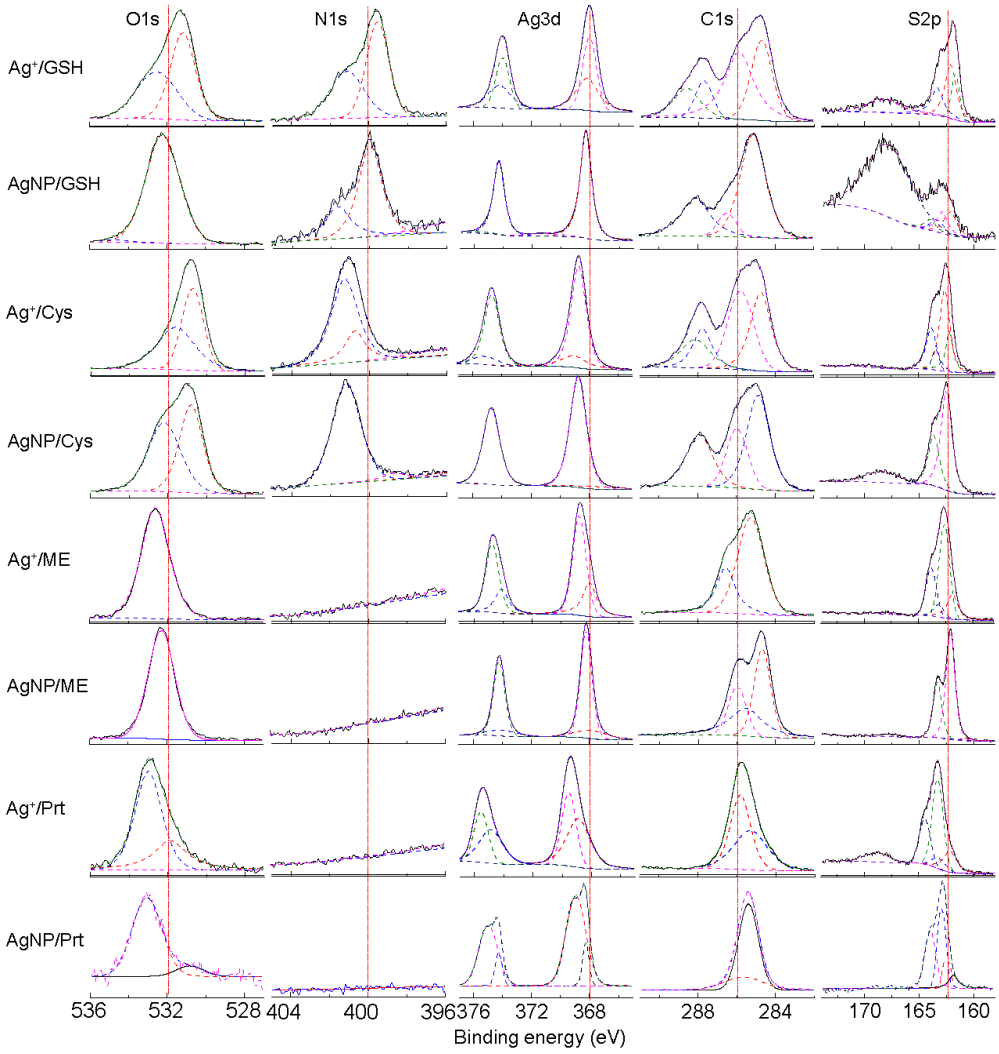

Figure 4.6 XPS spectra of washed precipitates in $AgNO_3$ and AgNPs mixed with GSH, Cys, ME, and Prt, respectively. Spectra from left to right represent XPS spectra for O1s, N1s, Ag3d, C1s, and S2p, respectively.

Note: $AgNO_3$/organothiol and AgNP/organothiol solutions were incubated for 3 days and precipitates were washed before the analysis. Spectra were normalized to the same intensity. The silver and organothiol molar ratio were 1:9 in all samples. Vertical red lines for guiding views.

Table 4.2 XPS analysis of the washed precipitates in AgNP/organothiol and $AgNO_3$/organothiol solutions.[a]

sample	silver			sulfur		
	binding energy (eV)	charge state	percentage %	binding energy (eV)	charge state	percentage %
$AgNO_3$/GSH	367.98 368.18	+1 0	22.93 44.07	161.68 162.08 168.28	-2 -1 +6	29.60 49.08 21.32
AgNP/GSH	368.28 371.18	0 0	94.05 5.95	162.18 162.88 167.98	-1 0 +6	11.64 10.74 77.62
$AgNO_3$/Cys	368.68 369.08	0 0	82.43 17.57	162.18 162.58 169.58	-1 -1 +6	26.51 70.85 2.64
AgNP/Cys	367.65 368.78	+1 0	4.01 95.99	162.48 168.48	-1 +6	83.46 16.54
$AgNO_3$/ME	367.98 368.78	+1 0	30.30 69.70	161.88 162.58 167.78	-2 -1 +4	23.56 74.63 1.81
AgNP/ME	368.08 368.18	+1 0	17.64 82.36	160.68 162.08 167.78	-2 -1 +4	2.96 93.25 3.79
$AgNO_3$/Prt	368.88 369.58	0 0	53.91 46.09	162.08 163.25 168.98	-1 0 +6	21.28 68.20 10.52
AgNP/Prt	368.25 368.95	0 0	14.88 85.12	161.83 162.94	-2 0	22.68 77.32

[a]Charge state assignment based on NIST Standard Reference Database 20, Version 4.1 and literature references.[5,143]

The XPS data shown in Figure 4.6 indicate that there are substantial amounts of oxygen in the precipitates from the AgNP/organothiol and $AgNO_3$/organothiol mixtures. While the presence of oxygen is expected in the Cys-, GSH-, and ME-containing samples, the oxygen in the Prt-containing sample must have originated from sources other than the intact organothiol. One possible source of the oxygen is water trapped inside the AgNPs that was not removed inside the vacuum chamber used in the XPS

analysis. Another possible source is the oxygen associated with oxidized sulfur species such as sulfenate and sulfonate.

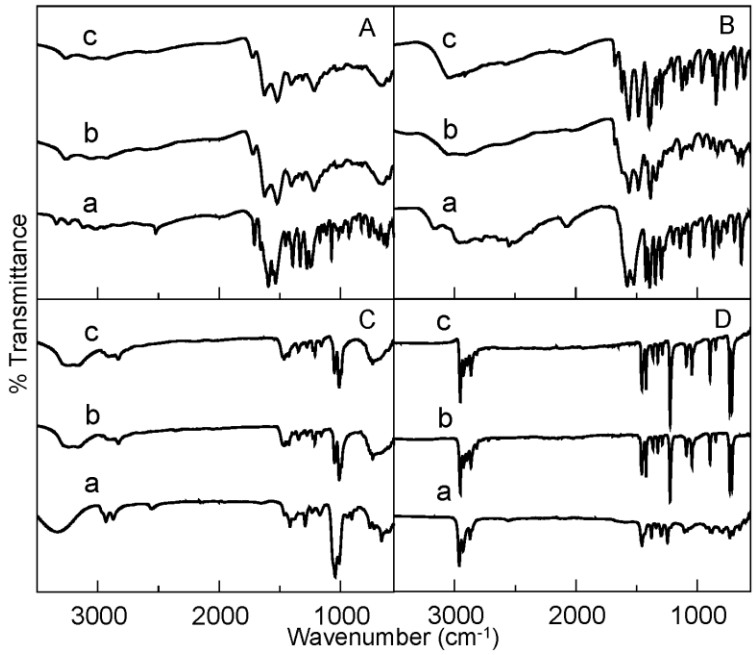

Figure 4.7 ATR-FITR spectra obtained with (a) organothiol control, extensively washed precipitates in (b) $AgNO_3$/organothiol and (c) AgNP/organothiol. The organothiols in (A), (B), (C), and (D) are GSH, Cys, ME, and Prt, respectively.

Note: The Ag:organothiol ratio in all samples are kept to 1:9. The samples were incubated for 3 days before the precipitates were washed and subsequently dried using a lyophilizer overnight before ATR-FTIR measurements.

ATR-FTIR was also employed to study organothiol structure in the washed precipitates in AgNP/organothiol and $AgNO_3$/organothiol solutions (Figure 4.7). The overall IR spectral features in the AgNP/organothiol precipitate are very similar to that observed in the corresponding $AgNO_3$/organothiol precipitates that contain the same organothiol, but they are different from that in the spectrum obtained with the organothiol control. This indicates that organothiol undergoes similar structural modification when it

reacts with AgNPs and $AgNO_3$. This conclusion is consistent with our hypothesis that surface silver on AgNPs is oxidized. Unfortunately, detailed peak assignment was not possible at this time, which limits our ability to identify the organothiol structure and conformation on silver.

4.4.4 Interconversion of fluorescence- and LSPR-active AgNPs

Fluorescence- and LSPR-active AgNPs ($AgNP_{Fluor}$ and $AgNP_{LSPR}$) synthesized by mixing $AgNO_3$ with ME in different molar ratios can be readily interconverted by simply adding excess Ag^+ or ME into the $AgNP_{Fluor}$ /ME or $AgNP_{LSPR}$/ME solutions (Figure 4.8). However, such conversions have not been achieved with the NPs synthesized with other organothiols. This result is consistent with the fact that among these four model organothiols, only NPs in the AgNP/ME mixture exhibit high structural and property similarity to their respective counterparts in the $AgNO_3$/ME mixtures. The discrepancy between ME and the other model organothiols is likely due to ME being drastically more water-soluble than the other organothiols. It is possible that ME induces more rapid and complete AgNP disintegration in the AgNP/ME mixtures before the onset of Ag-thiolate decomposition into small AgNPs. In contrast, AgNP disintegration into Ag-thiolate salts and Ag-thiolate salt decomposition into organothiol-capped AgNPs occur more or less concurrently when AgNPs are mixed with other organothiols.

Organothiols remain attached to both the fluorescence- and LSPR-active AgNPs in both the AgNP/ME and $AgNO_3$/ME solutions. This conclusion is drawn on the basis of the Raman and surface enhanced Raman spectra obtained with the washed precipitates in the AgNP/ME and $AgNO_3$/ME solutions (Figure 4.9). The characteristic S-H stretching feature in the organothiol normal Raman spectra were absent in the Raman spectra of the

precipitates, indicating that the thiol has been converted primarily to thiolate as suggested by the XPS data obtained with the precipitates from the AgNP/ME and $AgNO_3$/ME mixtures.

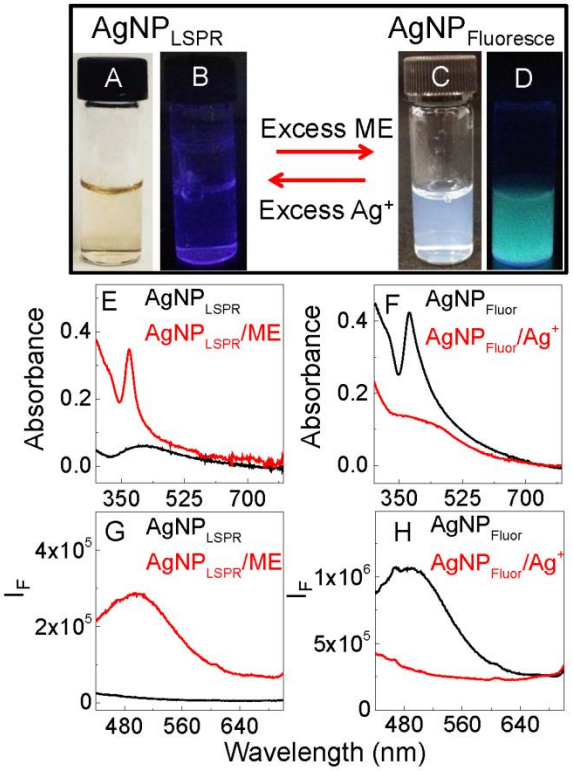

Figure 4.8 Interconversion of fluorescence- and LSPR-active AgNPs. Photographs of the LSPR- active AgNP solutions were taken under (A) visible and (B) UV light. Photographs of the fluorescence -active AgNPs were taken under (C) visible and (D) UV light. UV-vis spectra of (E) (black) $AgNP_{LSPR}$ and (red) ($AgNP_{LSPR}$/ME) solutions, and (F) (black) $AgNP_{Fluor}$ and (red) ($AgNP_{Fluor}/Ag^+$) mixtures. Fluorescence spectra of (G) (black) $AgNP_{LSPR}$ and (red) ($AgNP_{LSPR}$/ME) solutions and (H) (black) $AgNP_{Fluor}$ and (red) ($AgNP_{Fluor}/Ag^+$) mixtures.

Note: $AgNP_{LSPR}$ and $AgNP_{Fluor}$ refer to LSPR- and fluorescence-active AgNPs, respectively. $AgNP_{LSPR}$/ME and $AgNP_{Fluor}/Ag^+$ represent the AgNP solutions after adding excess ME or Ag^+ into the LSPR- or fluorescence-active AgNPs, respectively.

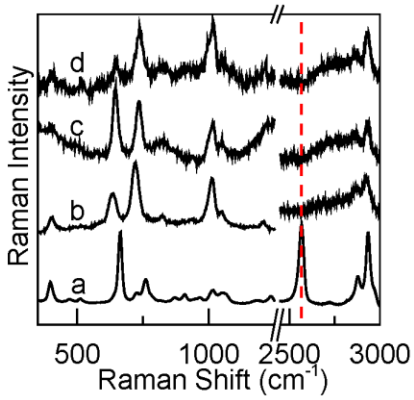

Figure 4.9 Raman or SERS spectra of (a) ME, (b) fluorescence- active AgNPs, (c) LSPR-active AgNPs formed in $AgNO_3$/ME mixture, and (d) fluorescence-active AgNPs in AgNP/ME mixture.

Note: 20% KCl (100 µL) was added to LSPR-active AgNPs formed in $AgNO_3$/ME (9:1) mixture in order to induce the aggregation while obtaining SERS spectra.

4.4.5 Mechanistic study of AgNP disintegration and formation

Negligible AgNP disintegration occurred in AgNP/ME mixtures stored inside an oxygen-free glove-box, in sharp contrast to the complete AgNP disintegration for AgNP/ME mixtures sitting under ambient conditions (Figure 4.10). The LSPR-active AgNPs in the AgNP/ME solution prepared and stored inside the glovebox only aggregated as can be seen in the photograph and UV-vis spectra taken with the mixture. The AgNP LSPR peak around 600 nm is due to the AgNP aggregates formed by AgNPs in the AgNP/ME mixture stored inside the glovebox (Figure 4.10). However, only a UV-vis peak around 370 nm appears in the AgNP/ME solution sitting under ambient conditions for the same period of time, indicating the complete AgNP disintegration. The fact that AgNPs disintegrate only in the ambient AgNP/ME solution, but not in an oxygen-free environment, provides conclusive evidence that it is ambient oxygen, not the organothiols that triggered the AgNP disintegration. No significant AgNP disintegration

was observed in the organothiol-free AgNP control sitting under ambient conditions for the same period of time. This, in conjugation with the data shown in Figure 4.10 indicates that organothiols accelerate the AgNP dissolution by chelating with the silver ion produced by oxygen oxidizing the AgNPs.

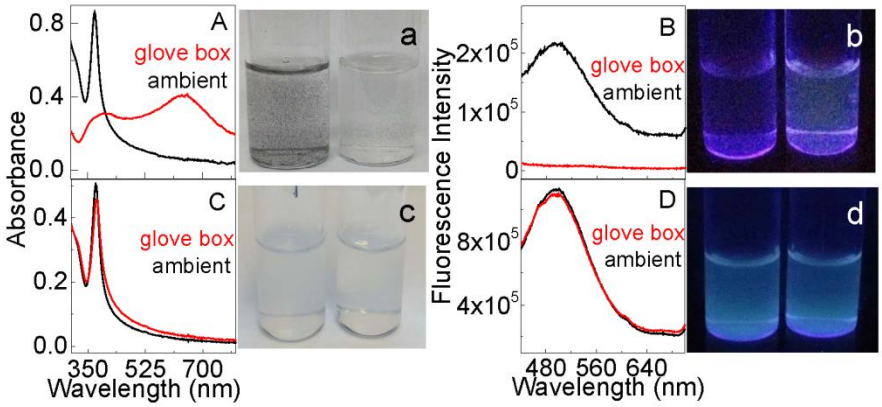

Figure 4.10 Comparison of AgNP disintegration and formation inside oxygen-free glove box and under ambient condition. (A) UV-vis and (B) fluorescence spectra of AgNP/ME mixtures incubated in oxygen-free glove box and ambient conditions. (C) UV-vis and (D) fluorescence spectra of $AgNO_3$/ME mixtures incubated in oxygen-free glove box and ambient conditions.

Note: Samples were incubated 1 day before spectral acquisition. Molar ratio of $AgNO_3$: ME is 1:9 in each mixture. The nominal concentrations of $AgNO_3$ and ME are 0.7 and 6.4 mM, respectively. Photographs: AgNP/ME under (a) visible and (b) UV light. $AgNO_3$/ME under (c) visible and (d) UV light. Glass vials from left to right represent the solutions prepared and stored inside and outside the glove-box, respectively.

In contrast, environmental oxygen has no significant effect on the structure and properties of the NPs observed in the $AgNO_3$/ME mixtures. This is evident from the fact the UV-vis and fluorescence spectra obtained with $AgNO_3$/ME mixtures incubated inside and outside the oxygen-free glove box are nearly identical (Figure 4.10). Since the S-H group is the only functional group that can be reactive with Ag^+ in $AgNO_3$/ME, the

observation of fluorescent active AgNPs is indicative of the thiol reduction of Ag^+ into zero-valence silver atoms.

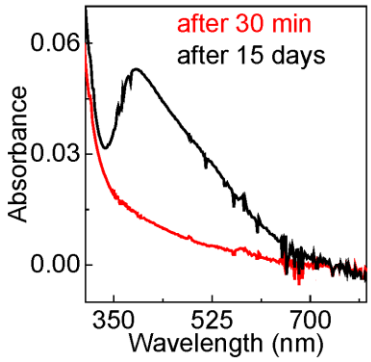

Figure 4.11 UV-vis spectra of $AgNO_3$/HED 9:1 mixture.

Note: The nominal concentration of $AgNO_3$ and HED are 700 and 39 μM, respectively.

Attempts to determine the structure and composition of the oxidized organothiols in the $AgNO_3$/organothiol and AgNP/organothiol mixtures were unsuccessful. However, organothiols reducing Ag^+ to zero valence silver nanomaterial can be readily understood on the basis of the redox potential of thiol. The redox potential of thiol-disulfide (RS-H/RS-SR) conversion is -0.2 V,[144,145] significantly smaller than the standard redox potential of Ag^+ (0.799 V).[36] Furthermore, AgNP formation was also observed in control experiments conducted with 2-hydroxyethyl disulfide (HED, HO-CH_2-CH_2-S-S-CH_2-CH_2-OH) mixed with $AgNO_3$ (Figure 4.11). This result indicates that disulfide can also reduce Ag^+ into zero valence Ag. However, the sample incubation time for the AgNP LSPR peak to appear in the $AgNO_3$/HED mixtures is significantly longer than that in $AgNO_3$/ME (~15 days versus 3 days), suggesting that reduction of Ag^+ by thiol is

significantly faster than that by disulfide. This result is consistent with the fact that the thiol (S-H) is a stronger reducing agent than disulfide (S-S).

The Ag^+ conversion into AgNPs in the $AgNO_3$/HED mixture implies that the zero valence sulfur in disulfide must be further oxidized by Ag^+ into higher oxidation states. This is to our knowledge, the first direct experimental evidence of the disulfide reducing Ag^+. This result can explain the sulfonic/sulfenic species observed in the XPS spectra obtained with the precipitates in the $AgNO_3$/Cys, $AgNO_3$/Prt, and $AgNO_3$/GSH mixtures (Figure 4.6). This observation that disulfide can convert Ag^+ into AgNPs should also be important for understanding the fate of AgNPs in biological systems that are rich sources of both free and disulfide-linked thiols.

4.4.6 Gold nanoparticle formation in $HAuCl_4$/organothiol mixtures

No AuNP disintegration was observed in any of the AuNP/organothiol mixtures (Figure 4.12). Only a monolayer of organothiols was adsorbed onto the AuNP surfaces. This is in sharp contrast with the AgNP disintegration observed in the AgNP/organothiol mixtures (Figure 4.1). This result is not surprising given the fact that gold has a significantly higher standard redox potential than silver.

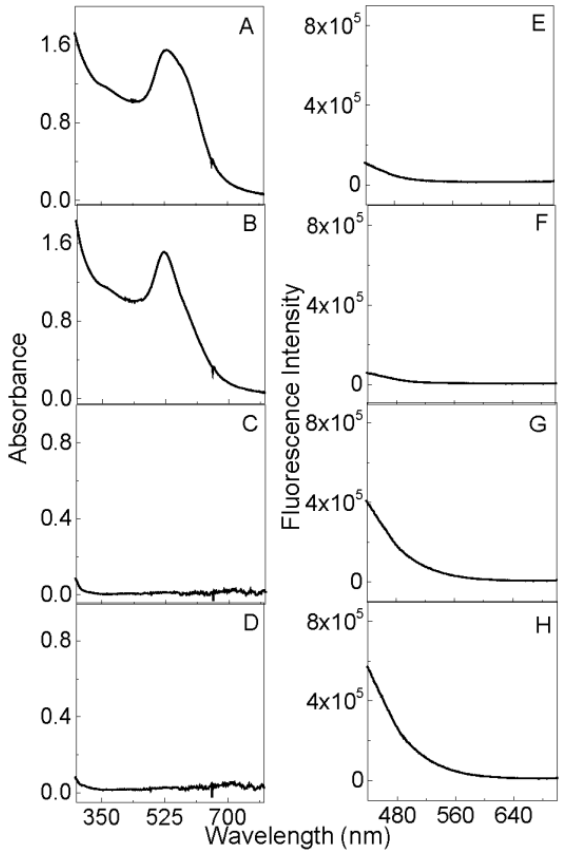

Figure 4.12 UV-vis spectra of AuNPs after the addition of (A) GSH, (B) Cys, (C) ME, and (D) Prt. (E) - (H) represent the respective fluorescence spectra.

Note: The nominal concentrations of AuNPs and organothiols were 7 nM and 4.7 mM.

Organothiols can also reduce Au^{3+} into fluorescence- and LSPR-active AuNPs in the $HAuCl_4$/organothiol mixtures by simply changing the Au^{3+} and organothiol concentration ratio (Figure 4.13 and Figure 4.14). Fluorescent-active AuNPs were observed when the organothiol is in excess (Figure 4.13), but only LSPR-active AuNPs were obtained when Au^{3+} is in excess (Figure 4.14). No significant fluorescence activity was observed with the LSPR-active AuNPs. These results are very similar to those observed in the $AgNO_3$/organothiol mixtures. Indeed, reduction of Au^{3+} by organothiols

should be thermodynamically more favorable than that for Ag^{+} because the Au^{3+} has a higher standard redox potential than silver.

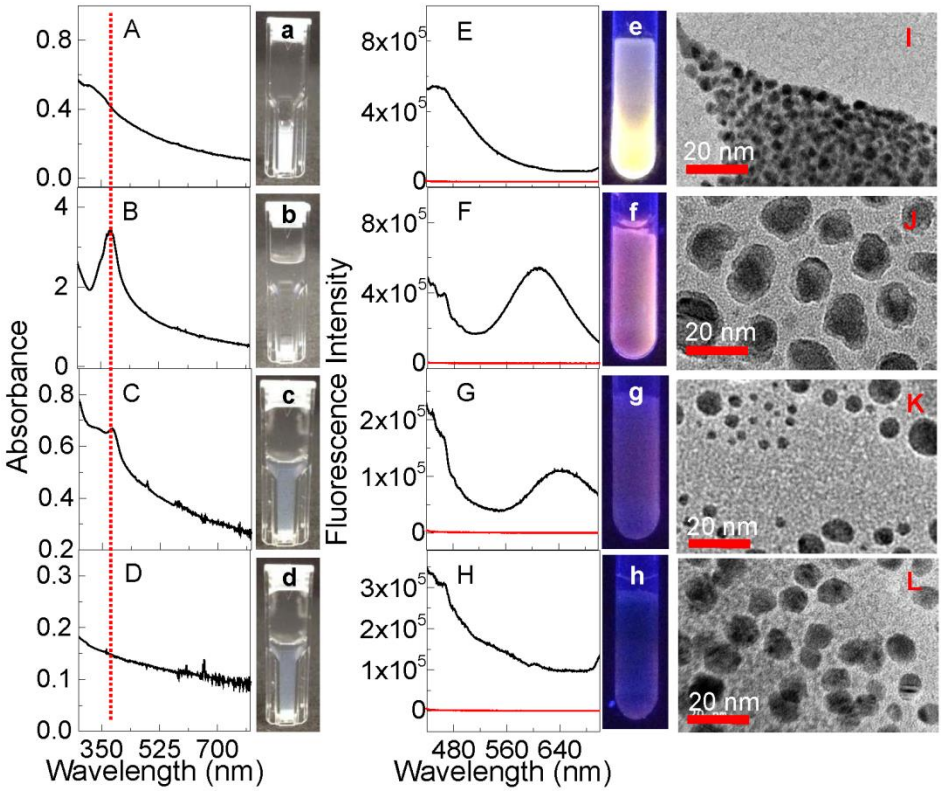

Figure 4.13 Thiol-induced fluorescence active AuNP formation. UV-vis spectra of (A) $HAuCl_4$/GSH, (B) $HAuCl_4$/Cys, (C) $HAuCl_4$/ME, and (D) $HAuCl_4$/Prt, respectively. Fluorescence spectra of (E) $HAuCl_4$/GSH, (F) $HAuCl_4$/Cys, (G) $HAuCl_4$/ME, and (H) $HAuCl_4$/Prt, respectively. Photograph of samples under (a-d) visible and (e-h) UV light. TEM images of (I) $HAuCl_4$/GSH, (J) $HAuCl_4$/Cys, (K) $HAuCl_4$/ME, and (L) $HAuCl_4$/Prt, respectively.

Note: Fluorescence excitation wavelength was 370 nm. UV-vis and fluorescence spectra were obtained 1 day after sample preparation. The molar ratio of $HAuCl_4$:organothiol was 1:9 in each mixture. The nominal concentrations of $HAuCl_4$ and organothiols are 0.7 and 6.4 mM, respectively

When excited at 370 nm, the peak emission wavelength for fluorescence-active AuNPs varies from 456 nm, 609 nm, and 648 nm for GSH, Cys, and ME, respectively

(Figure 4.13). This is compared to emission wavelengths of 536 nm, 456 nm, and 500 nm of the fluorescent-active AgNP synthesized with this same series of organothiols at the same excitation wavelength (Figure 4.4). This result indicates that the emission wavelength of the GSH-based bottom-up AuNPs is blue-shifted by 80 nm relative to its AgNP counterpart, but red-shifted by more than 100 nm for the AuNPs synthesized with ME and Cys in comparison to their respective AgNP counterparts. The AuNPs in the $HAuCl_4$/Prt mixture have a broad continuum emission with no well-defined features (Figure 4.13). This is similar to what has been observed with its AgNP counterpart. The fact that organothiol-containing noble metal nanoparticles can differ so significantly in their structures and properties further highlights the complexity of organothiol interactions with AgNPs and AuNPs. Our data indicate that changes in the organothiol structures, metal type, and the concentration ratios of metal precursor and organothiol concentrations can have drastic features on the optical properties of the nanomaterials. Indeed, Liu et al. showed that fluorescence-active AuNPs can be obtained only with PEG-SH with nominal molecular weight of ~1000 g/mol, but not with molecular weight of 5000 or 350 g/mol.[146]

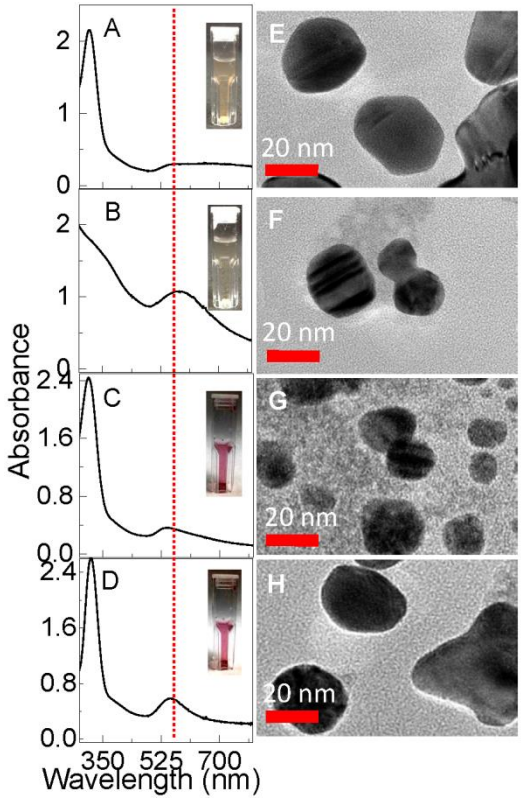

Figure 4.14 Thiol-induced AuNP formation. UV-vis spectra of (A) $HAuCl_4$/GSH, (B) $HAuCl_4$/Cys, (C) $HAuCl_4$/ME, and (D) $HAuCl_4$/Prt, respectively. TEM images obtained with (E) $HAuCl_4$/GSH (F) $HAuCl_4$/Cys, (G) $HAuCl_4$/ME, and (H) $HAuCl_4$/Prt, respectively.

Note: Insets: the photographs of respective mixtures after the NP formation. The molar ratio of $HAuCl_4$:organothiol was 9:1 in all mixtures. The nominal concentrations of $HAuCl_4$ and organothiols are 700 and 78 μM, respectively. Solutions were incubated for 3 days before UV-vis and TEM characterization.

4.5 Conclusions

Organothiol interactions with AgNPs are highly complicated in nature. In general, organothiols accelerate, but do not passivate AgNPs against oxidative disintegration of the AgNPs. Only organothiols such as alkanethiols that can form densely packed and highly ordered conformations can kinetically reduce the AgNP disintegration rate under ambient conditions; other organothiols including aromatic and amino-acid thiols are not

adequate for passivating AgNP from oxidative disintegration. The initial products of the disintegrated AgNPs in the AgNP/organothiol mixtures are likely silver-thiolate salts. However, these salts are eventually converted into fluorescence- or LSPR-active AgNPs capped by organothiols. This work provided the first conclusive evidence of the contradictory dual effect of organothiols on AgNPs in which organothiols induce both AgNP disintegration and formation. The insights from this work should be of general importance for plasmonic nanoparticle synthesis and applications where free or disulfide-linked thiols are commonly present.

Notes: This work has been previously published: Siriwardana, K.; Suwandaratne, N.; Perera, G. S.; Collier, W. E.; Perez, F.; Zhang, D., Contradictory Dual Effects: Organothiols Can Induce Both Silver Nanoparticle Disintegration and Formation under Ambient Conditions. *J. Phy. Chem. C* **2015**, *119*, 20975-20984.

CHAPTER V

CRITICAL SEQUENCE DEPENDENCE IN MULTICOMPONENT LIGAND BINDING TO GOLD NANOPARTICLES

(Published in *J. Phys. Chem. C* **2016,** *120*, 6900-6905)

5.1 Abstract

Multicomponent ligand interactions are involved in essentially all practical nanoparticle (NP) applications. Presented herein is the finding that multicomponent ligand binding to gold nanoparticles (AuNPs) can be highly dependent on the sequence of ligand mixing with AuNPs. Quantitative study revealed that the competitive adenine and glutanthione (GSH) adsorption onto both as-synthesized and pegylated AuNPs are predominantly kinetically-controlled, and adenine that binds only nonspecifically to AuNP adsorb faster than GSH. This raises concerns about the validity of the popular practice in current NP research of using the Langmuir isotherm or its variants to model multicomponent ligand adsorption on NPs. Mechanistically, this sequence dependency is due to the fact that there is no spontaneous ligand desorption even for the model protein and small molecules that can bind only nonspecifically to AuNPs. The insights and experimental methods provided in this work should be important for molecular-level understanding of nanoparticle interfacial interactions.

5.2 Introduction

Understanding gold nanoparticle (AuNP) interfacial interactions including ligand adsorption, desorption, and reactions, is critical for essentially all NP applications. This is because surface functionalization is commonly used to improve AuNP stability, biocompatibility, and target specificity in biological applications.[9,42,147] Multicomponent ligand interactions are usually present when AuNPs are added into complex mixtures such as biofluids. In this case, organic, inorganic, and biological molecules can bind to AuNPs through either the formation of covalent bonds with AuNPs (Au-S bond) or nonspecific intermolecular forces involving electrostatic interactions, van der Waals interactions, and ion-pair formation.[44,46,148] Further ligand interaction is also possible even when the AuNPs are prefunctionalized with ligands such as proteins,[53] thiolated poly(ethylene glycol) (PEG-SH),[56,83,149] and small molecules.[52] While there is tremendous interest in the synthesis and characterization of multicomponent functionalized nanoparticles for their applications in drug delivery,[150,151] cancer imaging,[152] and solar energy harvesting,[153] fundamental understanding of the multicomponent ligand interaction is limited. One popular belief is that multicomponent ligand binding is a thermodynamically controlled process, and the ligand composition on the nanoparticles can thereby modelled with the Langmuir adsorption isotherm or its variants.[21,65,154] The validity of this approach has, however, not been critically examined. Indeed, one must experimentally verify that a ligand binding system is indeed in an equilibrial state before the determination of its equilibrium binding constant and binding capacity.

Presented herein is the finding that multicomponent ligand binding to both as-synthesized and pegylated AuNPs (pAuNPs) can be critically dependent on the sequence of ligand addition to the AuNP solution. This challenges the current practice in nanoparticle research where the ligand binding to NPs was commonly assumed to be thermodynamically controlled, and thereby sequence-independent according to the Hess's law. Proteins and small molecules with different AuNP binding affinities were used as the model ligands. For the sake of simplicity, we will use A/B/C to represent the mixture solutions of A, B and C, and (A/B)/C to represent a mixture prepared by mixing A and B before the addition of C.

The model proteins used in this work consist of wild-type protein GB3 containing no cysteine residues,[110,111] , and two genetically modified GB3 proteins in which one or two amino-acid residues in the wild-type GB3 has been modified genetically into Cys.[155] The wild-type and mutated GB3 proteins are referred to as $GB3_0$, $GB3_1$, and $GB3_2$ with the subscripts representing the number of Cys residues. The sequential and simultaneous adsorption of $GB3_0$, $GB3_1$ or $GB3_2$ to AuNPs was probed using 2-mercaptobenzimidazole (2-MBI) as the molecular probe. Previous research has shown that, as a thione/thiol tautomer,[84,156] 2-MBI displaces nonspecifically adsorbed proteins from AuNPs and induced AuNP aggregation and precipitation, but has no significant effect on the dispersion stability of AuNPs that are pre-functionalized with cysteine-containing proteins.[43,54]

5.3 Experimental section

5.3.1 Materials and instruments

All chemicals except PEG-SH (5000 g/mol) were purchased from Sigma-Aldrich and used as received. PEG-SH was purchased from Layson Bio Inc., and the PEG-SH solutions were dialyzed using 3500 molecular weight cut off dialysis membranes prior to the PEG-SH mixing with AuNPs. Nanopure water (18.2 MΩ cm) was used in sample preparation. AuNPs were synthesized using the citrate reduction method.[92] The AuNP pegylation is performed by incubating the AuNPs with the PEG-SH for a predefined period of time, and the spontaneous PEG-SH adsorption onto AuNPs was confirmed with UV-vis spectra before and after the pegylation and the enhanced AuNP dispersion stability after the pegylation. GB3 proteins were prepared in-house and purified with published procedures.[43] The concentration of the GB3 variants was determined on the basis of their UV-vis absorbance at 280 nm.[43] An Olis HP 8452 A diode array spectrophotometer was used for the UV-vis measurements. A bench top centrifuge machine (Eppendorf AG centrifuge 5424) was used for centrifugation precipitation of the pAuNPs needed for the quantification of the adenine adsorption in the multicomponent adenine and GSH binding to pAuNPs experiments.

5.3.2 GB3 protein binding to AuNPs

All (AuNP/$GB3_0$/$GB3_i$)/2-MBI (i=1 or 2) solutions were prepared in a similar way. In short, 0.5 mL of as-synthesized AuNPs were mixed with an equal volume of 30 μM $GB3_0$ and $GB3_i$ solutions according to the specified sequence. In the sequential protein binding to AuNP experiment, AuNPs were first mixed with one protein solution and incubated overnight before the addition of the second protein solution.

(AuNP/$GB3_0$/$GB3_i$) solutions were further incubated overnight and 3 days before the addition of 0.5 mL 30 μM 2-MBI. Therefore, there are a total of 3 day time period for the proteins to adsorb and exchange on AuNP surfaces before 2-MBI addition. This long incubation (3 days) time should be adequate for the proteins to reach equilibrium binding if the multicomponent protein binding to AuNP is indeed thermodynamically controlled. The UV-vis characterization of the AuNP stability in the (AuNP/$GB3_0$/$GB3_i$)/2-MBI (i=1 or 2) solutions were conducted the day after adding the 2-MBI solution. The experimental results shown in the main text were all obtained with samples incubated in the refrigerator (4 °C). Similar experimental results were obtained with the samples prepared at ambient conditions.

5.3.3 GSH and adenine binding to AuNPs and pAuNPs

All (AuNP/adenine/GSH) and (pAuNP/adenine/GSH) solutions were prepared similarly. In brief, 0.5 mL of as-synthsized AuNPs or pAuNPs were mixed with an equal volume of 30 μM adenine and GSH according to the sequence specified in the results and discussion section. In the sequential GSH and adenine binding to AuNP/pAuNP experiment, AuNPs/pAuNPs were first incubated with one ligand overnight before the addition of the second ligand. After the addition of the second ligand, the solutions were again incubated overnight before the UV-vis quantification of the amount of adenine adsorbed onto the AuNPs.

5.3.4 Probing spontaneous ligand desorptions

Possible spontaneous adenine desorption was studied for adenine adsorbed onto the as-synthesized AuNPs and pAuNPs, respectively. 3 mL of 30μM adenine was added

to 3 mL of as-synthesized AuNPs and the resulting mixture was incubated overnight. The spontaneous adenine adsorption induced complete AuNP aggregation and precipitation. The amount of adenine adsorbed was quantified directly by UV-vis quantification of the adenine remaining free in the supernatant.

To probe possible spontaneous adenine desorption, the precipitated adenine-containing AuNPs were washed 10 times with water. Each washing consists of replacing 5.9 mL of the supernatant of the adenine-containing AuNP aggregates with an equal volume of water, followed by vortexing. The vortexed solution was allowed to sit for ~30 min to allow the adenine-containing AuNPs to settle to the bottom of glass vial before the subsequent washing cycle. The final washed solution was left to sit 2 days at ambient conditions to allow further desorption to occur if adenine on the AuNPs can be spontaneously desorbed. The total desorption time including the washing and solvent incubation is about 3 days, which is significantly longer than the time used in typical ligand adsorption, desorption, and exchange experiments.

Ligand displacement was used to probe the adenine remaining adsorbed onto the washed and 2 days incubated sample of AuNP aggregates. We used the small thiol 2-mercaptoethanol (ME) as the displacing agent. 20 μL of ME (14.3 M) was added to the 6 mL of washed adenine-containing AuNP aggregates solution to displace the adenine. 30 min after adding the ME, the UV-vis quantification of the adenine displaced from washed adenine-containing AuNPs was conducted.

The possible spontaneous adenine desorption from the pAuNPs was studied using procedures very similar to what is described above for the as-synthesized AuNPs. The only difference is that before each washing and adenine quantification, the adenine-

containing pAuNPs were centrifuged at 9000 rpm for 45 min to induce precipitation of the pAuNPs. The amount of the adenine adsorbed onto the pAuNPs and desorbed from the washed pAuNPs were both quantified with UV-vis spectra of the centrifugation supernatant.

5.4 Results and discussion

All GB_3 proteins spontaneously assemble onto AuNP surfaces. This is deduced from the red-shift of the AuNP surface plasmonic resonance (SPR) peak wavelength and the increased SPR peak absorption induced by GB3 protein addition to the AuNP control (Figure 5.1A). However, these GB3 variants differ significantly in their ability to protect AuNPs against 2-MBI-induced AuNP aggregation and precipitation. Adding 2-MBI to (AuNP/$GB3_0$) solutions induces immediate AuNP aggregation, and complete precipitation after overnight incubation (Figure 5.1B), while 2-MBI addition only induces limited AuNP aggregation in the (AuNP/$GB3_1$)/2-MBI solution with no detectable AuNP precipitation. In contrast, AuNPs in the (AuNP/$GB3_2$)/2-MBI sample are totally stable with no significant AuNP aggregation even after 3 days incubation with 2-MBI (Figure 5.1B). This observation is consistent with the previous observation that prefunctionalization of AuNPs with $GB3_2$ and the protein bovine serum albumin (BSA) can totally protect the AuNPs from 2-MBI-induced AuNP aggregation and precipitation.[43,53,54] It also provides direct evidence of the critical importance of cysteine residues in protein binding to AuNPs.

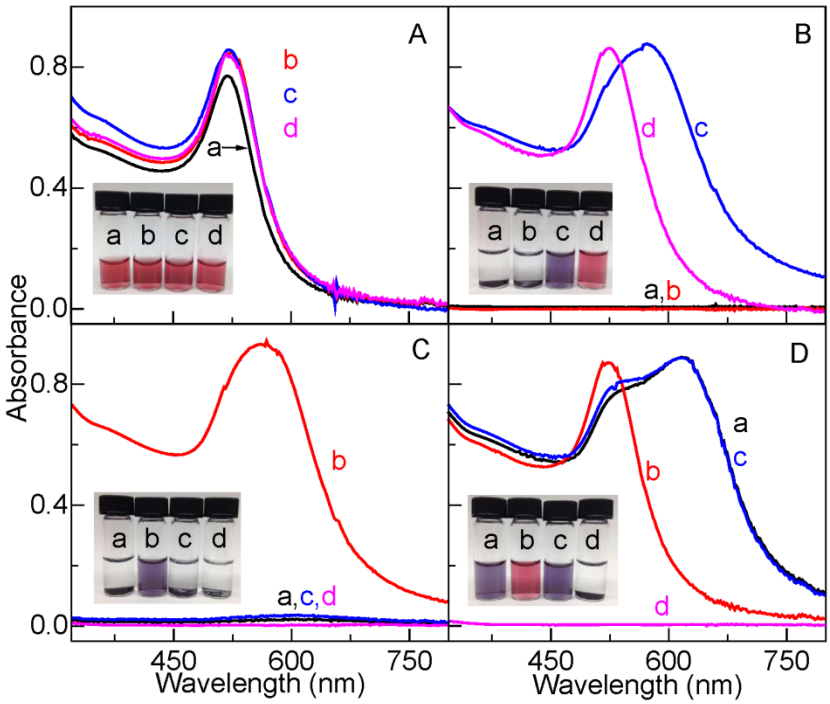

Figure 5.1 (A) UV-vis spectra and photographs of (a) AuNP, (b) AuNP/GB3$_0$, (c) AuNP/GB3$_1$, and (d) AuNP/GB3$_2$. (B) UV-vis spectra and photographs of (a) AuNP/2-MBI, (b) (AuNP/GB3$_0$)/2-MBI, (c) (AuNP/GB3$_1$)/2-MBI, and (d) (AuNP/GB3$_2$)/2-MBI. (C) UV-vis spectra and photographs of (a) (AuNP/GB3$_0$)/GB3$_1$/2-MBI, (b) (AuNP/GB3$_1$)/GB3$_0$/2-MBI, (c) (AuNP/(GB3$_0$/GB3$_1$))/2-MBI, and (d) (AuNP/2-MBI)/(GB3$_0$/GB3$_1$). (D) UV-vis spectra and photographs of (a) (AuNP/GB3$_0$)/GB3$_2$/2-MBI, (b) (AuNP/GB3$_2$)/GB3$_0$/2-MBI, (c) (AuNP/(GB3$_0$/GB3$_2$))/2-MBI, and (d) (AuNP/2-MBI)/(GB3$_0$/GB3$_2$).

Note: Only the supernatant is used for the UV-vis measurement of the samples where the AuNPs are aggregated. The samples in (B), (C) and (D) are prepared such that the third component in the mixture was added after the first two components were mixed and incubated overnight, and the fourth component was added one day after the addition of third component. The nominal concentration of AuNPs, proteins, and 2-MBI were 3 nM, 7.5 µM, and 7.5 µM, respectively.

The difference among the GB3 proteins in their ability to protect AuNPs from 2-MBI-induced aggregation and precipitation provides a convenient way to probe the possible sequence dependence of multicomponent protein interactions with AuNPs.

Addressing this issue is critical for evaluating whether or not multicomponent protein binding is indeed thermodynamically controlled. The data in Figure 5.1 indicates that the AuNP dispersion stability against 2-MBI-induced AuNP aggregation and precipitation in the (AuNP/$GB3_0$/$GB3_i$)/2-MBI (i=1, 2) solutions depends critically on the sequence of mixing $GB3_0$ and $GB3_i$ with AuNPs (Figure 5.1 C and D). The AuNPs in the ((AuNP/$GB3_1$)/$GB3_0$)/2-MBI solution only aggregated, as observed in the (AuNP/$GB3_1$)/2-MBI solution, but completely aggregated and precipitated in the ((AuNP/$GB3_0$)/$GB3_1$)/2-MBI and (AuNP/($GB3_0$/$GB3_1$))/2-MBI solutions, as observed in the (AuNP/$GB3_0$)/2-MBI solution. This is in spite of the fact that the sample composition in these (AuNP/$GB3_0$/$GB3_1$)/2-MBI solutions is exactly the same. Similar sequence dependence was observed among the three (AuNP/$GB3_0$/$GB3_2$)/2-MBI solutions with identical solution compositions but with different mixing sequences. AuNPs in ((AuNP/$GB3_2$)/$GB3_0$)/2-MBI solutions are entirely stable, but AuNPs in ((AuNP/$GB3_0$)/$GB3_2$)/2-MBI solutions are significantly aggregated.

The sequence dependence data shown in Figure 5.1 were conducted with (AuNP/$GB3_0$/$GB3_i$)/2-MBI samples in which the (AuNP/$GB3_0$/$GB3_i$) solutions were incubated overnight before 2-MBI addition. Similar sequence dependence was observed in (AuNP/$GB3_0$/$GB3_i$)/2-MBI solutions where the (AuNP/$GB3_0$/$GB3_i$) (i=1, 2) solutions were incubated for 3 days before the 2-MBI addition. This incubation time should be long enough for $GB3_0$ and $GB3_1$ or $GB3_2$ to reach equilibrium binding to the AuNP surface if the multicomponent ligand binding is indeed thermodynamically controlled. These sequence dependence excluded the possibility for $GB3_0$ and $GB3_1$ or $GB3_2$

proteins to reach equilibrium binding on the AuNPs even after 3 days of the sample incubation.

In addition to proteins, the multicomponent binding between small molecules to AuNPs can also be strongly sequence-dependent. Figure 5.2 shows the experimental data obtained with sequential and simultaneous adenine and glutathione (GSH) adsorptions onto as-synthesized and pAuNPs, respectively. The AuNP stability and the amount of the adenine adsorbed onto both (AuNP/GSH/adenine) and (pAuNP/GSH/adenine) solutions depend strongly on the sequence of GSH and adenine addition to the AuNP solutions. As an example, there is negligible adenine adsorption if the AuNPs are first mixed with GSH before adenine (Figure 5.2). However, substantial adenine is adsorbed onto the AuNP surface if the adenine is added first to AuNPs before GSH addition or adenine is added together with GSH to AuNPs (Figure 5.2). It is noted that again that the sample composition of all the (AuNP/GSH/adenine) samples and the (pAuNP/GSH/adenine) samples is totally identical. Furthermore, the adenine adsorption was quantified 3 days after the addition of the final component. This sample incubation time should be entirely adequate for thermodynamically controlled multicomponent ligand adsorption to reach equilibrium. The sequence dependence observed in the simultaneous adenine and GSH binding indicates that even for small molecular ligands, their binding to AuNPs can deviate significantly from Langmuir or its variants.

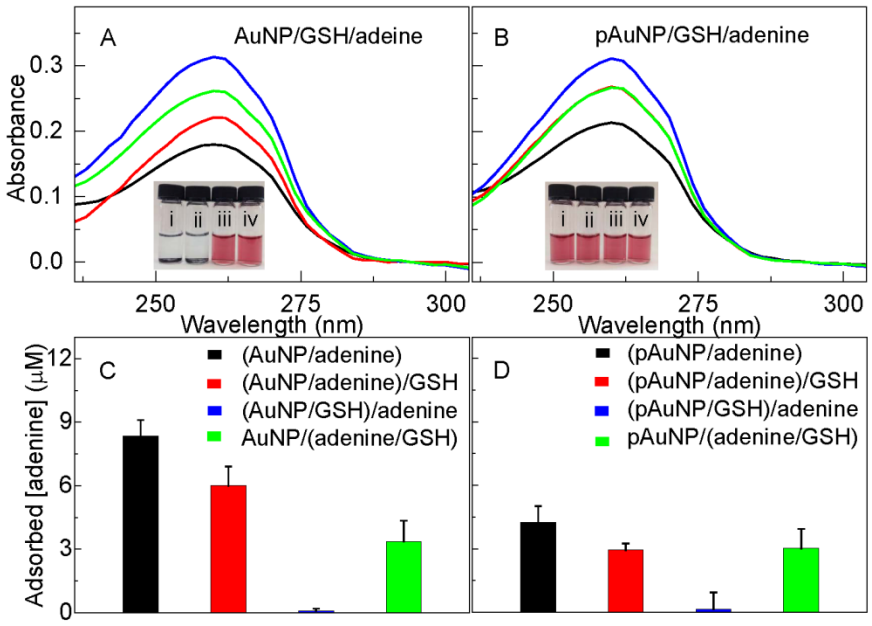

Figure 5.2 (A) UV-vis spectra of supernatant in (black) the (AuNP/adenine) and (red) (AuNP/adenine)/GSH solutions, and the centrifuge supernatants of the (blue) (AuNP/GSH)/adenine and (green) AuNP/(GSH/adenine) solutions. (B) UV-vis spectra of centrifuge supernatant of (black) (pAuNP/adenine), (red) (pAuNP/adenine)/GSH, (blue) (pAuNP/GSH)/adenine, and (green) pAuNP/(GSH/adenine) mixtures. Quantitative comparison of adenine adsorption onto (C) as-synthesized AuNPs and (D) pAuNPs.

Note: The vials from left to right in the inset of (A) are (i) (AuNP/adenine), (ii) (AuNP/adenine)/GSH, (iii) (AuNP/GSH)/adenine, and (iv) AuNP/(GSH/adenine), respectively. The vials from left to right in the inset of (B) are (i) (pAuNP/adenine), (ii) (pAuNP/adenine)/GSH, (iii) (pAuNP/GSH)/adenine, and (iv) pAuNP/(GSH/adenine), respectively. Error bars in C and D represent one standard deviation from three independent measurements. All samples were prepared such that the third component was added after the first two components were mixed overnight. The nominal concentrations of AuNP or pAuNP were 4 nM. GSH and adenine were 10 μM.

The amount of adsorbed adenine in (pAuNP/(GSH/adenine)) is highly similar to that in ((pAuNP/adenine)/GSH), but significantly different from ((pAuNP/GSH)/adenine). A Similar sequence depending on the adenine absorption is observed for the GSH and adenine binding to the as-synthesized AuNPs in which the

amount of adenine adsorbed in the (AuNP/(GSH/adenine)) sample is similar to that in ((AuNP/adenine)/GSH), but significantly different from that in ((AuNP/GSH)/adenine). These results have several important implications. First, adenine adsorbed faster than GSH onto AuNPs despite of fact that adenine can bind only nonspecifically to AuNPs, but GSH forms covalent Au-S bonding to gold. Second, the competitive adenine and GSH binding to AuNP is predominantly kinetically controlled. Otherwise, the amount of adsorbed adenine in (pAuNP/(GSH/adenine)) and ((pAuNP/adenine)/GSH) should be much more similar to that in ((pAuNP/GSH)/adenine). Third, one must be cautious to interpret ligand displacement data. The fact one ligand can displace a previously adsorbed ligand can serve as reliable indicator that the incoming ligand has higher binding affinity to NP than the initial ligands, but two ligand can be simultaneously adsorbed to NP doesn't necessarily mean that the two ligands have comparable NP binding affinity.

Mechanistically, the ligand exchange on NP surfaces must occur for a multicomponent ligand binding to be fully thermodynamically controlled. Otherwise, the ligand first adsorbed (because of the faster kinetics or earlier addition) onto NP will dominate the surfaces. There are two ligand exchange pathways.[20,51,157-159] The first is dissociative exchange pathway in which the initial ligand spontaneously desorbed from the host NP and the incoming ligand can then compete with the initial ligand for the unoccupied surface.[157,158,160] This process usually leads to equilibrium binding in which the stronger binder will dominate the NP surfaces. The second pathway is associative exchange in which the incoming ligand must first penetrate onto the NP surface and co-adsorb with the initial ligand before triggering the release of the initial ligand.[20,159,161-163]

This is the only possible pathway for ligands to exchange if the initial ligand cannot be spontaneously desorbed from the NP surfaces. In this case, steric hindrance imposed by the initial ligand on the NP surface can prevent the multicomponent ligand binding to reach equilibrium. One extreme example is that for NPs fully covered by an initial ligand that cannot undergo spontaneous desorption, subsequent ligand binding is impossible regardless of how much greater the NP binding affinity of the incoming ligand is than the initial ligand. Under this hypothetic situation there is no chance for the incoming ligands to even "see" the NP surface, let alone their NP binding.

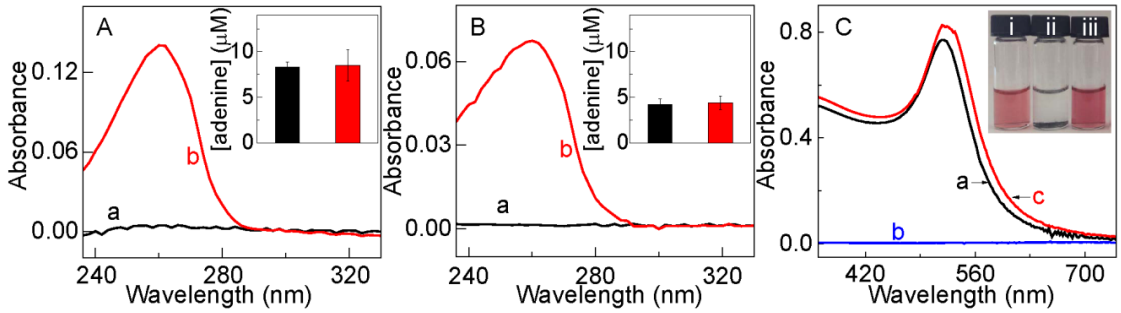

Figure 5.3 (A) (a) UV-vis spectrum of the supernatant of the washed (AuNP/adenine) mixture acquired 2 days after extensive solvent washing. The UV-vis spectrum (b) was obtained 30 min after adding ME to displace adenine adsorbed onto the washed adenine-containing AuNPs. (B) (a) UV-vis spectrum of the centrifuge supernatant of washed adenine-containing pAuNPs in its final washing solution for 2 days. The UV-vis spectrum (b) was obtained 30 min after adding ME, to displace adenine adsorbed onto the washed adenine-containing pAuNPs. (C) UV-vis spectra of (a) AuNP control, (b) (AuNP/adenine), and (c) (AuNP/$GB3_0$)/adenine, respectively.

Note: The experimental procedure of solvent washing is in the experimental section. The insets in (A) and (B) compare the adenine adsorbed onto the as-synthesized and pAuNPs, both (black) before and (red) after the solvent washing. Error bars are one standard deviation of three independent measurements. Inset in (C) are photograph of (i) AuNPs, (ii) (AuNP/adenine) and (iii) (AuNP/$GB3_0$)/adenine solutions. The nominal concentration of AuNP or pAuNP was 4 nM. The nominal concentration of adenine, ME, and $GB3_0$ was 10 μM.

The reason for the strong sequence dependence described above is the fact that once adsorbed neither the model protein nor the small molecule ligands can spontaneously desorb from the NP surface. This conclusion is drawn from experimental data obtained with adenine and $GB3_0$, the two model ligands that can bind only nonspecifically to AuNPs (Figure 5.3). There is no significant difference between the amount of the adenine adsorbed onto the AuNPs and that displaced from the washed adenine-containing AuNPs. This excludes the possibility that there is any substantial spontaneous adenine desorption from the AuNP surfaces during the washing process. Otherwise, the amount of adenine displaced from the washed adenine-containing AuNP samples should be significantly smaller than the adenine initially adsorbed onto AuNPs.

The possible spontaneous $GB3_0$ desorption is examined indirectly through the adenine-induced AuNP aggregation experiment (Figure 5.3). The adenine binding to the as-synthesized AuNP induces AuNP aggregation and precipitation. However, no significant AuNP aggregation was observed in the (AuNP/$GB3_0$)/adenine solutions. This is in sharp contrast to the observation that AuNPs are entirely aggregated and precipitated in (AuNP/$GB3_0$)/2-MBI solution (Figure 5.1). Since adenine has very similar molecular dimensions to 2-MBI, it should also be able to penetrate through the $GB3_0$ overlayer on AuNP. The fact that 2-MBI, but not adenine, can destabilize the $GB3_0$-functionalized AuNPs indicates that $GB3_0$'s binding affinity to AuNPs is smaller than that of 2-MBI, but higher than that of adenine. Since adenine cannot be spontaneously desorbed from AuNPs, the possibility for $GB3_0$ to spontaneously desorb from AuNPs should be entirely negligible.

The higher 2-MBI binding affinity to AuNPs than $GB3_0$ and adenine can be understood easily because 2-MBI forms covalent bonds with AuNPs.[19,84] In contrast, $GB3_0$ and adenine can only bind nonspecifically to AuNPs. The higher $GB3_0$ binding affinity to AuNP than adenine is not surprising either given the fact that as a protein, $GB3_0$ can form multivalent interactions with AuNPs with its multiple amino acid residues. The $GB3_0$ van der Waals interaction with AuNPs is also likely much greater than that of adenine because $GB3_0$ has larger molecular weight. Since most proteins have even larger molecular weights than $GB3_0$ (6208 g/mol)[111] and many of them contain one or more cysteine residues, it is likely to be a general phenomenon that once adsorbed, proteins on the AuNP surface cannot be spontaneously desorbed.

The data presented in Figure 5.3 are to our knowledge the first experimental study of the possibility of spontaneous ligand desorption from AuNP surfaces. Thermodynamically, removal of the excess ligand in a solution should cause ligand desorption to reestablish a new equilibrium. However, such a new equilibrium is possible only when the ligand desorption activation energy is low enough to allow spontaneous desorption to occur at ambient conditions. The data shown in Figure 5.3 indicate that even for ligands that can bind only nonspecifically to AuNPs, their desorption activation energy can be too high for significant spontaneous ligand desorption to occur.

5.5 Conclusions

In conclusion, we demonstrated using both protein and small molecule ligands that multicomponent ligand adsorption onto the AuNPs can be highly sequence-dependent, in that the structures and properties of the ligand-containing AuNPs depends not only on the ligand concentrations but also on their sequence of mixing with AuNPs.

The main reason is that even nonspecifically adsorbed ligands can have prohibitively high desorption activation energies, which prevents significant spontaneous desorption. Consequently, the ligand exchange can proceed only through an associative exchange pathway in which the incoming ligand has to be able to penetrate through the overlayer of the initial ligand on the NP surfaces to trigger the ligand displacement. This makes reaching an equilibrium state for multicomponent ligand binding to AuNPs extremely difficult, even for small molecule ligands. Another important learning is that the ligand that can bind only nonspecifically to AuNP can be adsorbed faster than organothiols onto the AuNP surfaces. This in combination with the observations that the multicomponent ligand adsorption can be kinetically controlled raises concerns about the popular practices using Langmuir adsorption isotherm or its variants to model multicomponent ligand adsorption onto NPs. One must verify that the ligand binding system has reached equilibrium binding to NP before applying any thermodynamical models. The sequence-dependent multicomponent ligand binding method demonstrated in this work provides a convenient strategy for the experimental confirmation whether or not a ligand binding system can indeed reach thermodynamically equilibrial state. The insights from this work should be of broad importance in NP research and applications that involves multicomponent ligand interactions.

Notes: This work has been previously published: Siriwardana, K.; LaCour, A.; Zhang, D., Critical Sequence Dependence in Multicomponent Ligand Binding to Gold Nanoparticles. *J. Phys. Chem. C* **2016**, *120*, 6900-6905.

REFERENCES

(1) Ghosh, S. K.; Pal, A.; Nath, S.; Kundu, S.; Panigrahi, S.; Pal, T.: Dimerization of Eosin on Nanostructured Gold Surfaces: Size Regime Dependence of the Small Metallic Particles. *Chem. Phys. Lett.* **2005**, *412*, 5-11.

(2) Ghosh, S. K.; Pal, A.; Kundu, S.; Nath, S.; Pal, T.: Fluorescence Quenching of 1-Methylaminopyrene Near Gold Nanoparticles: Size Regime Dependence of the Small Metallic Particles. *Chem. Phys. Lett.* **2004**, *395*, 366-372.

(3) Kubo, R.: Electronic Properties of Metallic Fine Particles. I. *J. Phys. Soc. Jpn* **1962**, *17*, 975-986.

(4) Lipka, J.; Semmler-Behnke, M.; Sperling, R. A.; Wenk, A.; Takenaka, S.; Schleh, C.; Kissel, T.; Parak, W. J.; Kreyling, W. G.: Biodistribution of PEG-Modified Gold Nanoparticles Following Intratracheal Instillation and Intravenous Injection. *Biomaterials* **2010**, *31*, 6574-6581.

(5) Yuan, X.; Tay, Y.; Dou, X.; Luo, Z.; Leong, D. T.; Xie, J.: Glutathione-Protected Silver Nanoclusters as Cysteine-Selective Fluorometric and Colorimetric Probe. *Anal. Chem.* **2012**, *85*, 1913-1919.

(6) Zhang, N.; Qu, F.; Luo, H. Q.; Li, N. B.: Sensitive and Selective Detection of Biothiols Based on Target-induced Agglomeration of Silvernanoclusters. *Biosens. Bioelectron.* **2013**, *42*, 214-218.

(7) Aijaz, A.; Xu, Q.: Catalysis with Metal Nanoparticles Immobilized within the Pores of Metal–Organic Frameworks. *J. Phys. Chem. Lett.* **2014**, *5*, 1400-1411.

(8) Kuznetsov, A. S.; Tikhomirov, V. K.; Shestakov, M. V.; Moshchalkov, V. V.: Ag Nanocluster Functionalized Glasses for Efficient Photonic Conversion in Light Sources, Solar Cells and Flexible Screen Monitors. *Nanoscale* **2013**, *5*, 10065-10075.

(9) Dykman, L.; Khlebtsov, N.: Gold Nanoparticles in Biomedical Applications: Recent Advances and Perspectives. *Chem. Soc. Rev.* **2012**, *41*, 2256-2282.

(10) Saha, K.; Agasti, S. S.; Kim, C.; Li, X.; Rotello, V. M.: Gold Nanoparticles in Chemical and Biological Sensing. *Chem. Rev.* **2012**, *112*, 2739-2779.

(11) Turkevich, J.; Stevenson, P. C.; Hillier, J.: A Study of the Nucleation and Growth Processes in the synthesis of Colloidal Gold. *Discuss. Faraday Soc.* **1951**, *11*, 55-75.

(12) Frens, G.: Controlled Nucleation for the Regulation of the Particle Size in Monodisperse Gold Suspensions. *Nature* **1973**, *241*, 20-22.

(13) Brust, M.; Walker, M.; Bethell, D.; Schiffrin, D. J.; Whyman, R.: Synthesis of Thiol-Derivatised Gold Nanoparticles in a Two-Phase Liquid-Liquid System. *J. Chem. Soc., Chem. Comm.* **1994**, 801-802.

(14) Lee, P. C.; Meisel, D.: Adsorption and Surface-Enhanced Raman of Dyes on Silver and Gold Sols. *J.Phys.Chem.* **1982**, *86*, 3391-3395.

(15) Henglein, A.; Giersig, M.: Formation of Colloidal Silver Nanoparticles: Capping Action of Citrate. *J. Phys. Chem. B* **1999**, *103*, 9533-9539.

(16) Zhang, D.; Neumann, O.; Wang, H.; Yuwono, V. M.; Barhoumi, A.; Perham, M.; Hartgerink, J. D.; Wittung-Stafshede, P.; Halas, N. J.: Gold Nanoparticles Can Induce the Formation of Protein-based Aggregates at Physiological pH. *Nano Lett.* **2009**, *9*, 666-671.

(17) Pelaz, B.; del Pino, P.; Maffre, P.; Hartmann, R.; Gallego, M.; Rivera-Fernández, S.; de la Fuente, J. M.; Nienhaus, G. U.; Parak, W. J.: Surface Functionalization of Nanoparticles with Polyethylene Glycol: Effects on Protein Adsorption and Cellular Uptake. *ACS Nano* **2015**, *9*, 6996-7008.

(18) Mout, R.; Moyano, D. F.; Rana, S.; Rotello, V. M.: Surface Functionalization of Nanoparticles for Nanomedicine. *Chem. Soc. rev.* **2012**, *41*, 2539-2544.

(19) Love, J. C.; Estroff, L. A.; Kriebel, J. K.; Nuzzo, R. G.; Whitesides, G. M.: Self-Assembled Monolayers of Thiolates on Metals as a Form of Nanotechnology. *Chem. Rev.* **2005**, *105*, 1103-1170.

(20) Hostetler, M. J.; Templeton, A. C.; Murray, R. W.: Dynamics of Place-Exchange Reactions on Monolayer-Protected Gold Cluster Molecules. *Langmuir* **1999**, *15*, 3782-3789.

(21) Tsai, D.-H.; Davila-Morris, M.; DelRio, F. W.; Guha, S.; Zachariah, M. R.; Hackley, V. A.: Quantitative Determination of Competitive Molecular Adsorption on Gold Nanoparticles Using Attenuated Total Reflectance–Fourier Transform Infrared Spectroscopy. *Langmuir* **2011**, *27*, 9302-9313.

(22) AbdulHalim, L. G.; Kothalawala, N.; Sinatra, L.; Dass, A.; Bakr, O. M.: Neat and Complete: Thiolate-Ligand Exchange on a Silver Molecular Nanoparticle. *J. Am. Chem. Soc.* **2014**, *136*, 15865-15868.

(23) Sung, K.-M.; Mosley, D. W.; Peelle, B. R.; Zhang, S.; Jacobson, J. M.: Synthesis of Monofunctionalized Gold Nanoparticles by Fmoc Solid-Phase Reactions. *J. Am. Chem. Soc.* **2004**, *126*, 5064-5065.

(24) Kang, J. S.; Taton, T. A.: Oligothiol Graft-Copolymer Coatings Stabilize Gold Nanoparticles against Harsh Experimental Conditions. *Langmuir* **2012**, *28*, 16751-16760.

(25) Arnaout, C. L.; Gunsch, C. K.: Impacts of Silver Nanoparticle Coating on the Nitrification Potential of Nitrosomonas Europaea. *Environ. Sci. Technol.* **2012**, *46*, 5387-5395.

(26) Giljohann, D. A.; Seferos, D. S.; Daniel, W. L.; Massich, M. D.; Patel, P. C.; Mirkin, C. A.: Gold Nanoparticles for Biology and Medicine. *Angew. Chem. Int. Ed.* **2010**, *49*, 3280-3294.

(27) Karakoti, A. S.; Das, S.; Thevuthasan, S.; Seal, S.: PEGylated Inorganic Nanoparticles. *Angew. Chem. Int. Ed.* **2011**, *50*, 1980-1994.

(28) Euliss, L. E.; DuPont, J. A.; Gratton, S.; DeSimone, J.: Imparting Size, Shape, and Composition Control of Materials for Nanomedicine. *Chem. Soc. Rev.* **2006**, *35*, 1095-1104.

(29) Jokerst, J. V.; Lobovkina, T.; Zare, R. N.; Gambhir, S. S.: Nanoparticle PEGylation for Imaging and Therapy. *Nanomedicine* **2011**, *6*, 715-28.

(30) Caragheorgheopol, A.; Chechik, V.: Mechanistic Aspects of Ligand Exchange in Au Nanoparticles. *Phys. Chem. Chem. Phys.* **2008**, *10*, 5029-5041.

(31) Toh, H.; Batchelor-McAuley, C.; Tschulik, K.; Compton, R.: Chemical Interactions between Silver Nanoparticles and Thiols: A Comparison of Mercaptohexanol against Cysteine. *Sci. China Chem.* **2014**, *57*, 1199-1210.

(32) Volkert, A. A.; Subramaniam, V.; Ivanov, M. R.; Goodman, A. M.; Haes, A. J.: Salt-Mediated Self-Assembly of Thioctic Acid on Gold Nanoparticles. *ACS Nano* **2011**, *5*, 4570-4580.

(33) Martin, M. N.; Allen, A. J.; MacCuspie, R. I.; Hackley, V. A.: Dissolution, Agglomerate Morphology, and Stability Limits of Protein-Coated Silver Nanoparticles. *Langmuir* **2014**, *30*, 11442-11452.

(34) Xue, Y.; Li, X.; Li, H.; Zhang, W.: Quantifying Thiol–Gold Interactions Towards the Efficient Strength Control. *Nature Commun.* **2014**, *5*, 4348.

(35) Hakkinen, H.: The Gold-Sulfur Interface at the Nanoscale. *Nat. Chem.* **2012**, *4*, 443-455.

(36) Andrieux-Ledier, A.; Tremblay, B.; Courty, A.: Stability of Self-Ordered Thiol-Coated Silver Nanoparticles: Oxidative Environment Effects. *Langmuir* **2013**, *29*, 13140-13145.

(37) Laibinis, P. E.; Whitesides, G. M.; Allara, D. L.; Tao, Y. T.; Parikh, A. N.; Nuzzo, R. G.: Comparison of the Structures and Wetting Properties of Self-Assembled Monolayers of n-Alkanethiols on the Coinage Metal Surfaces, Copper, Silver, and Gold. *J. Am. Chem. Soc.* **1991**, *113*, 7152-7167.

(38) Liu, J.; Sonshine, D. A.; Shervani, S.; Hurt, R. H.: Controlled Release of Biologically Active Silver from Nanosilver Surfaces. *ACS Nano* **2010**, *4*, 6903-6913.

(39) Nidya, M.; Umadevi, M.; Rajkumar, B. J. M.: Structural, Morphological and Optical Studies of l-Cysteine Modified Silver Nanoparticles and Its Application as a Probe for the Selective Colorimetric Detection of Hg^{2+}. *Spectrochim. Acta A: Mole. and Biomole. Spec.* **2014**, *133*, 265-271.

(40) Ansar, S. M.; Perera, G. S.; Gomez, P.; Salomon, G.; Vasquez, E. S.; Chu, I. W.; Zou, S.; Pittman, C. U.; Walters, K. B.; Zhang, D.: Mechanistic Study of Continuous Reactive Aromatic Organothiol Adsorption onto Silver Nanoparticles. *J. Phys. Chem. C* **2013**, *117*, 27146-27154.

(41) Fenter, P.; Eisenberger, P.; Li, J.; Camillone, N.; Bernasek, S.; Scoles, G.; Ramanarayanan, T. A.; Liang, K. S.: Structure of Octadecyl Thiol Self-Assembled on the Silver(111) Surface: An Incommensurate Monolayer. *Langmuir* **1991**, *7*, 2013-2016.

(42) Mahmoudi, M.; Lynch, I.; Ejtehadi, M. R.; Monopoli, M. P.; Bombelli, F. B.; Laurent, S.: Protein−Nanoparticle Interactions: Opportunities and Challenges. *Chem. Rev.* **2011**, *111*, 5610-5637.

(43) Siriwardana, K.; Wang, A.; Vangala, K.; Fitzkee, N.; Zhang, D.: Probing the Effects of Cysteine Residues on Protein Adsorption onto Gold Nanoparticles Using Wild-Type and Mutated GB3 Proteins. *Langmuir* **2013**, *29*, 10990-10996.

(44) Casals, E.; Pfaller, T.; Duschl, A.; Oostingh, G. J.; Puntes, V.: Time Evolution of the Nanoparticle Protein Corona. *ACS Nano* **2010**, *4*, 3623-3632.

(45) Sen, T.; Mandal, S.; Haldar, S.; Chattopadhyay, K.; Patra, A.: Interaction of Gold Nanoparticle with Human Serum Albumin (HSA) Protein Using Surface Energy Transfer. *J. Phys. Chem. C* **2011**, *115*, 24037-24044.

(46) Brewer, S. H.; Glomm, W. R.; Johnson, M. C.; Knag, M. K.; Franzen, S.: Probing BSA Binding to Citrate-Coated Gold Nanoparticles and Surfaces. *Langmuir* **2005**, *21*, 9303-9307.

(47) Lynch, I.; Dawson, K. A.: Protein-Nanoparticle Interactions. *Nano Today* **2008**, *3*, 40-47.

(48) Mahmoudi, M.; Sant, S.; Wang, B.; Laurent, S.; Sen, T.: Superparamagnetic Iron Oxide Nanoparticles (SPIONs): Development, Surface Modification and Applications in Chemotherapy. *Adv. Drug Delivery Rev.* **2011**, *63*, 24-46.

(49) Mahmoudi, M.; Simchi, A.; Imani, M.; Shokrgozar, M. A.; Milani, A. S.; Häfeli, U. O.; Stroeve, P.: A New Approach for the In Vitro Identification of the Cytotoxicity of Superparamagnetic Iron Oxide Nanoparticles. *Colloids Surf. B: Biointerfaces* **2010**, *75*, 300-309.

(50) De, M.; Miranda, O. R.; Rana, S.; Rotello, V. M.: Size and Geometry Dependent Protein-Nanoparticle Self-Assembly. *Chem. Commun.* **2009**, 2157-2159.

(51) Hirsh, S. L.; McKenzie, D. R.; Nosworthy, N. J.; Denman, J. A.; Sezerman, O. U.; Bilek, M. M. M.: The Vroman effect: Competitive Protein Exchange with Dynamic Multilayer Protein Aggregates. *Colloids Surf., B* **2013**, *103*, 395-404.

(52) Cui, M.; Liu, R.; Deng, Z.; Ge, G.; Liu, Y.; Xie, L.: Quantitative Study of Protein Coronas on Gold Nanoparticles with Different Surface Modifications. *Nano Res.* **2014**, *7*, 345-352.

(53) Vangala, K.; Ameer, F.; Salomon, G.; Le, V.; Lewis, E.; Yu, L.; Liu, D.; Zhang, D.: Studying Protein and Gold Nanoparticle Interaction Using Organothiols as Molecular Probes. *J. Phys. Chem. C* **2012**, *116*, 3645-3652.

(54) Vangala, K.; Siriwardana, K.; Vasquez, E. S.; Xin, Y.; Pittman, C. U.; Walters, K. B.; Zhang, D.: Simultaneous and Sequential Protein and Organothiol Interactions with Gold Nanoparticles. *J. Phys. Chem. C* **2012**, *117*, 1366-1374.

(55) Marsh, D.; Bartucci, R.; Sportelli, L.: Lipid Membranes with Grafted Polymers: Physicochemical Aspects. *Biochim.Biophys. Acta (BBA) - Biomembranes* **2003**, *1615*, 33-59.

(56) Larson, T. A.; Joshi, P. P.; Sokolov, K.: Preventing Protein Adsorption and Macrophage Uptake of Gold Nanoparticles via a Hydrophobic Shield. *ACS Nano* **2012**, *6*, 9182-9190.

(57) Satulovsky, J.; Carignano, M. A.; Szleifer, I.: Kinetic and Thermodynamic Control of Protein Adsorption. *Proc. Nat.l Acad. Sci.* **2000**, *97*, 9037-9041.

(58) Alkilany, A.; Murphy, C.: Toxicity and Cellular Uptake of Gold Nanoparticles: What We Have Learned So Far? *J. Nanopart. Res.* **2010**, *12*, 2313-2333.

(59) Gao, J.; Huang, X.; Liu, H.; Zan, F.; Ren, J.: Colloidal Stability of Gold Nanoparticles Modified with Thiol Compounds: Bioconjugation and Application in Cancer Cell Imaging. *Langmuir* **2012**, *28*, 4464-4471.

(60) Levin, C. S.; Bishnoi, S. W.; Grady, N. K.; Halas, N. J.: Determining the Conformation of Thiolated Poly(ethylene glycol) on Au Nanoshells by Surface-Enhanced Raman Scattering Spectroscopic Assay. *Anal. Chem.* **2006**, *78*, 3277-3281.

(61) Eck, W.; Craig, G.; Sigdel, A.; Ritter, G.; Old, L. J.; Tang, L.; Brennan, M. F.; Allen, P. J.; Mason, M. D.: PEGylated Gold Nanoparticles Conjugated to Monoclonal F19 Antibodies as Targeted Labeling Agents for Human Pancreatic Carcinoma Tissue. *ACS Nano* **2008**, *2*, 2263-2272.

(62) Oh, E.; Delehanty, J. B.; Sapsford, K. E.; Susumu, K.; Goswami, R.; Blanco-Canosa, J. B.; Dawson, P. E.; Granek, J.; Shoff, M.; Zhang, Q.; Goering, P. L.; Huston, A.; Medintz, I. L.: Cellular Uptake and Fate of PEGylated Gold Nanoparticles Is Dependent on Both Cell-Penetration Peptides and Particle Size. *ACS Nano* **2011**, *5*, 6434-6448.

(63) Larson-Smith, K.; Pozzo, D. C.: Competitive Adsorption of Thiolated Poly(ethylene glycol) and Alkane-Thiols on Gold Nanoparticles and Its Effect on Cluster Formation. *Langmuir* **2012**, *28*, 13157-13165.

(64) Larson-Smith, K.; Pozzo, D. C.: Scalable synthesis of self-assembling nanoparticle clusters based on controlled steric interactions. *Soft. Matter.* **2011**, *7*, 5339-5347.

(65) Tsai, D.-H.; DelRio, F. W.; MacCuspie, R. I.; Cho, T. J.; Zachariah, M. R.; Hackley, V. A.: Competitive Adsorption of Thiolated Polyethylene Glycol and Mercaptopropionic Acid on Gold Nanoparticles Measured by Physical Characterization Methods. *Langmuir* **2010**, *26*, 10325-10333.

(66) Rahme, K.; Chen, L.; Hobbs, R. G.; Morris, M. A.; O'Driscoll, C.; Holmes, J. D.: PEGylated Gold Nanoparticles: Polymer Quantification as a Function of PEG Lengths and Nanoparticle Dimensions. *RSC Adv.* **2013**, *3*, 6085-6094.

(67) Delfino, I.; Cannistraro, S.: Optical Investigation of the Electron Transfer Protein Azurin–Gold Nanoparticle System. *Biophys. Chem.* **2009**, *139*, 1-7.

(68) You, C.-C.; Miranda, O. R.; Gider, B.; Ghosh, P. S.; Kim, I.-B.; Erdogan, B.; Krovi, S. A.; Bunz, U. H. F.; Rotello, V. M.: Detection and Identification of Proteins using Nanoparticle-Fluorescent Polymer /`Chemical Nose/' Sensors. *Nature Nanotech.* **2007**, *2*, 318-323.

(69) Pramanik, S.; Banerjee, P.; Sarkar, A.; Bhattacharya, S. C.: Size-Dependent Interaction of Gold Nanoparticles with Transport Protein: A Spectroscopic Study. *J. Lumines.* **2008**, *128*, 1969-1974.

(70) Pagliai, M.; Caporali, S.; Muniz-Miranda, M.; Pratesi, G.; Schettino, V.: SERS, XPS, and DFT Study of Adenine Adsorption on Silver and Gold Surfaces. *J. Phys. Chem. Lett.* **2012**, *3*, 242-245.

(71) Cho, S. H.; Han, H. S.; Jang, D.-J.; Kim, K.; Kim, M. S.: Raman Spectroscopic Study of 1,4-Benzenedithiol Adsorbed on Silver. *J.Phys.Chem.* **1995**, *99*, 10594-10599.

(72) Jiang, X.; Jiang, J.; Jin, Y.; Wang, E.; Dong, S.: Effect of Colloidal Gold Size on the Conformational Changes of Adsorbed Cytochrome c: Probing by Circular Dichroism, UV−Visible, and Infrared Spectroscopy. *Biomacromol.* **2005**, *6*, 46-53.

(73) Sau, T. K.; Murphy, C. J.: Room Temperature, High-Yield Synthesis of Multiple Shapes of Gold Nanoparticles in Aqueous Solution. *J. Am. Chem. Soc.* **2004**, *126*, 8648-8649.

(74) Buhr, E.; Senftleben, N.; Klein, T.; Bergmann, D.; Gnieser, D.; Frase, C. G.; Bosse, H.: Characterization of Nanoparticles by Scanning Electron Microscopy in Transmission Mode. *Measurement Sci. and Technol.* **2009**, *20*, 084025.

(75) Martínez-Castañón, G. A.; Niño-Martínez, N.; Martínez-Gutierrez, F.; Martínez-Mendoza, J. R.; Ruiz, F.: Synthesis and Antibacterial Activity of Silver Nanoparticles with Different Sizes. *J. Nanopart. Res.* **2008**, *10*, 1343-1348.

(76) Kelly, K. L.; Coronado, E.; Zhao, L. L.; Schatz, G. C.: The Optical Properties of Metal Nanoparticles: The Influence of Size, Shape, and Dielectric Environment. *J. Phys. Chem. B* **2003**, *107*, 668-677.

(77) Petryayeva, E.; Krull, U. J.: Localized Surface Plasmon Resonance: Nanostructures, Bioassays and Biosensing—A Review. *Anal. Chim. Acta* **2011**, *706*, 8-24.

(78) Hutter, E.; Fendler, J. H.: Exploitation of Localized Surface Plasmon Resonance. *Adv. Mater.* **2004**, *16*, 1685-1706.

(79) Willets, K. A.; Van Duyne, R. P.: Localized Surface Plasmon Resonance Spectroscopy and Sensing. *Annu. Rev. Phys. Chem.* **2007**, *58*, 267-297.

(80) Ghosh, S. K.; Pal, T.: Interparticle Coupling Effect on the Surface Plasmon Resonance of Gold Nanoparticles: From Theory to Applications. *Chem. Rev.* **2007**, *107*, 4797-4862.

(81) Horvath, H.: Gustav Mie and the Scattering and Absorption of Light by Particles: Historic Developments and Basics. *J. Quant. Spec. Radiative Trans.* **2009**, *110*, 787-799.

(82) Harris, J. M.: Introduction to Biotechnical and Biomedical Applications of Poly(Ethylene Glycol). In *Poly(Ethylene Glycol) Chemistry*; Harris, J. M., Ed.; Springer US, 1992; pp 1-14.

(83) Walkey, C. D.; Olsen, J. B.; Guo, H.; Emili, A.; Chan, W. C. W.: Nanoparticle Size and Surface Chemistry Determine Serum Protein Adsorption and Macrophage Uptake. *J. Am. Chem. Soc.* **2011**, *134*, 2139-2147.

(84) Ansar, S. M.; Haputhanthri, R.; Edmonds, B.; Liu, D.; Yu, L.; Sygula, A.; Zhang, D.: Determination of the Binding Affinity, Packing, and Conformation of Thiolate and Thione Ligands on Gold Nanoparticles. *J. Phys. Chem. C* **2010**, *115*, 653-660.

(85) Ansar, S. M.; Perera, G. S.; Ameer, F. S.; Zou, S.; Pittman, C. U.; Zhang, D.: Desulfurization of Mercaptobenzimidazole and Thioguanine on Gold Nanoparticles Using Sodium Borohydride in Water at Room Temperature. *J. Phys. Chem. C* **2013**, *117*, 13722-13729.

(86) Zin, M. T.; Yip, H.-L.; Wong, N.-Y.; Ma, H.; Jen, A. K. Y.: Arrays of Covalently Bonded Single Gold Nanoparticles on Thiolated Molecular Assemblies. *Langmuir* **2006**, *22*, 6346-6351.

(87) Ansar, S. M.; Perera, G. S.; Jiang, D.; Holler, R. A.; Zhang, D.: Organothiols Self-Assembled onto Gold: Evidence for Deprotonation of the Sulfur-Bound Hydrogen and Charge Transfer from Thiolate. *J. Phys. Chem. C* **2013**, *117*, 8793-8798.

(88) Reyes, E. N.; Madueno, R.; Blazquez, M.; Pineda, T.: Facile Exchange of Ligands on the 6-Mercaptopurine-Monolayer Protected Gold Clusters Surface. *J. Phys. Chem. C* **2010**, *114*, 15955-15962.

(89) Franzen, S.; Folmer, J. C. W.; Glomm, W. R.; O'Neal, R.: Optical Properties of Dye Molecules Adsorbed on Single Gold and Silver Nanoparticles. *J. Phys. Chem. A* **2002**, *106*, 6533-6540.

(90) Lombardi, J. R.; Birke, R. L.: A Unified Approach to Surface-Enhanced Raman Spectroscopy. *J. Phys. Chem. C* **2008**, *112*, 5605-5617.

(91) Valley, N.; Greeneltch, N.; Van Duyne, R. P.; Schatz, G. C.: A Look at the Origin and Magnitude of the Chemical Contribution to the Enhancement Mechanism of Surface-Enhanced Raman Spectroscopy (SERS): Theory and Experiment. *J. Phys. Chem. Lett.* **2013**, *4*, 2599-2604.

(92) Freeman, R. G.; Hommer, M. B.; Grabar, K. C.; Jackson, M. A.; Natan, M. J.: Ag-Clad Au Nanoparticles: Novel Aggregation, Optical, and Surface-Enhanced Raman Scattering Properties. *J. Phys. Chem.* **1996**, *100*, 718-724.

(93) Jin, R.; Wu, G.; Li, Z.; Mirkin, C. A.; Schatz, G. C.: What Controls the Melting Properties of DNA-Linked Gold Nanoparticle Assemblies? *J. Am. Chem. Soc.* **2003**, *125*, 1643-1654.

(94) Jung, L. S.; Campbell, C. T.; Chinowsky, T. M.; Mar, M. N.; Yee, S. S.: Quantitative Interpretation of the Response of Surface Plasmon Resonance Sensors to Adsorbed Films. *Langmuir* **1998**, *14*, 5636-5648.

(95) Bantz, K. C.; Nelson, H. D.; Haynes, C. L.: Plasmon-Enabled Study of Self-Assembled Alkanethiol Ordering on Roughened Ag Substrates. *J. Phys. Chem. C* **2012**, *116*, 3585-3593.

(96) Malinsky, M. D.; Kelly, K. L.; Schatz, G. C.; Van Duyne, R. P.: Chain Length Dependence and Sensing Capabilities of the Localized Surface Plasmon Resonance of Silver Nanoparticles Chemically Modified with Alkanethiol Self-Assembled Monolayers. *J. Am. Chem. Soc.* **2001**, *123*, 1471-1482.

(97) Manson, J.; Kumar, D.; Meenan, B.; Dixon, D.: Polyethylene Glycol Functionalized Gold Nanoparticles: the Influence of Capping Density on Stability in Various Media. *Gold Bull* **2011**, *44*, 99-105.

(98) De Roe, C.; Courtoy, P. J.; Baudhuin, P.: A Model of Protein-Colloidal Gold Interactions. *J. Histochem. Cytochem.* **1987**, *35*, 1191-8.

(99) Tsai, D.-H.; DelRio, F. W.; Keene, A. M.; Tyner, K. M.; MacCuspie, R. I.; Cho, T. J.; Zachariah, M. R.; Hackley, V. A.: Adsorption and Conformation of Serum Albumin Protein on Gold Nanoparticles Investigated Using Dimensional Measurements and in Situ Spectroscopic Methods. *Langmuir* **2011**, *27*, 2464-2477.

(100) Tao, N. J.; DeRose, J. A.; Lindsay, S. M.: Self-assembly of Molecular Superstructures Studied by In Situ Scanning Tunneling Microscopy: DNA Bases on Gold (111). *J. Phys. Chem.* **1993**, *97*, 910-919.

(101) Zou, S.: Electromagnetic Wave Propagation in a Multilayer Silver Particle. *Chem. Phys. Lett.* **2008**, *454*, 289-293.

(102) Zhang, D.; Ansar, S. M.: Ratiometric Surface Enhanced Raman Quantification of Ligand Adsorption onto a Gold Nanoparticle. *Anal. Chem.* **2010**, *82*, 5910-5914.

(103) Ahamed, M.; AlSalhi, M. S.; Siddiqui, M. K. J.: Silver Nanoparticle Applications and Human Health. *Clin. Chim. Acta* **2010**, *411*, 1841-1848.

(104) Choi, O.; Deng, K. K.; Kim, N.-J.; Ross Jr, L.; Surampalli, R. Y.; Hu, Z.: The Inhibitory Effects of Silver Nanoparticles, Silver Ions, and Silver Chloride Colloids on Microbial Growth. *Water Res.* **2008**, *42*, 3066-3074.

(105) Jana, N. R.; Sau, T. K.; Pal, T.: Growing Small Silver Particle as Redox Catalyst. *J. Phys.Chem. B* **1998**, *103*, 115-121.

(106) Li, X.; Lenhart, J. J.; Walker, H. W.: Dissolution-Accompanied Aggregation Kinetics of Silver Nanoparticles. *Langmuir* **2010**, *26*, 16690-16698.

(107) Yin, Y.; Li, Z.-Y.; Zhong, Z.; Gates, B.; Xia, Y.; Venkateswaran, S.: Synthesis and Characterization of Stable Aqueous Dispersions of Silver Nanoparticles Through the Tollens Process. *J. Mater. Chem.* **2002**, *12*, 522-527.

(108) Chen, M.; Wang, L.-Y.; Han, J.-T.; Zhang, J.-Y.; Li, Z.-Y.; Qian, D.-J.: Preparation and Study of Polyacryamide-Stabilized Silver Nanoparticles through a One-Pot Process. *J. Phys. Chem. B* **2006**, *110*, 11224-11231.

(109) Ansar, S. M.; Gadogbe, M.; Siriwardana, K.; Howe, J. Y.; Dogel, S.; Hosseinkhannazer, H.; Collier, W. E.; Rodriguez, J.; Zou, S.; Zhang, D.: Dispersion Stability, Ligand Structure and Conformation, and SERS Activities of 1-Alkanethiol Functionalized Gold and Silver Nanoparticles. *J. Phys. Chem. C* **2014**, *118*, 24925-24934.

(110) Derrick, J. P.; Wigley, D. B.: The Third IgG-Binding Domain from Streptococcal Protein G: An Analysis by X-ray Crystallography of the Structure Alone and in a Complex with Fab. *J. Mol. Biol.* **1994**, *243*, 906-918.

(111) Ulmer, T. S.; Ramirez, B. E.; Delaglio, F.; Bax, A.: Evaluation of Backbone Proton Positions and Dynamics in a Small Protein by Liquid Crystal NMR Spectroscopy. *J. Am. Chem. Soc.* **2003**, *125*, 9179-9191.

(112) Kang, Y. N.; Kim, H.; Shin, W. S.; Woo, G.; Moon, T. W.: Effect of Disulfide Bond Reduction on Bovine Serum Albumin-Stabilized Emulsion Gel Formed by Microbial Transglutaminase. *J. Food Sci.* **2003**, *68*, 2215-2220.

(113) MacCuspie, R.: Colloidal Stability of Silver Nanoparticles in Biologically Relevant Conditions. *J. Nanopart. Res.* **2011**, *13*, 2893-2908.

(114) Tai, J.-T.; Lai, C.-S.; Ho, H.-C.; Yeh, Y.-S.; Wang, H.-F.; Ho, R.-M.; Tsai, D.-H.: Protein–Silver Nanoparticle Interactions to Colloidal Stability in Acidic Environments. *Langmuir* **2014**, *30*, 12755-12764.

(115) Ostermeyer, A.-K.; Kostigen Mumuper, C.; Semprini, L.; Radniecki, T.: Influence of Bovine Serum Albumin and Alginate on Silver Nanoparticle Dissolution and Toxicity to Nitrosomonas europaea. *Environ. Sci. Technol.* **2013**, *47*, 14403-14410.

(116) Gondikas, A. P.; Morris, A.; Reinsch, B. C.; Marinakos, S. M.; Lowry, G. V.; Hsu-Kim, H.: Cysteine-Induced Modifications of Zero-valent Silver Nanomaterials: Implications for Particle Surface Chemistry, Aggregation, Dissolution, and Silver Speciation. *Environ. Sci. Technol.* **2012**, *46*, 7037-7045.

(117) López-Tobar, E.; Hernández, B.; Ghomi, M.; Sanchez-Cortes, S.: Stability of the Disulfide Bond in Cystine Adsorbed on Silver and Gold Nanoparticles As Evidenced by SERS Data. *J. Phys. Chem. C* **2012**, *117*, 1531-1537.

(118) Pokhrel, L. R.; Dubey, B.; Scheuerman, P. R.: Impacts of Select Organic Ligands on the Colloidal Stability, Dissolution Dynamics, and Toxicity of Silver Nanoparticles. *Environ. Sci.Technol.* **2013**, *47*, 12877-12885.

(119) Navarro, E.; Piccapietra, F.; Wagner, B.; Marconi, F.; Kaegi, R.; Odzak, N.; Sigg, L.; Behra, R.: Toxicity of Silver Nanoparticles to Chlamydomonas reinhardtii. *Environ.Sci.Technol.* **2008**, *42*, 8959-8964.

(120) Eigenheer, R.; Castellanos, E. R.; Nakamoto, M. Y.; Gerner, K. T.; Lampe, A. M.; Wheeler, K. E.: Silver Nanoparticle Protein Corona Composition Compared Across Engineered Particle Properties and Environmentally Relevant Reaction Conditions. *Environ. Sci.: Nano* **2014**, *1*, 238-247.

(121) Kim, J. A.; Salvati, A.; Aberg, C.; Dawson, K. A.: Suppression of Nanoparticle Cytotoxicity Approaching In vivo Serum Concentrations: Limitations of In Vitro Testing for Nanosafety. *Nanoscale* **2014**, *6*, 14180-14184.

(122) Lee, H.; Kim, M. S.; Suh, S. W.: Raman Spectroscopy of Sulphur-Containing Amino Acids and Their Derivatives Adsorbed on Silver. *J.Raman Spectrosc.* **1991**, *22*, 91-96.

(123) Wang, A.; Vangala, K.; Vo, T.; Zhang, D.; Fitzkee, N. C.: A Three-Step Model for Protein–Gold Nanoparticle Adsorption. *J. Phys. Chem. C* **2014**, *118*, 8134-8142.

(124) Maiolo, D.; Bergese, P.; Mahon, E.; Dawson, K. A.; Monopoli, M. P.: Surfactant Titration of Nanoparticle–Protein Corona. *Anal. Chem.* **2014**.

(125) Monopoli, M. P.; Åberg, C.; Salvati, A.; Dawson, K. A.: Biomolecular Coronas Provide the Biological Identity of Nanosized Materials. *Nature Nanotech.* **2012**, *7*, 779-786.

(126) Requejo, R.; Hurd, T. R.; Costa, N. J.; Murphy, M. P.: Cysteine Residues Exposed on Protein Surfaces Are The Dominant Intramitochondrial Thiol and May Protect Against Oxidative Damage. *FEBS J.* **2010**, *277*, 1465-1480.

(127) Houk, R. J. T.; Jacobs, B. W.; Gabaly, F. E.; Chang, N. N.; Talin, A. A.; Graham, D. D.; House, S. D.; Robertson, I. M.; Allendorf, M. D.: Silver Cluster Formation, Dynamics, and Chemistry in Metal−Organic Frameworks. *Nano Lett.* **2009**, *9*, 3413-3418.

(128) Yu, S.-j.; Yin, Y.-g.; Liu, J.-f.: Silver Nanoparticles in the Environment. *Environ. Sci.: Processes & Impacts* **2013**, *15*, 78-92.

(129) Cui, Y.; Wang, Y.; Liu, R.; Sun, Z.; Wei, Y.; Zhao, Y.; Gao, X.: Serial Silver Clusters Biomineralized by One Peptide. *ACS Nano* **2011**, *5*, 8684-8689.

(130) Chakraborty, I.; Udayabhaskararao, T.; Deepesh, G. K.; Pradeep, T.: Sunlight Mediated Synthesis and Antibacterial Properties of Monolayer Protected Silver Clusters. *J. Mater. Chem. B* **2013**, *1*, 4059-4064.

(131) Graham, D.; Thompson, D. G.; Smith, W. E.; Faulds, K.: Control of Enhanced Raman Scattering using a DNA-based Assembly Process of Dye-Coded Nanoparticles. *Nature Nanotech.* **2008**, *3*, 548-551.

(132) Faghihi, F.; Hazendonk, P.; Montina, T.: Investigation into the Mechanism and Microstructure of Reaction Intermediates in the Two-Phase Synthesis of Alkanethiol-Capped Silver Nanoparticles. *Langmuir* **2015**, *31*, 3473-3481.

(133) Baksi, A.; Bootharaju, M. S.; Chen, X.; Häkkinen, H.; Pradeep, T.: $Ag_{11}(SG)_7$: A New Cluster Identified by Mass Spectrometry and Optical Spectroscopy. *J. Phys. Chem. C* **2014**, *118*, 21722-21729.

(134) Adhikari, B.; Banerjee, A.: Facile Synthesis of Water-Soluble Fluorescent Silver Nanoclusters and HgII Sensing. *Chem. Mater.* **2010**, *22*, 4364-4371.

(135) Cathcart, N.; Kitaev, V.: Silver Nanoclusters: Single-Stage Scaleable Synthesis of Monodisperse Species and Their Chirooptical Properties. *J.Phys. Chem.C* **2010**, *114*, 16010-16017.

(136) McLellan, J. M.; Li, Z.-Y.; Siekkinen, A. R.; Xia, Y.: The SERS Activity of a Supported Ag Nanocube Strongly Depends on Its Orientation Relative to Laser Polarization. *Nano Lett.* **2007**, *7*, 1013-1017.

(137) Adams, N. H.; Kramer, J.: Potentiometric Determination of Silver Thiolate Formation Constants Using a Ag_2S Electrode. *Aquatic Geochem.* **1999**, *5*, 1-11.

(138) Tsujimura, S.; Tatsumi, H.; Ogawa, J.; Shimizu, S.; Kano, K.; Ikeda, T.: Bioelectrocatalytic Reduction of Dioxygen to Water at Neutral pH using Bilirubin Oxidase as an Enzyme and 2,2′-azinobis (3-ethylbenzothiazolin-6-sulfonate) as an Electron Transfer Mediator. *J. Electroanal. Chem.* **2001**, *496*, 69-75.

(139) Jocelyn, P. C.: The Standard Redox Potential of Cysteine-Cystine from the Thiol-Disulphide Exchange Reaction with Glutathione and Lipoic Acid. *Eur. J. Biochem.* **1967**, *2*, 327-331.

(140) Rost, J.; Rapoport, S.: Reduction-potential of Glutathione. *Nature* **1964**, *201*, 185-185.

(141) Siriwardana, K.; Wang, A.; Gadogbe, M.; Collier, W. E.; Fitzkee, N. C.; Zhang, D.: Studying the Effects of Cysteine Residues on Protein Interactions with Silver Nanoparticles. *J. Phys. Chem. C* **2015**, *119*, 2910-2916.

(142) Shen, L.-M.; Chen, Q.; Sun, Z.-Y.; Chen, X.-W.; Wang, J.-H.: Assay of Biothiols by Regulating the Growth of Silver Nanoparticles with C-Dots as Reducing Agent. *Anal. Chem.* **2014**, *86*, 5002-5008.

(143) Krylova, V.; Duktien, N.: Synthesis and Characterization of Ag_2S Layers Formed on Polypropylene. *J. Chem.* **2013**, *2013*, 11.

(144) Åslund, F.; Berndt, K. D.; Holmgren, A.: Redox Potentials of Glutaredoxins and Other Thiol-Disulfide Oxidoreductases of the Thioredoxin Superfamily Determined by Direct Protein-Protein Redox Equilibria. *J. Biol. Chem.* **1997**, *272*, 30780-30786.

(145) Lukesh, J. C.; Palte, M. J.; Raines, R. T.: A Potent, Versatile Disulfide-Reducing Agent from Aspartic Acid. *J. Am.Chem.Soc.* **2012**, *134*, 4057-4059.

(146) Liu, J.; Yu, M.; Ning, X.; Zhou, C.; Yang, S.; Zheng, J.: PEGylation and Zwitterionization: Pros and Cons in the Renal Clearance and Tumor Targeting of Near-IR-Emitting Gold Nanoparticles. *Angew. Chem. Int. Ed.* **2013**, *52*, 12572-12576.

(147) Lacerda, S. H. D. P.; Park, J. J.; Meuse, C.; Pristinski, D.; Becker, M. L.; Karim, A.; Douglas, J. F.: Interaction of Gold Nanoparticles with Common Human Blood Proteins. *ACS Nano* **2010**, *4*, 365-379.

(148) Perera, G. S.; Nettles, C. B.; Zhou, Y.; Zou, S.; Hollis, T. K.; Zhang, D.: Direct Observation of Ion Pairing at the Liquid/Solid Interfaces by Surface Enhanced Raman Spectroscopy. *Langmuir* **2015**, *31*, 8998-9005.

(149) Siriwardana, K.; Gadogbe, M.; Ansar, S. M.; Vasquez, E. S.; Collier, W. E.; Zou, S.; Walters, K. B.; Zhang, D.: Ligand Adsorption and Exchange on Pegylated Gold Nanoparticles. *J. Phys. Chem. C* **2014**, *118*, 11111-11119.

(150) Ghosh, P.; Yang, X.; Arvizo, R.; Zhu, Z.-J.; Agasti, S. S.; Mo, Z.; Rotello, V. M.: Intracellular Delivery of a Membrane-Impermeable Enzyme in Active Form Using Functionalized Gold Nanoparticles. *J. Am. Chem. Soc.* **2010**, *132*, 2642-2645.

(151) Lee, K. Y. J.; Wang, Y.; Nie, S.: In Vitro Study of a pH-Sensitive Multifunctional Doxorubicin-Gold Nanoparticle System: Therapeutic Effect and Surface Enhanced Raman scattering. *RSC Adv.* **2015**, *5*, 65651-65659.

(152) Lee, S.; Kim, S.; Choo, J.; Shin, S. Y.; Lee, Y. H.; Choi, H. Y.; Ha, S.; Kang, K.; Oh, C. H.: Biological Imaging of HEK293 Cells Expressing PLCγ1 Using Surface-Enhanced Raman Microscopy. *Anal. Chem.* **2007**, *79*, 916-922.

(153) Rodriguez, I.; Ramiro-Manzano, F.; Atienzar, P.; Martinez, J. M.; Meseguer, F.; Garcia, H.; Corma, A.: Solar Energy Harvesting in Photoelectrochemical Solar Cells. *J. Mater. Chem.* **2007**, *17*, 3205-3209.

(154) Choy, K. K. H.; Porter, J. F.; McKay, G.: Langmuir Isotherm Models Applied to the Multicomponent Sorption of Acid Dyes from Effluent onto Activated Carbon. *J. Chem. Eng. Data* **2000**, *45*, 575-584.

(155) Yao, L.; Grishaev, A.; Cornilescu, G.; Bax, A.: The Impact of Hydrogen Bonding on Amide 1H Chemical Shift Anisotropy Studied by Cross-Correlated Relaxation and Liquid Crystal NMR Spectroscopy. *J.Am.Chem. Soc.* **2010**, *132*, 10866-10875.

(156) Doneux, T.; Buess-Herman, C.; Lipkowski, J.: Electrochemical and FTIR Characterization of the Self-assembled Monolayer of 2-Mercaptobenzimidazole on Au(1 1 1). *J. Electroanal. Chem.* **2004**, *564*, 65-75.

(157) Huetz, P.; Ball, V.; Voegel, J. C.; Schaaf, P.: Exchange Kinetics for a Heterogeneous Protein System on a Solid Surface. *Langmuir* **1995**, *11*, 3145-3152.

(158) Kotaro, K.; Masahiko, H.; Hiroyuki, S.; Wolfgang, K.: Exchange Kinetics of Alkanethiol Self-Assembled Monolayers Probed by Attenuated Total Reflection with Enhancement of Surface Plasmon Resonance. *Jpn. J. Appl. Phys.* **1997**, *36*, L1116.

(159) Guo, R.; Song, Y.; Wang, G.; Murray, R. W.: Does Core Size Matter in the Kinetics of Ligand Exchanges of Monolayer-Protected Au Clusters? *J. Am. Chem. Soc.* **2005**, *127*, 2752-2757.

(160) Ionita, P.; Caragheorgheopol, A.; Gilbert, B. C.; Chechik, V.: EPR Study of a Place-Exchange Reaction on Au Nanoparticles: Two Branches of a Disulfide Molecule Do Not Adsorb Adjacent to Each Other. *J. Am. Chem. Soc.* **2002**, *124*, 9048-9049.

(161) Bain, C. D.; Whitesides, G. M.: Formation of Monolayers by the Coadsorption of Thiols on Gold: Variation in the Length of the Alkyl Chain. *J. Am. Chem. Soc.* **1989**, *111*, 7164-7175.

(162) Heinecke, C. L.; Ni, T. W.; Malola, S.; Mäkinen, V.; Wong, O. A.; Häkkinen, H.; Ackerson, C. J.: Structural and Theoretical Basis for Ligand Exchange on Thiolate Monolayer Protected Gold Nanoclusters. *J. Am. Chem. Soc.* **2012**, *134*, 13316-13322.

(163) Templeton, A. C.; Wuelfing, W. P.; Murray, R. W.: Monolayer-Protected Cluster Molecules. *Accounts Chem. Res.* **2000**, *33*, 27-36.